UNIVERSITY OF OKLAHOMA

GRADUATE COLLEGE

BUILDING CLUSTER CONTROL TO ENABLE GRID RELIABILITY AND EFFICIENCY SUPPORT

A DISSERTATION

SUBMITTED TO THE GRADUATE FACULTY

in partial fulfillment of the requirements for the

Degree of

DOCTOR OF PHILOSOPHY

By

ZHIMIN JIANG
Norman, Oklahoma
2022

BUILDING CLUSTER CONTROL TO ENABLE GRID RELIABILITY AND EFFICIENCY SUPPORT

A DISSERTATION APPROVED FOR THE
SCHOOL OF AEROSPACE AND MECHANICAL ENGINEERING

BY THE COMMITTEE CONSISTING OF

Dr. Jie Cai, Chair

Dr. Choon Yik Tang

Dr. Li Song

Dr. Paul Moses

Dr. Wei Sun

Dedicated

to my beloved parents

ACKNOWLEDGMENTS

I would like to give my gratitude and admiration to my advisor, Dr. Cai, who logged a considerable amount of time coaching me throughout this process. His patient guidance and encouragement led me through this journey and his diligence and perseverance also inspires everyone working in his group. The experience in his lab will be a treasure that will benefit me for the rest of my life. I would also like to thank Dr. Tang for his expert knowledge, valuable feedback and support during my extremely difficult time in my academic career, as well as for recommending me to Dr. Cai.

I would like to also thank all my committee members. Thank you, Dr. Song, Dr. Moses, and Dr. Sun for taking your time and being a part of my committee.

I am also grateful for my dearest labmates, colleagues, it is their companionship that makes my PhD life an enjoyable experience and a lasting memory.

Special thanks to Peng Wu, for all his love and support.

TABLE OF CONTENTS

LIST OF TABLES

LIST OF FIGURES

LIST OF ACRONYMS

CAES Compressed air energy storage

DLC Direct load control

GNEP generalized Nash equilibrium problem

HIL hardware-in-the-loop

HVAC heating, ventilation and air-conditioning

MPP maximum power point

NE Nash equilibrium

NEP Nash equilibrium problem

NI Nikaido-Isoda function

PAR peak to average ratio

PI proportional-integral

PV solar photovoltaic

SVR step voltage regulator

TOU time-of-use

VCG Vickrey-Clarke-Groves

VFD variable frequency drive

VI Variational Inequality

ZAT zone air temperature

ABSTRACT

Power system operators are actively seeking solutions to increase electric grid power flexibility and inertia, to accommodate deeper renewable integration. Buildings account for 75% of the total electricity use in the US and have great potential for grid reliability support at various time and spatial scales. Due to the limited bidding power of individual buildings, grid services are often provided by a fleet of small buildings managed by tailored coordination strategies. This dissertation presents two families of control methods for building cluster energy management based on the control time frequency and inter-building coordination mode: (1) dictatorial load modulating control strategies formulated under a specific context of distribution voltage regulation, and (2) market-based load shifting control achieved through a game-theoretic control framework. Load modulation can enable distribution voltage support by controling flexible loads in the building clusters to let their power use follow volatile solar photovoltaic (PV) output, as a means to mitigate fluctuations in the net demand and maintain a stable voltage. The game-theoretic control strategies allow coordinative load shifting in which individual entities determine their control actions in their own interests while coordination is achieved indirectly through a market mechanism, with a goal of flattening the total load curve of the building cluster.

For load modulation, two dictatorial control strategies were developed for heating, ventilation and air-conditioning (HVAC) systems in support of voltage regulation of distribution networks with high PV penetration. For voltage support, the flexible HVAC loads are proactively controlled by the aggregator to smooth out fluctuations in the net demand and PV generation. The first control strategy was developed for variable-capacity HVAC systems whose compressor speeds/stages are directly controlled by a central controller to achieve load modulation in response to real-time voltage reading. The control effectiveness was verified by hardware-in-the-loop (HIL) tests, combining a 33-bus distribution feeder model and an actual 3-ton heat pump. Laboratory tests showed that the strategy was effective in

reducing variations of net demand with negligible impact on indoor comfort, resulting in 55% reductions of voltage fluctuations and complete or partial elimination of voltage regulator tap operations. The second control method for voltage support is to coordinate the cycling of HVAC systems and water heaters in different buildings to provide proactive voltage support against volatile solar generation. The control performance was evaluated with a co-simulation platform for PV-rich residential community with cycling HVAC and water heating equipment. The platform allows co-simulation of 100 high-fidelity EnergyPlus models for residential dwellings, a solar PV model, and a distribution network power flow model, to capture interactions between the loads, PV generation and distribution voltage. Simulation tests have shown that the voltage regulation strategies using flexible building loads could help reduce operations of step voltage regulators by up to 73%.

The second part of this dissertation describes a new game theoretic control framework to enable market-based load shifting of building clusters. Analyses were carried out for two operational scenarios, namely explicit peak demand reduction control and optimal flexible load dispatch. The peak demand reduction game considers a peak demand charge which is proportional to the monthly peak demand of the whole aggregation. A Shapley value-based cost allocation mechanism, along with a log-sum-exponential approximate of the non-differentiable max operator, was designed to solve the aggregate demand reduction problem. The existence and uniqueness of Nash equilibrium (NE) solution were established with the aid of Variational Inequality (VI) theory. A centralized algorithm and a distributed algorithm were proposed to find the NE, and the convergence was rigorously proved under certain conditions. Numerical tests with a commercial community showed that the control performance attained was close to social optimum with less than 2% performance degradation. For the flexible load dispatch game, a marginal generation cost curve is assumed which is dependent on the collective demand of the whole aggregation. This study considered a power model and an exponential model for the marginal cost curve and proved the existence and uniqueness of NE for these two cost models. A simulation case study was considered using a linear

marginal cost model to demonstrate the efficacy of the proposed game-theoretic control for flexible load dispatching in building clusters. A distributed best response algorithm was developed to find the NE. The simulation tests showed that the game-theoretic control could reduce the overall operating cost by 5.8% and reduce peak load by 28% compared to a baseline operation strategy. The achieved performance was very close to the social optimum, with a Price of Anarchy of 1.007.

CHAPTER 1

INTRODUCTION

Proliferation of renewable energy resources and growing electricity demand are placing increasing stress on the power grid. Flexible electrical demands can be utilized to alleviate the stress, enabling a more robust and reliable electric power system while reducing consumer costs. Buildings, as the nation's largest power consumer, account for 75% of U.S. electricity consumption and contribute a comparable fraction of peak demand [1]. Many building loads are flexible and deferrable. When a communication and management system is in place, the flexible loads may be controlled at varying time scales to benefit the grid while reducing the electricity costs of building owners.

The advances in information and communication technologies have made buildings more connected than ever before and catalyzed a new building design and operation paradigm termed connected buildings or connected communities. Leveraging the economies of scale, connected communities allow more cost-effective utilization of renewable energy and aggregated participation in wholesale energy and ancillary service markets, which are traditionally not friendly to individual buildings with low bidding power. Connected buildings also offer operational benefits such as improved energy efficiency, reduced carbon emissions and operation costs through energy use coordination across different buildings. Appropriate control strategies are critical to achieve the full potential of such connected technologies but the control development is a challenging task due to strong inter-building couplings and self-interestedness of participants.

This dissertation presents a series of building cluster control strategies designed to optimize and coordinate energy uses across different buildings to maximize their support to electric infrastructure operations and planning. Through these strategies, building end uses can be dynamically controlled to help meet grid operational requirements and reduce overall system costs, while still satisfying the comfort and productivity needs of occupants. Figure 1.1 shows a classification of building cluster control strategies based on the control time frequency and mode of inter-building coordination. According to the control time scale, control strategies may be categorized into two groups, namely load modulation and load shifting, following the classification of grid services by US Department of Energy [2]. In load modulation services, buildings vary their loads in real time (or every few seconds) to closely track reference grid signals. Reported modulation services from buildings include frequency regulation, spinning reserves and distribution voltage support. For load shifting control, a flexible load is shifted from peak hours to off-peak hours, usually through pre-cooling or pre-heating actions, and peak demand is reduced in response to grid constraints or time-of-use (TOU) price signals. Coordination across different buildings can be achieved through either a dictator scheme or a market-based approach. A dictatorial operation mode assumes that the grid operator, utility, or a third-party aggregator can control building appliances directly through a communication infrastructure. Direct load control (DLC), a voluntary curtailment program offered by most of utilities in the US, is a good example of the dictator scheme. If enrolled in a DLC program, a customer will receive a communication-enabled thermostat by which the utility provider can remotely switch off the air-conditioner or heat pump during high demand hours. On the other hand, the market-based mode allows coordination of different end users through an energy market where load changes are incentivized by properly designed pricing signals. The wholesale electricity market is an example of this operation mode although at a large scale.

There have been extensive research on dictatorial or centralized control strategies for building cluster load shifting. However, research on the other three categories is scarce. This dissertation focuses on two out of the three under-researched categories, namely dictatorial load modulating strategies and market-based load shifting control. The load modulation control strategies are discussed using a specific grid service (distribution network voltage regulation), while the market-based control is achieved through a game-theoretic control framework. The fourth category, i.e., market-based load modulation control, is not covered since it has limited practical value to manage a market with a clearing time of a few seconds.

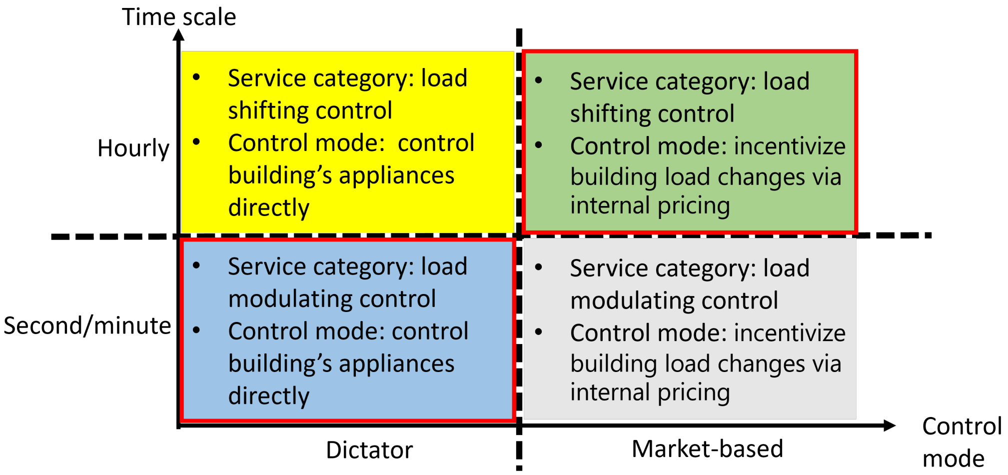

Figure 1.1: Classification of building energy control strategies

Building cluster control strategies for distribution voltage regulation can reduce voltage fluctuations and voltage regulator operations caused by unstable PV power output. Two voltage control methods are presented. The first approach is to control variable-speed HVAC systems to let their power use follow the volatile PV output, as a means to mitigate fluctuations in the net demand. To achieve this control capability, I developed a PV smoothing control strategy for variable-speed HVAC equipment and verified its performance through HIL tests, combining a 33-bus distribution feeder model and an actual 3-ton heat pump. The control strategy is comprised of multiple control blocks including a PV power smoothing filter, power flexibility estimator, power tracking controller, and zone temperature regulation controller. Key laboratory test results are reported. The second method of voltage support is through coordination of a fleet of small commercial and/or residential buildings. More specifically, a centralized control strategy was developed that coordinates the operations of HVAC equipment and hot water heaters across different households in a residential community to provide proactive voltage support against volatile solar generation. A co-simulation framework that integrates EnergyPlus models for residential dwellings (e.g., 100 houses in the case study), a PV model for solar power generation, and a 33-bus distribution network model was established to test the effectiveness of the coordinative control strategy in reducing distribution voltage fluctuations.

Market-based building cluster load shifting is achieved through game-theoretic control strategies designed to flatten the aggregate load profile and to provide efficiency support to the grid. Two market-based load shifting control methods were developed: (1) market-based game-theoretic control for peak demand reduction and (2) market-based game-theoretic control for flexible load dispatching. Both load shifting strategies leverage thermal network models to characterize the dynamics and constraints of building thermal loads. The peak demand reduction control involves a demand charge, which is proportional to the monthly peak demand of the whole aggregation and is a coupled cost for different buildings. To allocate the collective cost among participants, a Shapley value-based allocation mechanism, along with a log-sum-exponential approximate of the non-differentiable max operator, was proposed to solve the aggregate demand reduction problem. For this mechanism, I have proved the existence and uniqueness of the NE. A centralized and a distributed algorithm were developed to find the NE. In the flexible load dispatching game, different cost functions were considered to capture the impact of total power demand on the marginal cost of electricity generation, and the existence and uniqueness of NE under the different cost functions are discussed. A distributed best response algorithm was developed to find the NE of the dispatch game. A six-building simulation case study with a linear cost function has been used to evaluate the performance of the game-theoretic control for flexible load dispatching, along with two benchmarking control methods.

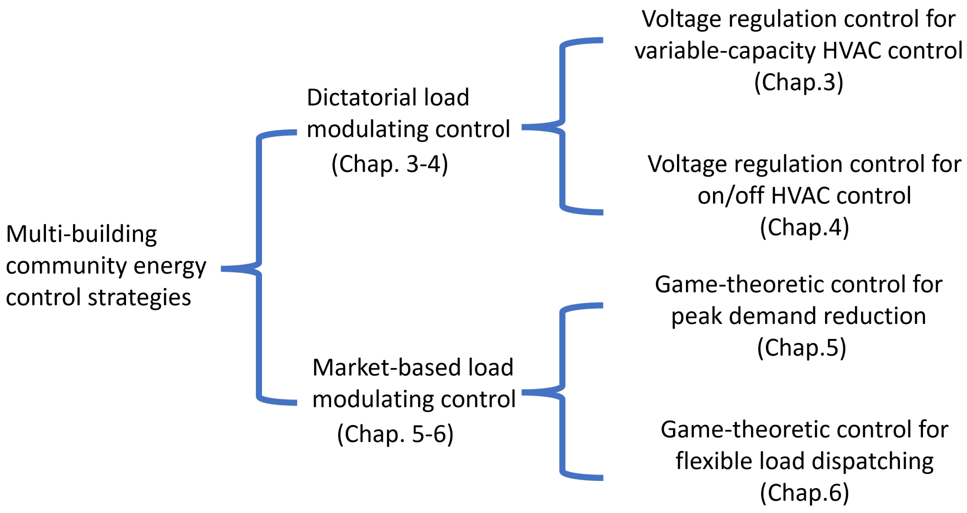

Figure 1.2: The structure of this dissertation

Figure 1.2 illustrates the overall structure of this dissertation. In Chapter 3, a voltage regulation control method for variable-capacity HVAC systems is introduced, which is comprised of multiple control blocks including smoothing filter, power flexibility estimator, power tracking controller and zone temperature regulation controller. To evaluate the performance of the control strategy, experimental tests are carried out with a HIL testbed, which integrates a 3-ton heat pump (hardware) and numerical models for a representative building and a 33-bus distribution network with high PV penetration. In Chapter 4, a voltage regulation control method for cycling HVAC systems is presented. A co-simulation platform along with the component models for the residential building prototypes, a power distribution grid and solar PV is used to evaluate the performance of the control strategy. Chapters 5 and 6 introduce two market-based load shifting control methods. Chapter 5 provides an overview of the fundamentals of convex optimization, game theory, and VI problems and introduces a game-theoretic control problem for demand response aggregators whose electricity cost includes a demand charge and a TOU energy charge, while Chapter 6 focuses on game-theoretic control for flexible load dispatching under various marginal pricing models. Concluding remarks are provided and potential future work is discussed in Chapter 7.

CHAPTER 2

LITERATURE REVIEW

A thorough review of relevant prior work is presented in this chapter according to the two building cluster control categories discussed in the introduction: (1) building clusters' participation in regulating voltage of distribution networks with high PV penetration and (2) market-based game-theoretic control of building clusters for reducing the peak demand and operational cost.

2.1 Voltage Regulation Control for Building Clusters

The growth of renewable energy utilization will continue in the years to come due to fast declining installation costs and state initiatives to pass renewable portfolio standards in order to diversify their energy supplies, stimulate economic growth, and decrease greenhouse gas emissions [3]. On May 9, 2018, the California Energy Commission established rules and became the first U.S. state to require PV panels in new homes constructed after January 1, 2020 [4]. The rising deployment of renewable energy provides considerable problems to the power grid in maintaining reliable and stable operation due to the increased unpredictability in power production, despite its importance in achieving a sustainable energy eco-system. Voltage variations beyond the regulatory limits, bidirectional power flows, and harmonic distortion in the current and voltage waveforms may result from the unpredictability of renewable resources, such as solar and wind power [5]. Operational challenges arising from the utilization of renewable energy include dynamic power system behavior on time scales ranging from microseconds to hours.U.S. Department of Energy (DOE) research shows that when the yearly energy contribution of renewables hits 20%, the present power infrastructure in the California market has to be curtailed by at least 30% [6]. Power system operators are continuously looking for ways to increase their capacity to accommodate renewable energy with mitigating their negative effect on grid stability and capacity [7]. Technologies are being investigated to minimize the fluctuation of renewable energy generation in response to these system integration needs [8]. Most of the technologies are targeted at intermittency mitigation of PV output, which involves the most aggressive fluctuations.

When solar irradiance rises, curtailment and dump load controls reduce the effective energy production, which slows the upward ramping of PV output. Traditional curtailment strategies operate the system below the maximum power point (MPP) to limit power production, whereas the dump load control employs a resistor to consume and dump a part of the available power to minimize generation [9, 10]. Even though they're simple to deploy, these strategies have a negative effect on both productivity and asset value. In addition, both strategies can only be used to reduce upward ramping, and they are unable to lower downward ramp rates. It is possible to reduce the fluctuation in output by using a combination of dispatchable generation, such as diesel and natural gas generators, with PV and wind resources [11]. However, the problem is that these dispatchable generating assets are often sluggish and cannot be utilized to regulate high-frequency ramp rates at all.

2.1.1 Control Methods for Smoothing Solar Power Output

Controlling renewable generation through energy storage has been studied, and all have a common control logic: charge the storage during overgeneration periods and discharge to satisfy the load when renewable power is constrained. Because of its high power-to-energy ratio and its ability to store rotating energy, the flywheel has been employed for PV smoothing control in a variety of ways [12]. However, flywheels have degraded performance for long-term energy storage due to friction losses and are not suitable for mild days with intermittent power fluctuations. Compressed air energy storage (CAES) is another mechanical storage device that has been utilized to manage the ramp rate of PV [13]. During period of low PV output, the compressed and pressurized air from the storage tank can be sent to a turbine, which generates power using the excess PV power. Both flywheels and CAES are mechanically based and have advantages such as reduced initial costs, longer life spans, and smaller environmental impacts compared to electrochemical energy storage. However, their overall round-trip energy efficiency is lower, ranging from 40% to 70%. The use of supercapacitors for renewable mitigation control has recently been investigated [14]. Due to their better life cycle performance and high power density, supercapacitors are a viable option for applications which require dynamic storage. However, material reliability difficulties and high capital costs make them uneconomical for large-scale utility use. A good number of strategies were proposed in the literature for control of battery charging/discharging for PV smoothing, most of which applied smoothing filters to obtain smoother net generation from raw PV output. Both moving-average [15] and full term low-pass filters [16] were proved effective for PV generation smoothing. The major drawback of filter-based algorithms is the delayed estimation of the PV output midpoint because of the memory effect. Ramp rate limiting control, a special type of filter, is only concerned about the power output change between consecutive time steps and attempts to limit the change within a given threshold. Compared to low-pass filter algorithms, the ramp-rate control requires minimum computing and memory resources and involves reduced battery energy throughput leading to lower round-trip energy losses and improved life time [17]. However, the ramp-rate control solution typically requires greater battery sizes to prepare for both upward and downward ramping.

2.1.2 Modulation Services from HVAC Systems

Due to buildings' intrinsic thermal inertia, HVAC systems in buildings are great candidates for modulation services such as power frequency and voltage control. Variable-speed supply fans [18, 19], electrical space heaters [20], chilled-water pumps [21], residential heat pumps [22], water heaters [23], commercial-scale chillers [24], and packaged air-conditioning equipment [25] have been studied for regulatory service. In addition to providing frequency regulation assistance for the bulk power grid, HVAC equipment was effectively employed for frequency support of microgrids [26, 27] and load following in minimizing variations in renewable power [28]. The published results have demonstrated a variety of advantages of using HVAC equipment for modulation services compared to other resources:

- Fast response: a majority of the power associated with building thermal systems is consumed by electric motors which have fast power response to speed changes [29];
- Low capital cost: almost all buildings have HVAC systems installed and the cost to enable the smoothing control capability in existing equipment is marginal compared to installation of new storage systems;
- No round-trip efficiency loss: charging and discharging a thermal system involves no additional heat loss compared to normal operation, leading to little to no opportunity costs for provision of smoothing control [30];
- Environment-friendly compared to batteries and fossil fuel plants, especially with the shift to low- or zero-GWP refrigerant.

However, in residential and light commercial buildings, the relatively limited power capacity of a single building represents a significant impediment to the contribution of buildings to frequency regulaton. There have been efforts to develop aggregation solutions for the frequency regulation control of multiple buildings in order to overcome the size challenge of frequency regulation in a single building and provide an acceptable size of regulation capacity by aggregating or coordinating different buildings in a cluster. For example, references [31, 32] have developed and experimentally tested a hierarchical frequency regulation control method using variable-speed supply air fans in commercial buildings. A supervisory reserve scheduler, a room controller, and a local regulation signal tracking controller were integrated to identify the next day regulation reserve capacity. The reserve scheduler is based on a similar approach to that of the study [33] by explicitly addressing the randomness in the regulatory signal. The studies in [32, 31, 33] relied only on supply air fans for frequency regulation. Fan control is straightforward, but its power capacity is much lower than that of HVAC compressors.

2.1.3 Control Methods for Distribution Network Voltage Regulation

Voltage regulation devices used in traditional distribution grids include on-load tap changer (OLTC), shunt capacitor and step voltage regulator (SVR). These devices are primarily designed to mitigate slow diurnal voltage variations and not suitable for rejecting dynamic disturbances caused by deep PV integration. For more effective distribution voltage management, hybrid methods have been investigated that combine legacy voltage regulation devices with emerging technologies such as PV power curtailment [34], reactive power control through smart inverters [35, 36], electrical batteries [37] and smart load management [38]. PV inverter Volt-Var control can be implemented either in a completely decentralized manner through a droop logic based on local voltage measurements [35] or in a centralized scheme where the reactive power injection/absorption at different nodes are managed by a central coordinator [36]. The local and decentralized method may cause voltage instability due to lack of synchronization across the different devices. Although the centralized approach is able to maintain stability with appropriate coordination, a communication infrastructure is required and the communication delay may jeopardize the overall control performance. In reference [39], energy storage was used along with tap changer transformers to regulate voltage and reduce tap operations in case of high PV penetration. When voltage rises, the transformer tap position is firstly changed and then the energy storage system is charged; on the occasion of peak load, coordination signals will be sent to discharge the distributed energy storage in order to mitigate voltage drops.

2.1.4 Building-to-Grid Co-Simulation Platform

Co-located with distributed generation in a PV-rich distribution grid, building flexible loads can be leveraged for distribution voltage support. To facilitate optimal controller design and performance assessment, a high-fidelity numerical tool is needed for the distribution grid that can capture realistic dynamics and the diverse patterns of building flexible loads. To this end, a co-simulation approach, leveraging and linking disparate simulation tools across different disciplines, appears to be suitable. In the field of building performance simulation, a co-simulation approach has been adopted to accommodate different types of simulation analysis and most of prior studies utilized whole building energy simulation programs (e.g., EnergyPlus) paired with other numerical tools. For example, studies combined EnergyPlus and MATLAB/Simulink framework to investigate the influence of weather as well as construction materials on the room and ventilation temperatures [40] and to support assessment of an occupant-oriented mixed mode predictive controller [41]. Another study co-simulated a building's energy performance and the outdoor micro-climate by linking EnergyPlus and ENVI-met, to study the impact of different types of green roofs on the cooling demand for different climate conditions and urban densities [42]. Analysis of phase change materials (PCM) for thermal management of buildings was performed with an EnergyPlus and ANSYS Fluent co-simulation setup [43]. The above studies have shown good success of co-simulation with the high fidelity EnergyPlus toolset and other simulation platforms to accommodate cross-disciplinary analyses. Some power system simulation tools, e.g., GridLAB-D [44], incorporate simplified building models that cannot capture some of the important load dynamics, such as heat pump efficiency variations caused by cyclic operations and dehumidification. Most relevant to this study, the Transactive Energy Simulation Platform (TESP), developed by the Pacific Northwest National Laboratory, allows the implementation and control of EnergyPlus building models on the feeder level and provides co-simulation capability across different simulators including GridLab-D, EnergyPlus, OpenDSS, PyPower, NS-3, among others.

2.2 Market-Based Game-Theoretic Control of Building Clusters

To improve the robustness and efficiency of the grid, an aggregator is needed across a number of users to unite the users in the grid and regulate the power usage strategies of users in response to the dynamic unit electricity price, allowing for more efficient energy usage. One method for aggregator is to find the above optimal strategy centralized [45, 46, 47], with the aggregator defining user's power consumption strategy profile over the time horizon. This, however, is a quite aggressive method, as it needs each user to supply extensive information on user's power consumption. Indeed, these concerns about privacy may prevent demand-side users from subscribing to the optimization process. The computational complexity of centralized system will increase significantly as the number of buildings increases, which makes the centralized approach incapable of accommodating an increase in the aggregation size. Additionally, a cooperative solution may sacrifice some individuals' utilities or quality of services (e.g., uncomfortable indoor temperatures) to achieve social optimality, and rational players may leave the alliance for their own benefits, leading to an unstable coalition.

To address the above mentioned social and technical barriers, a non-cooperative game solution be considered. The non-cooperative game provides the aggregator with a distributed operation mode in which each individual only considers his/her own optimization objectives and constraints. There is a lot of game relevant research that focuses on load management (demand side) [48, 49, 50, 51, 52] and energy source management (supply side) [53, 54, 55]. For the demand side, users are the game's participants and the goal of the users is to reduce their own electricity cost by scheduling their electricity usage profiles. In this framework, the users can obtain information of other users and energy unit price from the electricity market to optimize their control actions. For the supply side game, each user engages in a game with the electricity provider, where the electricity provider, as a leader, maximizes their profit by setting price and users as the followers adjust the power demand accordingly. These non-cooperative strategies can be divided into two sub-categories: dynamic games and static games.

2.2.1 Dynamic Game in Building Energy Management

For a dynamic game, also called sequential game, there is at least one player who chooses their strategy according to which the others make their decision. The later players must have information about the former player's actions. Therefore, the time plays a key role in decision making. The Stackelberg game that is commonly used in smart grid solutions is an example of dynamic games. For instance, authors of [53, 54, 55] used Stackelberg games to model the interactions between the utility company and electricity consumers, where the utility company (leader) sets the price and the users (followers) adjust the power demand accordingly. When a Stackelberg equilibrium is reached, the leader's profit is maximized and all the users' costs are minimized at the identified prices. The Stackelberg game setting is not very applicable to building load aggregators since it is difficult to come up with a non-monetary utility function for individual buildings. Most Stackelberg equilibrium seeking algorithms assume easy access to closed-form solutions of the followers' optimization problems, which is not the case for building load control. In [56], the authors proposed a bi-level game framework for demand side management. On the customer side (bottom layer), a static non-cooperative game is used in which Nash equilibrium solutions are sought that minimize the individual player's electricity cost under a given price structure. As the top layer, a dynamic Stackelberg game is used to model the interactions between the utility company and the customers, in which the utility company updates the price structure to maximize its profit meanwhile minimizing the peak to average ratio (PAR). A distributed algorithm was proposed to solve the bi-level optimization problem.

2.2.2 Static Game in Building Energy Management

The static game theory has been studied extensively for smart grid applications. For instance, in [51], a two-settlement demand response strategy was proposed with day-ahead and real-time phases. The day-ahead bidding strategy was based on a non-cooperative Nash equilibrium game setting in which each player tends to minimize the expected daily electricity cost and the electricity price is proportional to the aggregated demand. The day-ahead bidding process is reformulated as a generalized Nash equilibrium problem (GNEP) and an asynchronous proximal decomposition algorithm is used to find the variational solution of the GNEP by relaxing the coupling constraints. The study assumed a simple load model without any temporal couplings. In reference [52], the authors presented a Nash equilibrium-based strategy for demand-side management to reduce the PAR and energy cost. A heuristic method was used to distribute the aggregate generation cost among the consumers based on their respective shares of total daily energy use. The consequence of this treatment was that the same cost function was involved for all players, transforming the non-cooperative game into a homothetic cooperative type. A block coordinate decent-type algorithm was used to solve the Nash equilibrium problem. In reference [57], the authors proposed a Vickrey-Clarke-Groves (VCG) cost allocation mechanism which ensures each user's objective function aligns with the social planner's objective function. Therefore, the users cannot do better than truthfully declaring their demand information to the energy provider, who determines the payment and the power consumption strategy of each user according to the Nash equilibrium of the VCG mechanism. In this framework, customers are requested to share their power demand information, which is used by a centralized operator for the price calculation. In static game applications, existing game-theoretic controls for demand side management primarily used pricing mechanisms to incentivize costumers to change their power consumption strategies. The existing social cost functions are mostly strictly convex. For instances, a quadratic social cost function was used in [52, 58]; a logarithmic social cost function that ensures users are able to sell energy back to the grid was used in [56] and a power function was used in [59].

Algorithm for Game Theoretic Control

To solve the game problem and find the NE, the following three methods are most commonly used:

- *Best response algorithms.* These algorithms allow (semi-)distributed implementations. Therefore, they are often employed by engineers and practitioners for problem solving. There are two types of distributed implementations: Jacobi (simultaneous iterative algorithm) and Gauss–Seidel (sequential iterative algorithm). These algorithms are simple to implement, but the convergence conditions can be very restrictive. They are often utilized for problems with specific structures, e.g., potential game [60] and supermodular game [61].
- *VI algorithms.* For NE problems with completely decoupled action sets, VI-based algorithms can be more suitable, e.g., methods of projection (extragradient method by Korpelevich [62]; hyperplane projection by Konnov [63]), Tikhonov regularization [64], proximal point [65] and splitting [66]. VI algorithms often feature better global convergence properties, but may be more computationally demanding in comparison to best response algorithms.
- *Nikaido-Isoda function (NI) algorithms.* For generalized NE problems, e.g., the distribution voltage regulation problem where a player's action set is dependent on the actions of others, the NI function-based approach may be more appropriate [67, 68].

This approach converts a (G)NEP into a saddle point problem using the Nikaido-Isoda (NI) function, and then uses classic saddle point algorithms to find the NE. A semismooth Newton's method with a backtracking (geometric) line search can be used to find the stationary point of a complementarity reformulation of the merit function [69]. This algorithm can solve not only NE problems but also GNEP [70].

2.3 Review Summary and New Contributions of the Present Work

Based one the review results, it is apparent that there has been limited research work on grid-responsive building cluster control under the dictatorial load modulation or market-based load shifting categories, as shown in Figure 2.1. Most of the existing building cluster control methods were synthesized on a hourly time scale to control electrical equipment in buildings with a dictatorial operation mode [46, 71, 72, 73] This dissertation fills the gap on dictatorial load modulation and market-based load shifting by a series of new control strategy development. Specifically, the present work makes unique contributions in the following aspects:

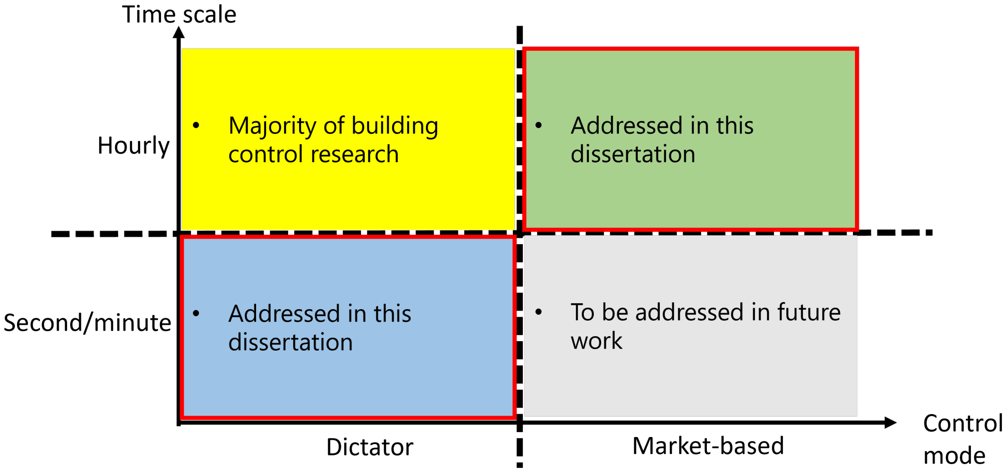

Figure 2.1: Classification of building energy control strategies

- *Voltage regulation.* This dissertation introduces a completely new method for solar power smoothing by utilizing novel voltage regulation control strategies for building thermal equipment, which is operated on a second/minute time scale under a dictator mode.

- *Cost function.* Previous studies for game-theoretic control for demand side management considered cost functions that are smooth and strictly convex, e.g., quadratic cost function [52, 58], logarithmic cost function [56], and power function [59]. The present study is first to use a non-smooth convex cost function (max function).

- *Split pricing mechanism.* Prior work used simple social cost split methods, e.g., assuming an individual's share of the social cost is proportional to their total power consumption. which is difficult to make the optimal decisions of individuals consistent with the global optimum. In addition, the heuristic cost splitting mechanism is hard to maintain the stability of the alliance. To overcome the shortcomings mentioned above, the present work adopts a shapely value-based allocation mechanism that is fair and efficient.

- *Existence and uniqueness of NE.* The existence and uniqueness of NE for the peak demand reduction game problem with a Shapley value-based split function were proven. This study also proved the existence and uniqueness of NE for the flexible load dispatching game problem under an exponential marginal price model and a power marginal price model.

- *Centralized algorithms to find NE solution.* A centralized algorithm is proposed for the game problem based on a customized proximal point algorithm for the VI [74]. Compared with the previous VI algorithms, this algorithm features accelerated convergence by designing the regulation coefficient according to everyone's constraints before reformulating the game into a VI form.

CHAPTER 3

DISTRIBUTION VOLTAGE SUPPORT USING VARIABLE-CAPACITY HVAC SYSTEMS

This chapter presents a voltage regulation control method for variable-capacity HVAC systems that are designed to pair with solar PV applications. However, the method can also be applied for intermittency mitigation of other renewable resources. Section 3.1 introduces a building-to-distribution grid simulation model that covers components commonly encountered in a PV-rich distribution grid. Section 3.2 introduces a PV smoothing control strategy, a voltage regulation control method using variable-capacity HVAC systems. The control strategy is comprised of multiple control blocks including a smoothing filter, a power flexibility estimator, a power tracking controller and a zone temperature regulation controller. Section 3.3 describes a HIL testing methodology used for performance assessment of the proposed control method. The experimental setup, simulation models for the distribution network and buildings, and their interactions are discussed. Section 3.4 presents and discusses the key test results. A chapter summary is given in Section 3.5.

3.1 Building-to-Distribution Grid Model

This section introduces a building-to-distribution grid simulation model covering components commonly encountered in a PV-rich distribution grid. This model is utilized to assess and evaluate the PV smoothing performance of various HVAC systems (variable-capacity HVAC systems in this chapter and cycling HVAC systems in Chapter 4). The building-to-distribution grid system simulation includes models of residential dwellings, a radial distribution feeder, solar PV panels uniformly distributed across the feeder, a step voltage regulator (SVR) and a central control system. These component models are elaborated in the subsequent sections.

3.1.1 Power Distribution Network Model

The voltage regulation strategy can bring a variety of benefits to the electric grid. One of the performance improvements is in voltage regulation for distribution networks having high PV penetrations. Voltage variation caused by renewable intermittencies has been recognized as one of the main barriers for deep integration of distributed generation into low- and medium-voltage distribution networks [75, 76]. The HVAC system voltage regulation strategy aims to reduce the variability of net demand/generation, which will consequentially stabilize the distribution voltage and minimize the adverse impact of renewables on the life time of legacy voltage regulation devices. Figure 3.1 shows the test distribution system used in the case study, which consists of 33 load buses and has a nominal apparent capacity of 4.55 MVA, which is also the summation of nominal capacities of all the load buses in this distribution network. The distribution grid model has packaged as a nonlinear steady-state power flow

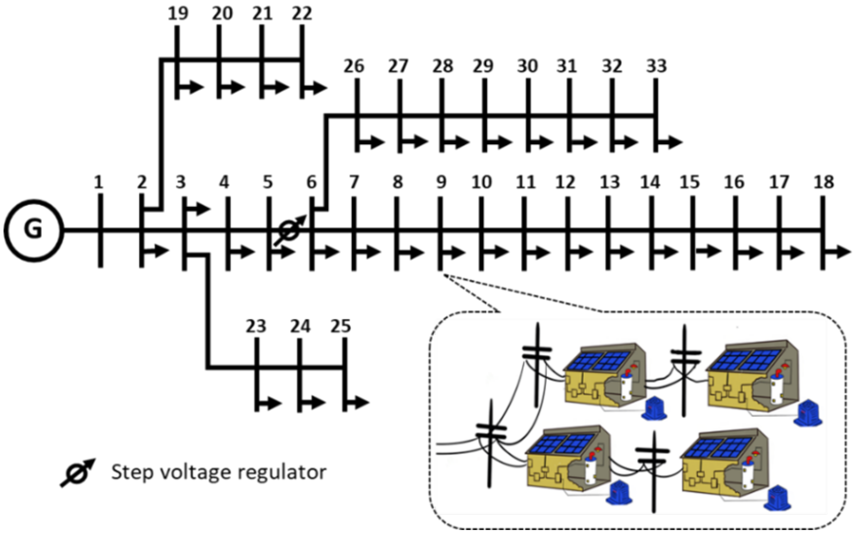

Figure 3.1: Residential distribution network in the case study

model to simulate voltage variations of a distribution system and a Newton-Raphson method for equation solving [77]. The distribution grid model can be executed at various time steps (e.g., every second in this chapter and every minute in Chapter 4) to calculate the distribution voltage given the instantaneous loads and PV output. Note that the nonlinear power flow model is not suitable to use in iterative control algorithms due to the high computational demand. To improve numerical efficiency, the grid simulator also incorporates a routine to generate a linear approximate of the power flow model based on the linearization approach proposed by Baran and Wu [77] for radial networks. This approach neglects the line loss terms but captures the reactive power contribution to voltage drops. The linear surrogate model is used in the controllers discussed in Section 4.2. However, it should be noted that the voltage simulation results presented in this chapter were all obtained with the nonlinear power flow model.

3.1.2 Step Voltage Regulator

As shown in Figure 3.1, a SVR is assumed to be installed between buses 5 and 6 to compensate for voltage drops along the radial distribution line. A SVR is primarily designed to maintain a constant secondary voltage under time varying load and distributed generation, which are known to be highly influenced by weather events and can fluctuate drastically [78]. It is an autotransformer that can vary the turns ratio through automatic tap changing to achieve voltage regulation. For conventional grid operation with no or low PV penetrations, SVRs work along with on-load tap changers and/or capacitor banks to regulate voltage on a distribution network against diurnal load variations. Figure 3.2 compares the voltage profiles along the feeder with and without SVR, at the nominal load conditions and without PV integration. It can be seen that without SVR, the voltage of the buses at the far end of the feeder would drop below 0.95 p.u. and violate the ANSI C84.1 Standard [79]. The SVR installed after bus 5 can boost the voltage of downstream buses to be in compliance with the standard.

It may be noted that the SVR secondary voltage is typically set at a slightly higher value, e.g., 1.05 p.u., to compensate for large voltage drops in a long radial network. However, the tests conduced in this study assumed a setpoint of 1 p.u. at bus 6 to prevent overvoltage issues due to distributed PV penetration.

Growing installations of solar PV generators in distribution systems may cause frequent variations of distribution voltage and overstress voltage regulation devices [80]. To quantify this impact and capture potential benefit of the proposed voltage regulation solution on operations of voltage regulation devices, a SVR installed in the middle of the feeder is considered. Most utility SVRs are able to modulate the output (secondary) voltage in the range of 90% to 110% of the input (primary) voltage. This regulation is usually accomplished in 32 discrete steps so that each step would result in 0.625% or 0.75 V voltage change on a standard 120 VAC base. The 32 steps are equally divided between -10% and +10% so there are 16 steps each for voltage boost and reduction. In this study, the SVR is operated to maintain the secondary voltage (of bus 6) within a prescribed deadband through adjusting the tap position. Two different deadband settings, i.e., $\pm 0.625\%$ (± 0.75 V) and $\pm 1.6\%$ (± 2 V), are simulated to evaluate the impact on operation behaviors. Most SVR controllers apply a time delay to prevent too frequent tap operations; a tap position change is only executed when the voltage stays out of the deadband for a minimum duration. A time delay setting of 30 seconds is assumed in this study [80, 81].

3.1.3 PV Integration on Distribution Network

For simplicity, it is assumed that solar PV panels are installed across all buses in the distribution network with identical penetration levels. The PV penetration at a distribution node is defined as the ratio of the total nameplate capacity of solar PV systems to the nominal apparent load of the bus. Only real power is assumed to be injected by the PV panels. For each bus, power consumption of all the connected buildings and solar power output calcu-

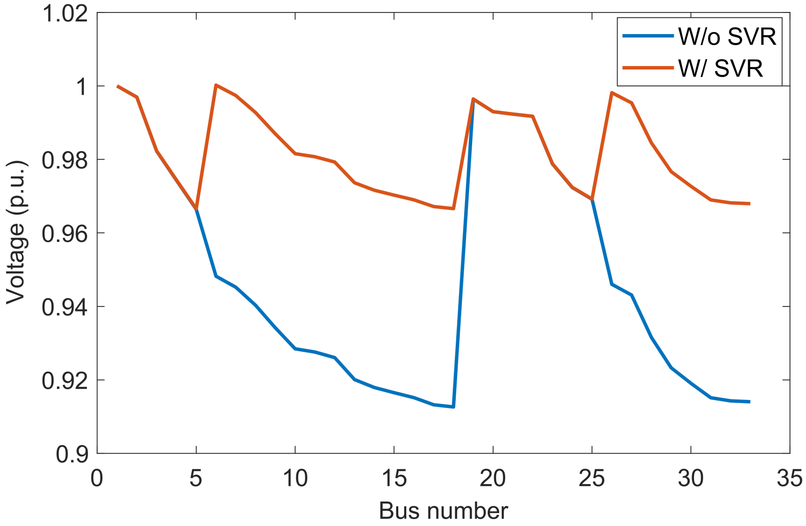

Figure 3.2: Feeder voltage profiles with nominal load and without PV.

lated from the solar PV model are both scaled to match the nominal capacity of that bus. Therefore, the solar power fluctuations across the different buses are all synchronized and the test performance presented in this chapter corresponds to the worst case scenario without considering geometrical averaging effect. An actual distribution network at the same PV penetration level would experience smaller disturbance due to the averaging effect among a large number of PV panels in the service territory.

3.1.4 Building Thermal Capacitance Model

In this study, building load profile was generated with the DOE prototypical building model using EnergyPlus, a whole building energy simulation tool developed and maintained by the U.S. Department of Energy (DOE). HVAC loads are regarded as the major flexible loads and all other electrical end consumers, e.g., lighting, computers etc., are assumed to be non-controllable [82]. The HVAC systems power modulation required by the voltage regulation control leads to fluctuations in the cooling effect delivered by the HVAC system and may adversely impact indoor comfort. Therefore, operational (and load) flexibility of HVAC equipment is affected by the building thermal inertia and HVAC anti-cycling time settings, both of which affect and thereby can be correlated with the HVAC cycling patterns. To accurately capture this effect, a lumped capacitance building thermal model is implemented to emulate indoor environmental variations during voltage regulation and details of the model are presented as follows.

The following thermostat model characterizes the HVAC cycling frequency with respect to the runtime fraction X [83]:

$$N = 4 \cdot N_{max} \cdot X \cdot (1 - X) \tag{3.1}$$

where N is the number of duty cycles in each hour and N_{max} is the peak cycling rate which occurs at $X = 0.5$. The runtime fraction is defined as the ratio of the HVAC run time in one duty cycle to the total cycle length, which is also close to the ratio of the building load to the HVAC cooling capacity [83]. Figure 3.3 shows the variation of the HVAC cycling rate with the run time fraction from one of the simulated case study buildings in EnergyPlus (after modification of the effective capacitance, to be discussed in the following paragraph); the bell-shaped curve represents the best fit of Section 3.1.4 to the simulation results with N_{max} close to 3. It can be observed that the cycling rate is low for periods with very low or very high load ratios, while the cycling rate peaks at a run time fraction of 0.5. The building thermal capacitance can be estimated based on a cyclic thermostat model

$$C_{bld} = \frac{Q_{rate}}{8 N_{max} T_{db}} \tag{3.2}$$

where Q_{rate} is the rated cooling capacity of the HVAC system. T_{db} is the thermostat deadband and N_{max} is the maximum compressor cycling rate per hour, for a single-stage HVAC unit. It may be noted that the thermal capacitance C_{bld} combines the thermal inertial associated with the indoor air volume, air-to-furniture/wall interactions and thermostat enclosure. For given HVAC capacity and thermostat deadband, the maximum cycling rate is inversely

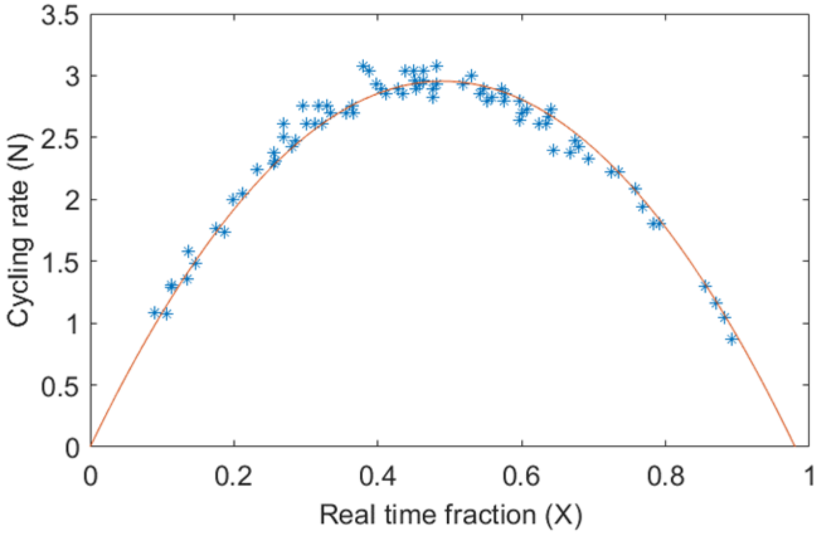

Figure 3.3: Cycling rate vs. run time fraction for an example EnergyPlus building model

proportional to the combined thermal capacitance, which is a relatively constant parameter for a given house. Due to the relationship with the combined thermal capacitance, peak cycling rate is an important parameter and realistic estimates thereof are critical to capture the aggregate flexibility. Henderson et al. collected high-resolution thermostat data from more than 10 single-family residential dwellings in Florida and found the peak cycling rate ranging from 2.4 to 3.5 [83]. Note that the thermal capacitance is derived based on the thermostat cycling model subject to an on/off HVAC unit. However, the case study considered in this chapter involves a variable-capacity HVAC system that can continuously modulate its cooling power to regulate the temperature.

3.2 PV Smoothing Control Strategy

Figure 3.4 depicts the proposed overall PV smoothing control strategy for variable-capacity HVAC systems. At each decision time step, the PV generation and building thermal load need to be pre-conditioned to estimate the respective base power, which is used to identify the HVAC power setpoint on the fly. The control method consists of three major control modules: 1) a low-pass filter to estimate the base PV power, a midpoint around which the actual PV output fluctuates, 2) a HVAC power flexibility estimator that takes the instantaneous cooling load and generates the upper/lower bounds for HVAC power modulation, and 3) a power tracking controller that modulates the compressor speed to follow the identified power setpoint. The pre-conditioning step ensures energy neutrality in the compensating power so that the average building thermal load can be met to maintain indoor comfort. The various control modules are elaborated as follows.

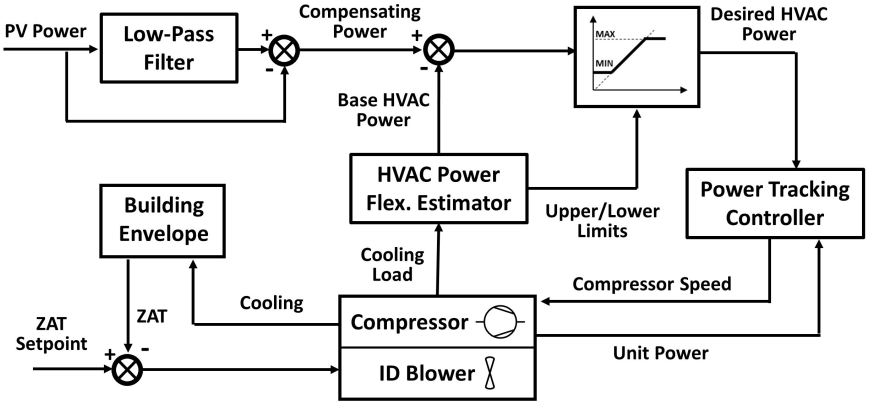

Figure 3.4: Overall control diagram

3.2.1 Voltage Regulation Low-pass Filter

A moving-average filter is implemented to identify the midpoint of PV power fluctuation during partly cloudy and partly sunny days. The difference between the filter output and the instantaneous PV power, termed compensating power, should ideally be offset by smoothing resources such as building thermal loads in order to obtain a relatively smooth net generation/demand. In the experimental tests, a 30-minute time window and uniform weights were assumed in the implemented moving-average filter. Figure 3.5 shows the raw and filtered PV power output, based on field power measurements of a 14 kW solar plant. The 30-minute data used in the experiments is also highlighted.

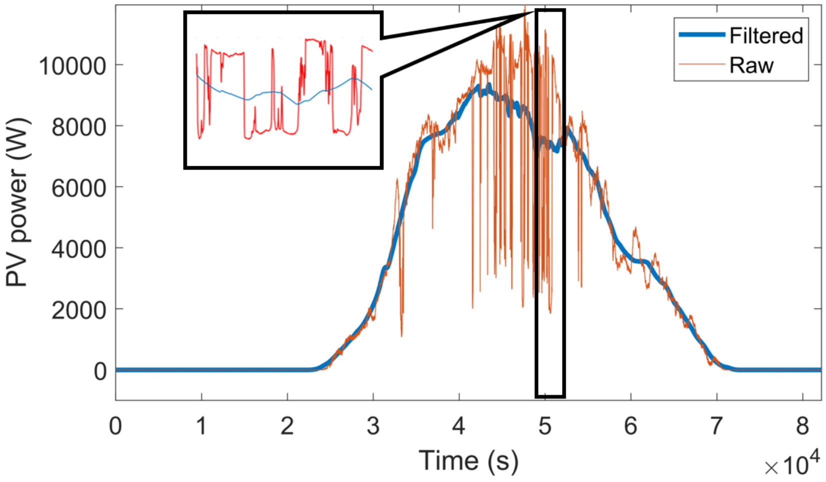

Figure 3.5: Raw and filtered diurnal PV power.

3.2.2 HVAC Power Flexibility Estimator

HVAC systems are primarily designed to maintain indoor comfort, which represents a major constraint in determining control actions for voltage regulation. Therefore, it is critical to develop a method to estimate the HVAC power flexibility, dictated by the base power and the upper/lower limits. During PV smoothing control, the HVAC power is modulated around the base level and within the upper/lower limits to absorb excessive fluctuation of PV output. As long as the modulation power is energy neutral with respect to the base power, the average cooling effect and indoor temperature regulation performance would not be impacted.

a. HVAC System Model

The first task of the flexibility estimator is to identify the base compressor speed and power at a given building load. A simplified quasi-steady-state model was developed to capture the relationship between the cooling rate and HVAC power, based on a compressor map and empirical correlations on temperature differentials of the condenser and evaporator. The compressor map uses the following 20-term correlations for compressor power (P) and cooling capacity (Q) predictions:

$$P = \mathbf{c_1}^{\mathrm{T}}\mathbf{x} \tag{3.3}$$

$$Q = \mathbf{c_2}^{\mathrm{T}}\mathbf{x} \tag{3.4}$$

where $\mathbf{c_1}$ and $\mathbf{c_2}$ are the coefficient vectors, provided by the equipment manufacturer. The vector $\mathbf{x}$ is equal to $[1, T_e, T_c, R, T_eT_c, T_eR, T_cR, T_e^2, T_c^2, R^2, T_eT_cR, T_e^2T_c, T_e^2R, T_e^3, T_eT_c^2, T_c^2R, T_c^3, T_eR^2, T_cR^2, R^3]^\top$, where R is the compressor speed, and T_e and T_c are the saturated evaporating and condensing temperatures. The evaporating and condensing temperatures are intermediate variables that vary with operating conditions such as the zone/return air temperature (T_z) and outdoor temperature (T_o). The air-to-refrigerant temperature differentials, defined as

$$dT_e = T_z - T_e \tag{3.5}$$

$$dT_c = T_c - T_o, \tag{3.6}$$

drive the heat transfers on the evaporator and condenser, respectively. For variable-capacity HVAC systems, the temperature differentials are highly dependent on boundary conditions (i.e., T_z and T_o) and compressor speed. This dependence can be approximated by the following linear correlations:

$$dT_e = a_0 + a_1T_o + a_2T_z + a_3R \tag{3.7}$$

$$dT_c = b_0 + b_1T_o + b_2T_z + b_3R \tag{3.8}$$

where the coefficients a_i and b_i's can be estimated from system performance data. In this study, offline experimental tests were carried out for the test unit covering a wide range of operating conditions and linear regression was applied to obtain the coefficient values from the experimental data. It should be noted that the supply airflow could also impact the temperature differentials; this dependence is neglected in the present study since the PV smoothing strategy tends to maintain a relatively constant airflow when appropriate power limits are used. Dehumidification is not considered since all tests were carried out under dry air conditions (the sensible heat ratio is always equal to unity). Figure 3.6 and Figure 3.7 compare the experimental and model prediction results. The model is in good agreement with measurements for both cooling capacity and power predictions, with relative errors less than 10% of a majority of the points.

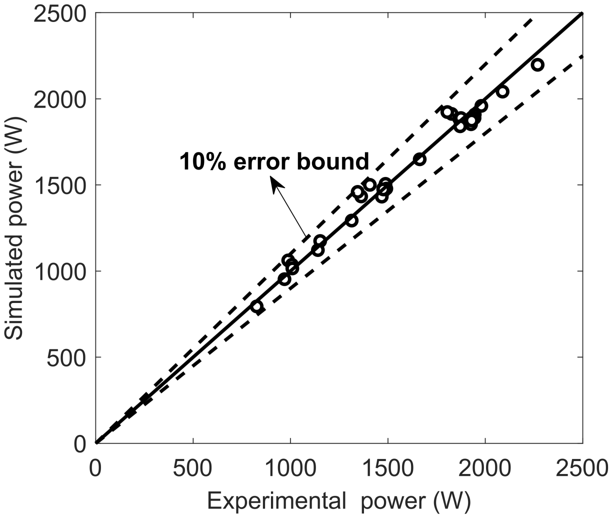

Figure 3.6: HVAC power prediction performance.

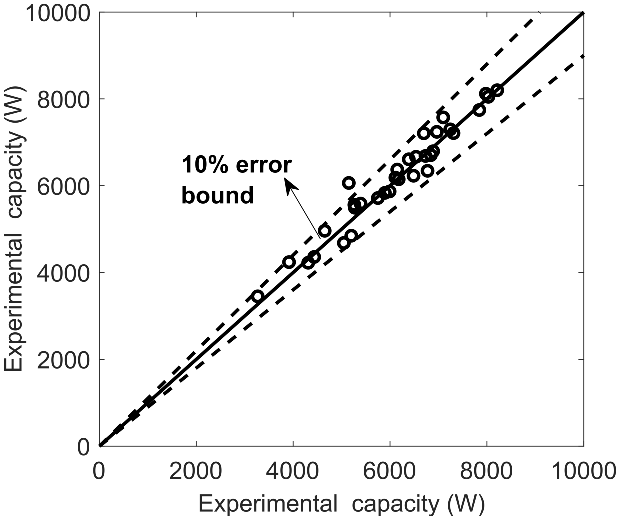

Figure 3.7: HVAC cooling capacity prediction performance.

The developed HVAC system model has an input-output form of

$$[P, Q] = \text{HVAC}(T_o, T_z, R). \tag{3.9}$$

Figure 3.8 shows the relationship between the cooling capacity and HVAC power at $T_z = 25°\text{C}$ and $T_o = 35°\text{C}$ when the compressor speed varies in the full range (35% to 100% of nominal speed). There is a clear one-to-one projection between capacity and power, which allows easy conversion from one to the other as needed in the flexibility estimator.

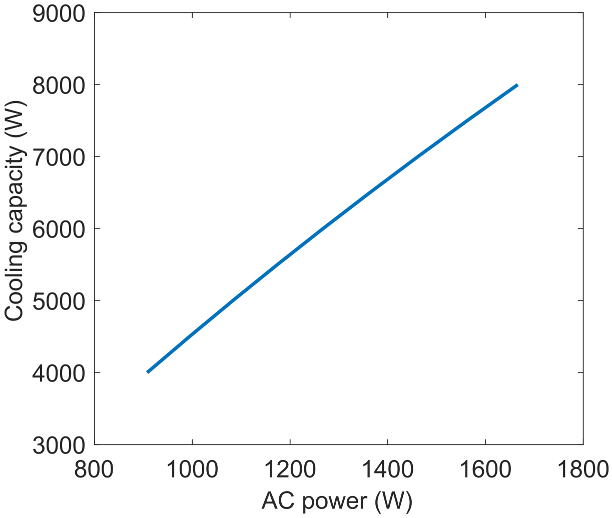

Figure 3.8: Variation of cooling capacity with compressor power, for $T_z = 25°\text{C}$ and $T_o = 35°\text{C}$.

b. Flexibility Estimator

The flexibility estimator is designed to predict the range of HVAC power modulation for given load and boundary conditions (T_z and T_o). Firstly, the upper and lower bounds of cooling output need to be identified as

$$Q_{min} = \text{HVAC}(T_o, T_z, R_{min}) \tag{3.10}$$

$$Q_{max} = \text{HVAC}(T_o, T_z, R_{max}) \tag{3.11}$$

where R_{min} and R_{max} are the compressor speed lower and upper limits. For the test unit, the lowest speed of the compressor is approximately 35% of the nominal or maximum speed. For a given cooling load Q, the modulation margin of the cooling capacity can be estimated as

$$\Delta Q = min(Q_{max} - Q, Q - Q_{min})$$

and the upper and lower bounds for capacity modulation can be found as $Q_{UB} = Q + \Delta Q$ and $Q_{LB} = Q - \Delta Q$. During PV smoothing, the cooling capacity would modulate with a midpoint equal to the load Q and ramp-up/-down margin equal to ΔQ. These bounds dictate the thermal flexibility of the HVAC system. The power flexibility, i.e., the corresponding upper and lower bounds (P_{UB} and P_{LB}) of the compensating HVAC power, can be easily estimated using the HVAC system model in Equation (3.9), since the model gives a one-to-one mapping between the power and cooling capacity. The base HVAC power is simply the arithmetic average of the upper and lower bounds

$$P_{base} = \frac{P_{LB} + P_{UB}}{2}$$

Figure 3.9 and Figure 3.10 depict the variations of thermal and power flexibilities of the HVAC system under study, for different load levels and at boundary conditions $T_o = 35$°C and $T_z = 25$°C. It can be seen that for extremely high or low load conditions, the flexibility is reduced because the base compressor speed is closer to its upper or lower bounds and the speed modulation margins are reduced attributed to the symmetric requirements for upward and downward ramping. The flexibility peaks at intermediate load conditions with maximum speed modulation margins.

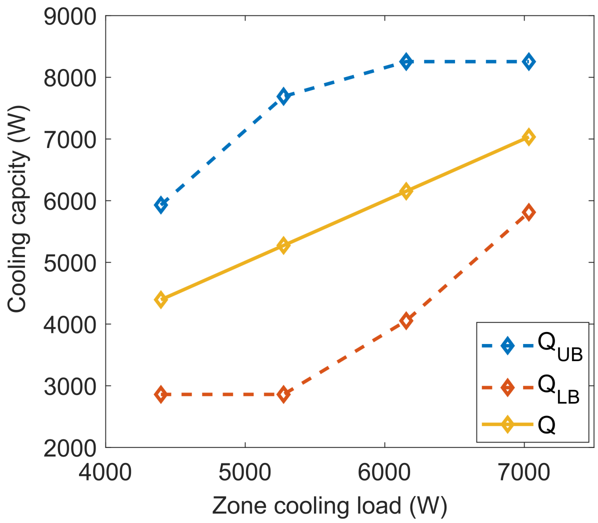

Figure 3.9: The cooling capacity flexibility at different load levels.

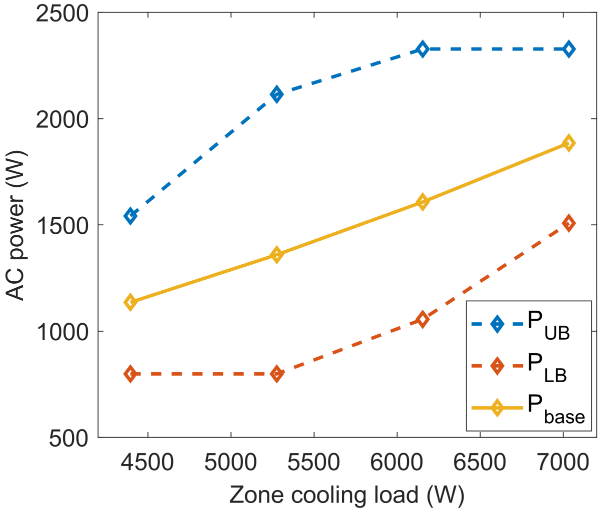

Figure 3.10: The power flexibility at different load levels.

3.2.3 Power Tracking Controller

The estimated power flexibility can be leveraged to identify the desired HVAC power, which is set to the base HVAC power plus the PV compensating power (P_{comp}), but needs to be bounded by the power modulation limits, i.e.,

$$P_{des} = \max\big(\min(P_{base} + P_{comp}, P_{UB}), P_{LB}\big) \tag{3.12}$$

A power tracking controller is designed to determine the compressor speed on the fly in order to follow the desired power level P_{des}. A feedforward-feedback approach is adopted where a feedforward block estimates the compressor speed needed to match the power set value based on the HVAC model and a feedback controller takes corrective control actions to compensate for model inaccuracies. The tracking control diagram is shown in Figure 3.11.

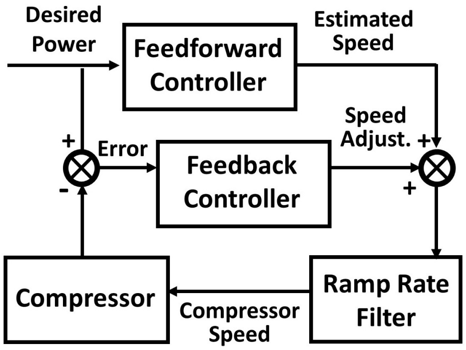

Figure 3.11: Power tracking control diagram.

The feedforward controller relies on the quasi-steady-state HVAC model described in Section 3.2.2 to obtain a rough estimate of the compressor speed for the given power set value. This is achieved through a Newton-Raphson-based numerical solver that finds the target speed R for a given power level P. This feedforward controller enables fast responses to sudden changes in the power setpoint, which is an essential requirement for PV smoothing control during partly cloudy and partly sunny days.

The feedback block is necessary to compensate for mismatches between model predictions and actual system behaviors and to mitigate steady-state errors. A proportional-integral (PI) controller is used with PI gains tuned through offline tests using the Ziegler-Nichols method. The sum of the feedback and feedforward control outputs is fed to a ramp rate filter, which enforces the ramp rate limit before the control command is sent to the compressor variable frequency drive (VFD).

3.2.4 Zone Temperature Control

The primary function of a HVAC system is to maintain desirable indoor conditions. In provision of grid services, such as voltage regulation, the building thermal load must be met by the HVAC equipment for satisfactory indoor temperature regulation. A PI-type feedback loop is used to monitor the actual zone air temperature and vary the indoor fan speed to regulate the zone temperature close to its setpoint. When the zone temperature goes beyond the setpoint, the supply air flow delivered by the indoor blower will be increased to provide more cooling to the indoor space; the reverse action will be taken when the temperature drops below the setpoint. The zone temperature control loop is designed to cope with the building envelope dynamics, which are typically very slow and could have time constants up to a week. As a consequence, the interactions with other control loops are negligible.

3.3 Testing Methodology

3.3.1 HIL Experimental Testing Approach

Figure 3.12 shows the experimental test rig and the HIL testing methodology. The test unit is a 3-ton (10.5 kW) split heat pump, with variable-speed drives for the compressor, supply and condenser fans. The outdoor unit is placed in an environmental chamber which is used to reproduce desired outdoor conditions (dry-bulb temperature and humidity). The environmental chamber has dimensions 18’×15’×12’ and is built with 5” thick polyurethane insulation panels. The chamber is served by a medium-temperature refrigeration system and can accommodate psychrometic testing of air-conditioning/heat pump units up to 12 ton. The indoor air-handling unit is connected to an indoor environmental test loop that is able to maintain specified indoor temperature and humidity. The test loop is made of 21”×21” square duct that has a total length of 30’ and is instrumented with high accuracy flow station and temperature/humidity sensors. A conditioning system, which is sized according to the thermal capacity of the outdoor chamber, is used to generate desired conditions in the indoor test loop. A monitoring system is in place and major operating conditions are recorded, including the instantaneous air-side cooling rate and power consumption of the compressor, supply and condenser fans.

In the HIL tests, the measured cooling effect is fed to the building thermostat model described in Section 3.3.2 and the zone temperature is predicted for the next time step (1 second). The predicted temperature is sent to the indoor loop controller which actuates the indoor conditioning system so that the return temperature closely follows the predicted indoor temperature. The indoor temperature is also used for supply fan speed control. However, due to the small variation in the simulated indoor temperature (see results in Section 3.4.6), the supply fan speed was relatively constant in the experimental tests. This bidirectional feedback mechanism ensures the indoor unit experiences realistic indoor environmental variations during PV smoothing control. The thermal HIL also plays a critical role in evaluating any impact that PV smoothing may have on indoor temperature regulation and comfort delivery. HVAC systems are primarily operated to maintain indoor comfort and any negative impact on comfort delivery will limit the technology's acceptance among building owners/operators. The measured compressor (plus condenser fan) power draw is fed to the power distribution network model presented in Section 3.3.2, which is used to simulate nodal voltage variations. Since no feedback of power system operation is involved, there is only unidirectional communications from the test unit to the distribution network model. In the experimental tests, indoor fan power was not used for PV smoothing since it was relatively constant and had magnitude much smaller than that of the outdoor unit.

The proposed control strategy was programmed in a National Instruments CompactRIO controller using LabVIEW. The generated control command, i.e., the compressor speed, is communicated to the test unit via a proprietary communication protocol acquired from the

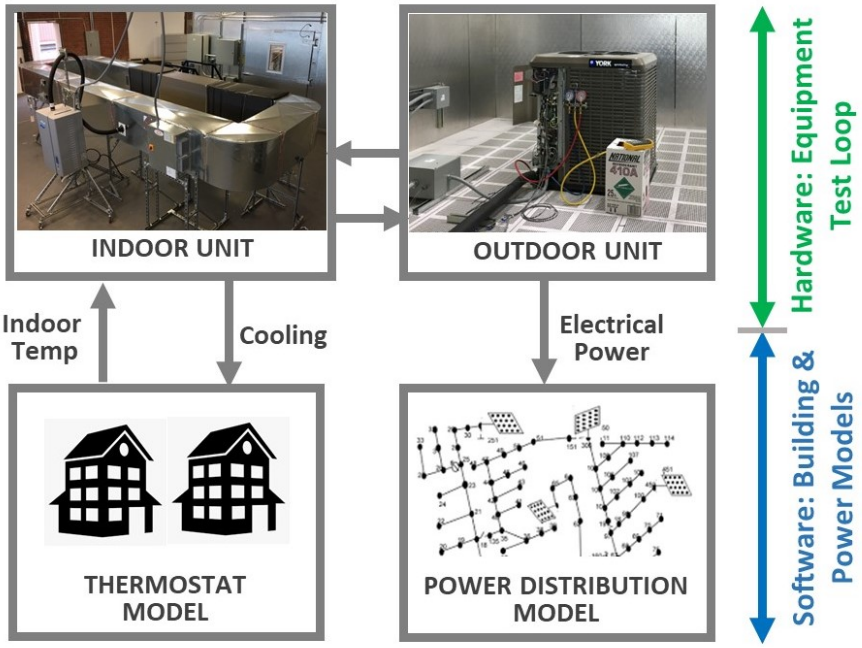

Figure 3.12: Experimental test schematic.

manufacturer. The control signal is sent to the unit and feedback information, such as actual compressor and condenser fan speeds, is received by the NI controller every second.

3.3.2 Building Load Model

We will use the power flow model described in Section 3.1 to evaluate the efficacy of our PV smoothing control method. The distribution network model is implemented using MATPOWER in MATLAB [84] and values of model parameters can be found in [85]. To simplify the overall analysis, commercial load characteristics are assumed for all the buses. Figure 3.13 shows an example load profile for a peak summer day of a small office building located in Oklahoma City. The non-HVAC appliances together contribute approximately 47% of the total building peak load for this specific load profile. Therefore, it is assumed in the PV smoothing analysis that only 53% of the nodal peak power is consumed by HVAC equipment and used as the main flexible resource. The power consumed by the test unit during the experimental tests is scaled to the nominal power capacities of the various buses in a synchronized manner. This allows assessment of the effectiveness when the smoothing solution is adopted by all buildings connected to the distribution network. The same (nominal) power factor is applied for HVAC and non-HVAC loads.

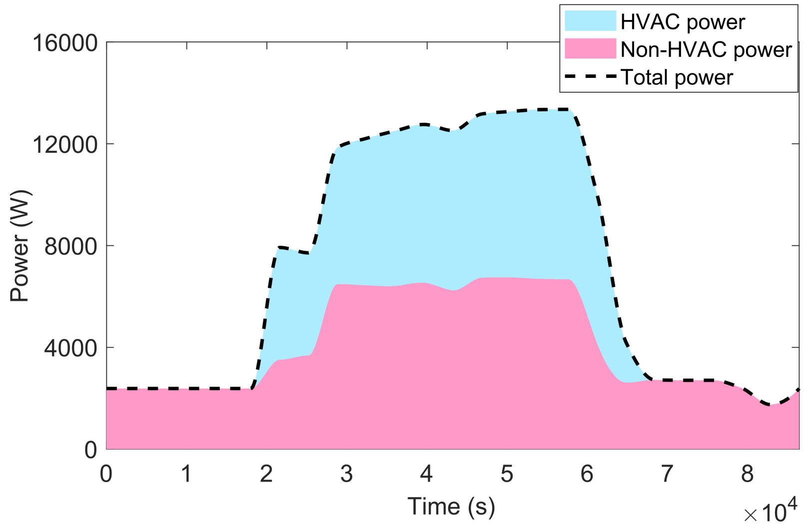

Figure 3.13: Diurnal electrical demand of a typical commercial building.

a. Building Thermal Model

Assuming time-invariant thermal parameters, a discrete-time model can be obtained to calculate the zone temperature response for given cooling effect delivered to the indoor space [30]

$$C_{bld}\frac{T_z(t)}{dt} = UA\big(T_o(t) - T_z(t)\big) + Q_{int}(t) - Q(t) \tag{3.13}$$

where C_{bld} is the effective thermal capacitance of a building, UA is the overall conductance between indoor and outdoor spaces, Q_{int} is the internal heat gain and Q is the instantaneous cooling delivered by the HVAC system. The building thermal capacitance can be estimated based on a cyclic thermostat model Section 3.1.4. The parameters assume $N_{max} = 3$ cycles/hr and $T_{db} = 0.56$°C, based on results reported in a field study by Henderson and Rengarajan [86]. The building thermal capacitance is derived from field measurements in a dozen of residential houses that were served by single-speed HVAC systems. However, it captures typical building thermal inertia and can be used to analyze representative indoor environmental responses for any type of HVAC equipment. The building overall thermal conductance UA is estimated as

$$UA = \frac{Q_{rate}}{f_{os}} \frac{1}{T_{OD} - T_{bal,D}}$$

where f_{os} is the HVAC equipment oversizing factor (assuming a value of 1.2 in this study), T_{OD} is the design outdoor temperature (set to 35°C) and $T_{bal,D}$ is the balance point outdoor temperature (19.4°C) (see [87] for modeling details).

3.4 Results and Discussions

A number of parametric tests were undertaken to understand the sensitivity of control performance under different operation settings. The parameters and the tested values are shown in Table 3.1. The tests covered two voltage regulator deadbands, three compressor speed ramp rate limits, two PV penetration levels and three building load ratios.

Table 3.1: Test parameter values

	Test cases
SVR deadband (p.u.)	0.00625, 0.016
Compressor ramp limit (RPM/s)	120, 240, 360
PV penetration	50%, 100%
Cooling load ratio	60%, 70%, 80%

3.4.1 Power Tracking Performance

There is an upper limit for the motor speed ramp rate imposed to protect the motor from overstress. This limit determines how fast a compressor can respond to a speed command

and thus can directly impact the power tracking performance. A higher ramp rate limit can enable faster speed and power responses but may overstress the motor and lead to premature failures. The VFD for the test unit has a reconfigurable parameter for the maximum ramp rate, which is defaulted at 120 RPM/s and has the highest allowable value of 360 RPM/s. The authors confirmed with the compressor manufacturer that the products passed reliability tests for different ramp rates in the range without noticeable impact on the compressor lifespan. Experimental tests were carried out for three ramp rate limits: 120 RPM/s, 240 RPM/s and 360 RPM/s. The test results are shown in Figure 3.14. The target power was generated by the control strategy discussed in Section 3.2. The compressor speed command was determined by the feedback-feedforward controller elaborated in Section 3.2.3 and sent to the compressor VFD control board. The same control settings were used in the three tests with the only difference being the VFD ramp rate limit. As expected, the ramp rate limit of 360 RPM/s resulted in the best tracking performance, while significant delays in control actions could be observed in the case with a ramp rate limit of 120 RPM/s. The results presented in the remainder of the chapter were all obtained under a ramp rate limit of 360 RPM/s.

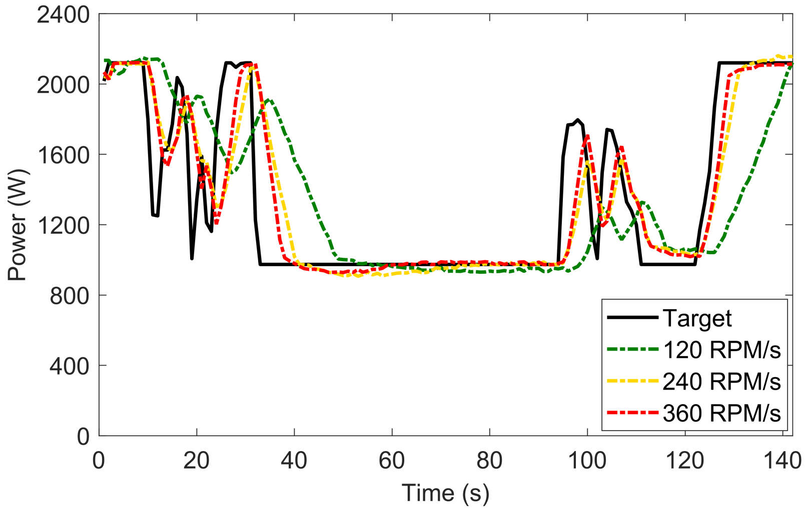

Figure 3.14: Power tracking results at different ramp rate limits.

Figure 3.15 and Figure 3.16 compare the power variations with and without PV smoothing control at node 6, for a load ratio (α_{ld}) of 70% and a PV penetration level (α_{PV}) of

50%. The outermost profile is the total building electrical demand, including both controllable (HVAC) and non-controllable power uses. In these plots, the HVAC power collected in the experiments was scaled according to the bus nominal load. The yellow shaded areas correspond to PV power generation and the net demand is highlighted by blue shaded areas. For the baseline case without PV smoothing, the building demand was relatively constant, leading to a highly fluctuating net demand because of the volatile PV power output. The PV smoothing controller varied the compressor speed in sync with the instantaneous solar power and was able to effectively reduce the variation of the net demand. A few spikes were present in the net demand, which were mainly caused by the communication delays (1 second) and limited ramp rate of the compressor speed. With PV smoothing, the standard deviation of the net demand was reduced from 0.012 MW to 0.0035 MW compared to the base case without PV smoothing.

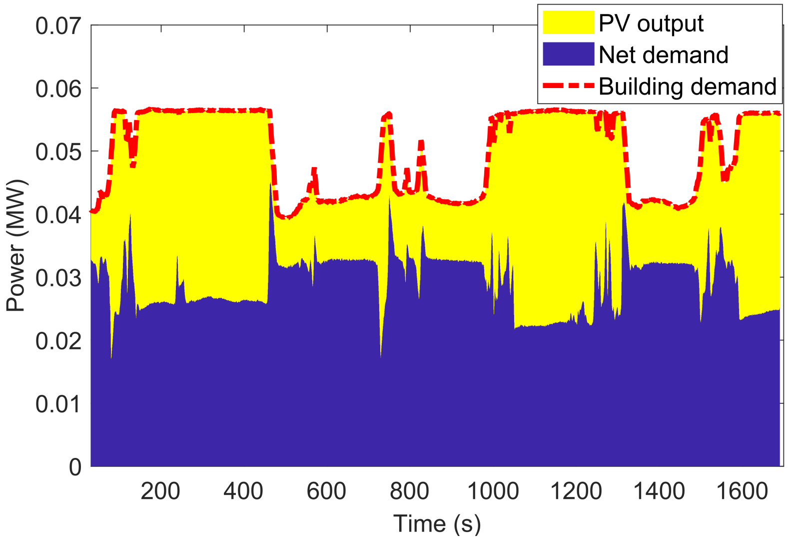

Figure 3.15: Power variations at node 6 with PV smoothing, α_{ld}=70% and α_{PV}= 50%.

3.4.2 Impact on Distribution PV smoothing

Figure 3.17 compares variations of the voltage at bus 6 with and without PV smoothing. To eliminate the influence of SVR tap operations on the nodal voltage, the SVR was temporar-

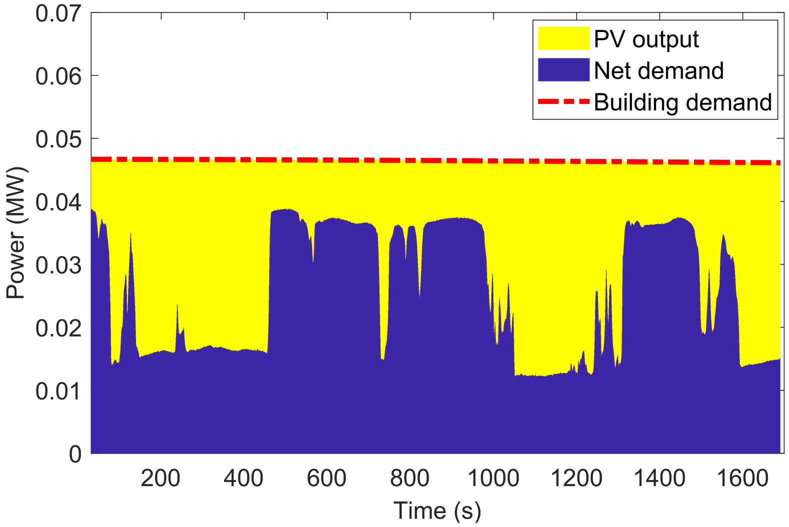

Figure 3.16: Power variations at node 6 without PV smoothing, α_{ld}=70% and α_{PV}= 50%.

ily removed for this analysis. With suppressed fluctuations in net demand, the nodal voltage variation could be much reduced using the PV smoothing strategy. Figure 3.18 shows comparative histograms of the bus 6 voltage for the two cases. Two voltage clusters existed associated with the rising and falling of the solar power. Without PV smoothing, the two clusters centered at 0.966 p.u. and 0.982 p.u., respectively. The smoothing strategy was able to shorten the distance between the two clusters, with the voltage standard deviation reduced from 0.0072 p.u. to 0.0032 p.u. Only bus 6 voltage is presented here since it has a direct impact on the voltage regulator operations, which will be discussed in the following sections. Buses further downstream of the network would see even greater voltage fluctuations driven by solar volatility.

3.4.3 Impact on SVR Operations

The SVR is operated to maintain the secondary voltage, i.e., voltage at bus 6, within a prescribed deadband. Fluctuations of the control voltage could trigger frequent SVR tap operations, which may accelerate aging of the tap changer and cause premature failures. SVR tap operation control sequences were simulated as part of the distribution network model

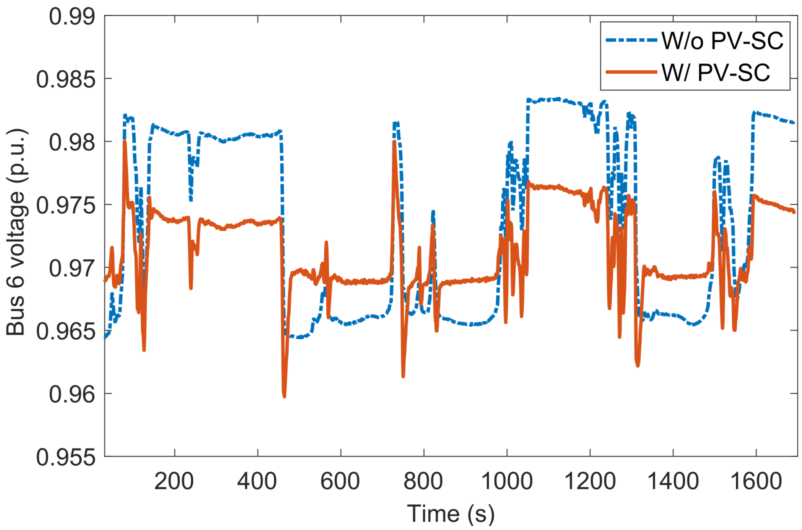

Figure 3.17: Comparison of bus 6 voltage for cases with and without PV smoothing; α_{ld}=70%, α_{PV}= 50% and no SVRs. Standard deviations(STDs) are 0.0072 p.u. and 0.0032 p.u. for cases without and with PV smoothing.

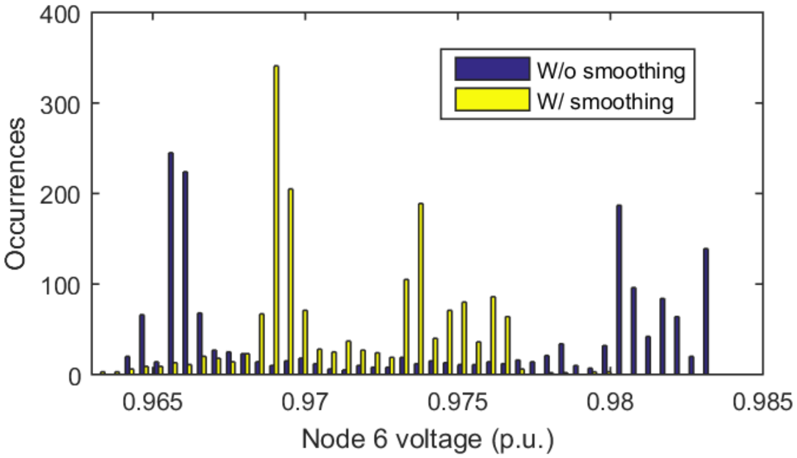

Figure 3.18: Histograms of bus 6 voltage; α_{ld}=70%, α_{PV}= 50% and no SVRs.

described in Section 3.3.2. Figure 3.19 depicts the variations of the SVR secondary voltage and Figure 3.20 shows the tap operations for cases with and without proactive PV smoothing. These simulations assumed a voltage deadband of 0.00625 p.u. It should be noted that results during the simulation initialization period are not presented. At the beginning of simulation, the tap changer stepped up from an initial position (zero) to a point where the resultant voltage fell within the deadband. It can be observed that with PV smoothing, the voltage was well maintained inside the deadband and no tap position change was executed.

A few voltage excursions were present, but they did not trigger any tap operations because the duration was all shorter than the delay setting, i.e., 30 seconds. For the base case without PV smoothing, the voltage drifted out of the deadband for prolonged periods of time, which triggered 10 tap operations in total for the 30-minute test period.

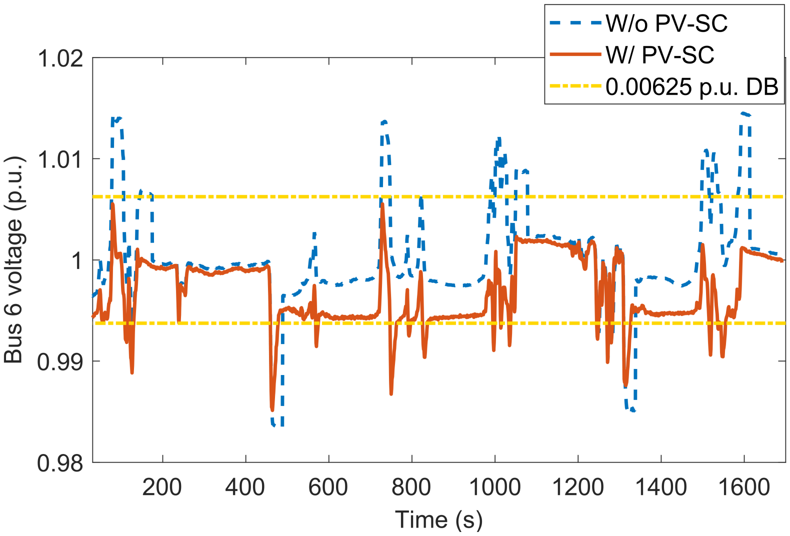

Figure 3.19: Bus 6 voltage variations for α_{ld}=70%, α_{PV}= 50% and SVR deadband=0.00625p.u. Voltage STDs are 0.0065 p.u. and 0.0052 p.u. for cases without and with PV smoothing.

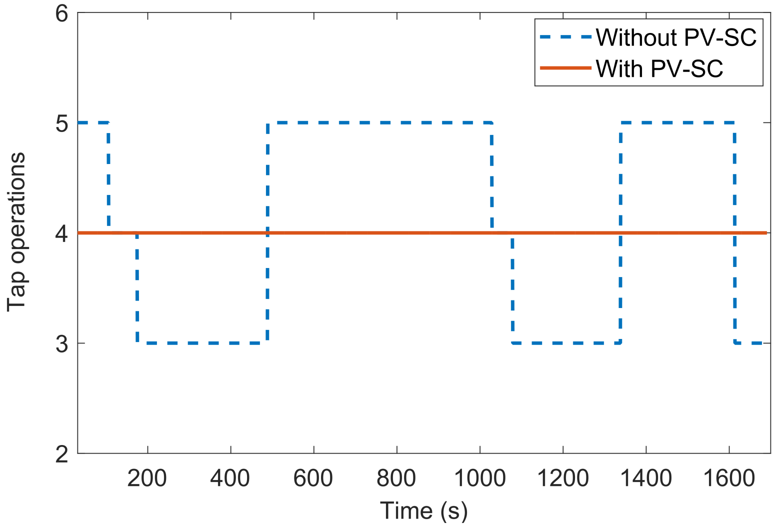

Figure 3.20: VR tap position changes for α_{ld}=70%, α_{PV}= 50% and SVR deadband=0.00625p.u.

The SVR tap operations are highly dependent on the deadband setting. A tighter deadband can provide better regulation, especially for downstream buses far away from the SVR, but may lead to frequent tap operations; a wider deadband reduces the frequency of tap changes but could result in nodal voltage floating out of acceptable ranges. Figure 3.21 and Figure 3.22 compare the voltage variations at bus 6 and the SVR tap operations for deadbands of 0.00625 p.u. and 0.016 p.u., both without PV smoothing. With a relaxed deadband setting of 0.016 p.u., the SVR secondary voltage stayed within the deadband even without proactive PV smoothing, resulting in no tap operations during the test period. Therefore, PV smoothing would not make any difference in terms of SVR operations for this specific case with a 50% PV penetration; however, the benefit of voltage improvement still existed. For cases with high PV penetrations, the SVR control behaviors could be altered significantly and this will be discussed in Section 3.4.4. Reduced tap operations with a relaxed deadband setting may come at a cost of deteriorated PV smoothing performance. Figure 3.23 compares the bus 33 (farthest node on the network) voltage variations for the two deadband settings. It can be seen that the voltage fluctuation at bus 33 has a magnitude almost twice of the fluctuation at bus 6. Thus, using a larger deadband may lead to voltage violations of regulatory limits (e.g., the ±5% threshold set forth by ANSI C84.1 [79]), especially for long radial networks with high PV penetrations. However, PV smoothing could ensure consistent PV smoothing performance along the feeder even with relaxed SVR deadband settings. Figure 3.23 shows that when the 0.016 p.u. deadband was used in combination with PV smoothing, the voltage variation was even smaller than the results obtained with a 0.00625 p.u. deadband setting (without PV smoothing).

3.4.4 Impact of PV Penetrations on PV smoothing

PV penetration levels directly affect the magnitude of voltage fluctuations on the distribution network. It was shown in the preceding section that a 50% penetration level would not cause any SVR tap changes when a 0.016 p.u. deadband setting was used, even without

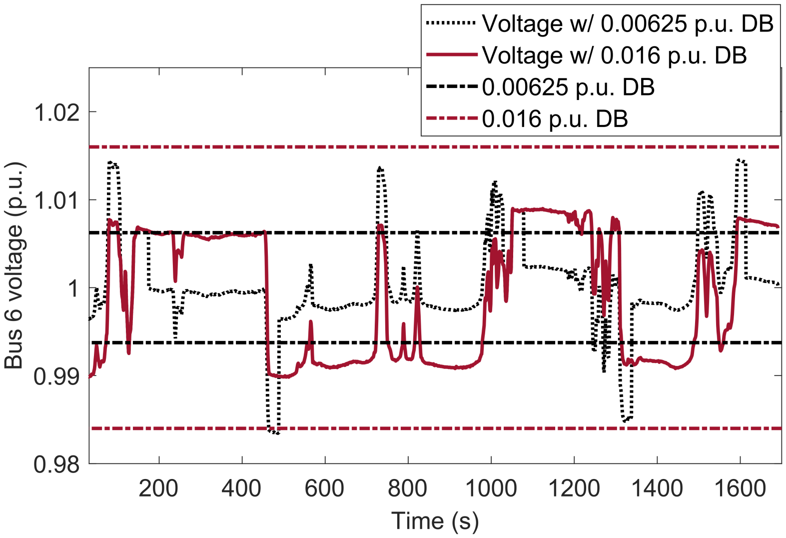

Figure 3.21: Bus 6 voltage variations under two deadband settings; α_{ld}=70%, α_{PV}= 50% and without PV smoothing. Voltage STDs are 0.0065 p.u. and 0.0082 p.u. for SVR deadbands of 0.00625 p.u. and 0.016 p.u.

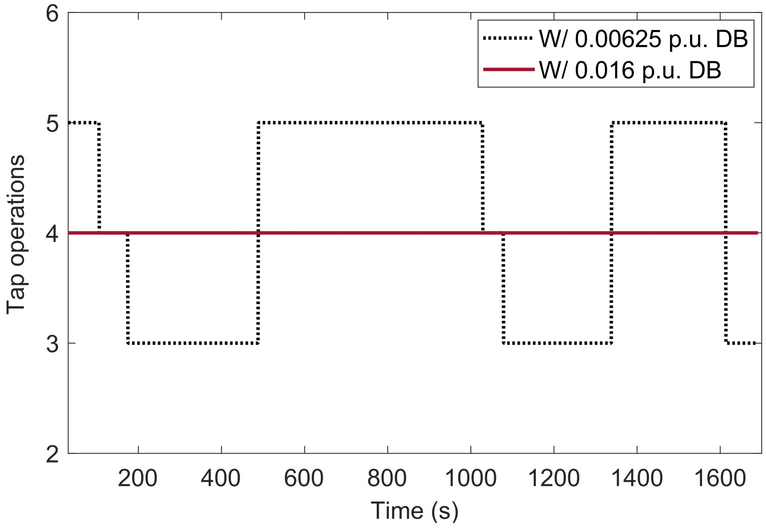

Figure 3.22: VR tap position changes under two deadband settings; α_{ld}=70%, α_{PV}= 50% and without PV smoothing.

PV smoothing. Simulations were also carried out for a case with 100% PV penetration to evaluate the influence of PV penetration levels on PV smoothing performance. Figure 3.24 compares the SVR secondary voltage variations for 50% and 100% penetrations, assuming a voltage deadband of 0.016 p.u. It can be seen that without PV smoothing, doubling the PV size resulted in the secondary voltage drifting outside the deadband and a few tap changes

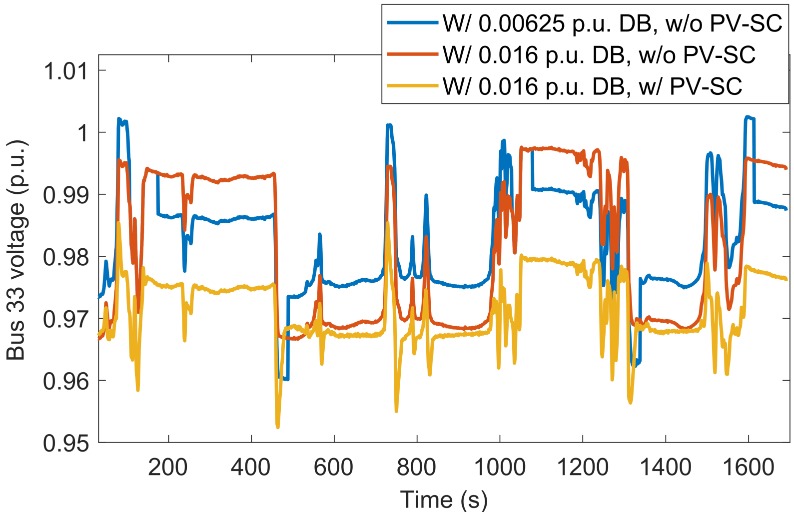

Figure 3.23: Bus 33 voltage variations under two deadband settings; α_{ld}=70%, α_{PV}= 50%. Voltage STDs are 0.0094 p.u., 0.012 p.u. and 0.0064 p.u. for blue, red and orange curves.

were undertaken to bring the voltage back into range. Figure 3.24 also shows the SVR secondary voltage behaviors when PV smoothing was enabled. The PV smoothing solution was able to maintain the voltage within the deadband without any need for tap operations, as can be seen in Figure 3.25.

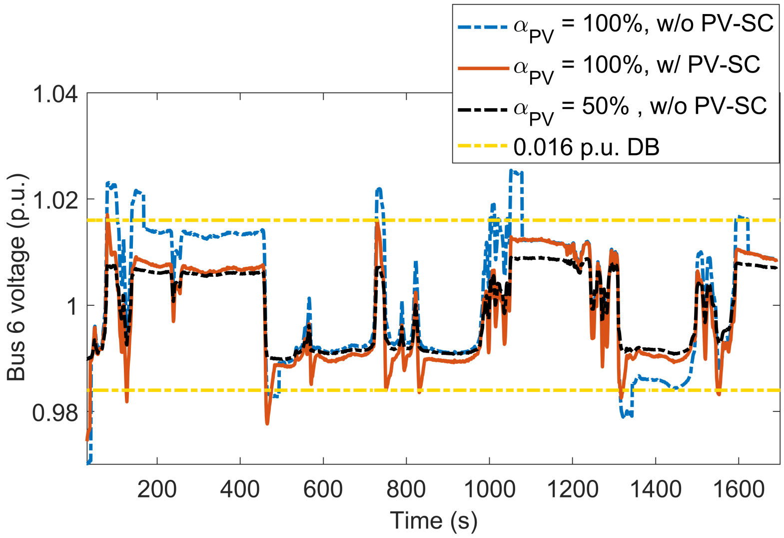

Figure 3.24: Bus 6 voltage variations with and without PV smoothing, at different PV penetration levels and with α_{ld}=70%. Voltage STDs are 0.012 p.u., 0.0098 p.u. and 0.0082 p.u. for blue, red and black curves.

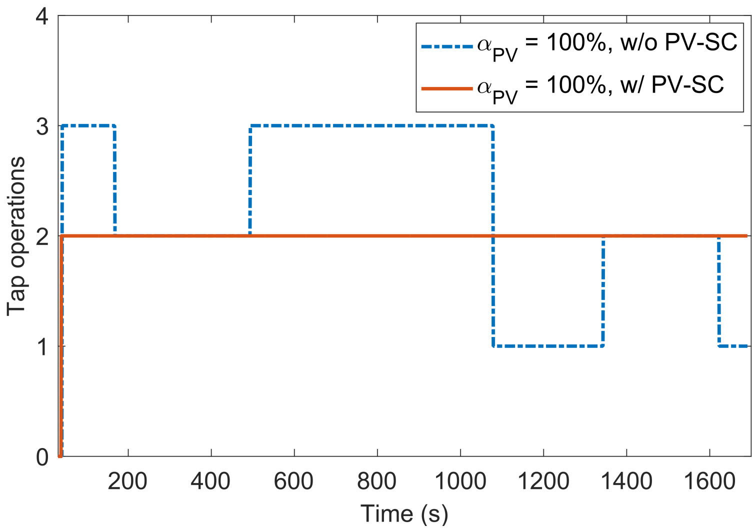

Figure 3.25: Tap operations with and without PV smoothing; α_{ld}=70%, α_{PV}= 100% and SVR deadband = 0.016p.u.

3.4.5 Impact of Building Load on PV smoothing

As illustrated in Figure 3.10, the smoothing capacity varies significantly with the instantaneous building load. For excessively high or low load conditions, the available smoothing capacity is limited due to reduced margins to the speed upper/lower bounds (see Section 3.2.2 for detailed explanations). Experimental tests were conducted for three load levels, i.e., $\alpha_{ld} = 60\%$, 70% and 80%, and the resultant net demand profiles at bus 6 are depicted in Figure 3.26. It can be observed that the smoothing capacities were similar for load ratios of 60% and 70%. At 80% load ratio, the smoothing capacity was much reduced, leading to a greater magnitude of fluctuation in the net demand. As a consequence, the voltage drifted out of the deadband, even after PV smoothing, for a few occasions which triggered tap position changes, as can be seen in Figure 3.27 and Figure 3.28. With load ratios of 60% and 70%, the PV smoothing was able to maintain the voltage in range without any tap operations.

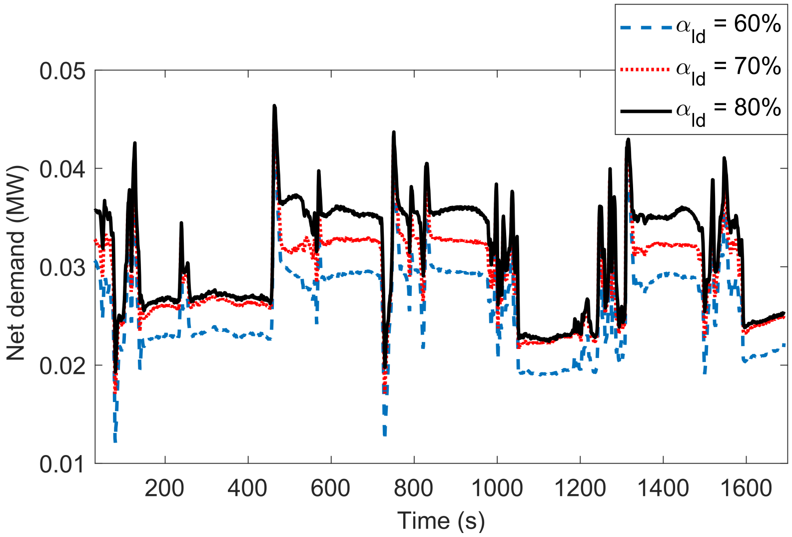

Figure 3.26: Net demand of bus 6 at different load conditions, with PV smoothing, $\alpha_{PV} = 50\%$ and SVR deadband = 0.00625p.u.

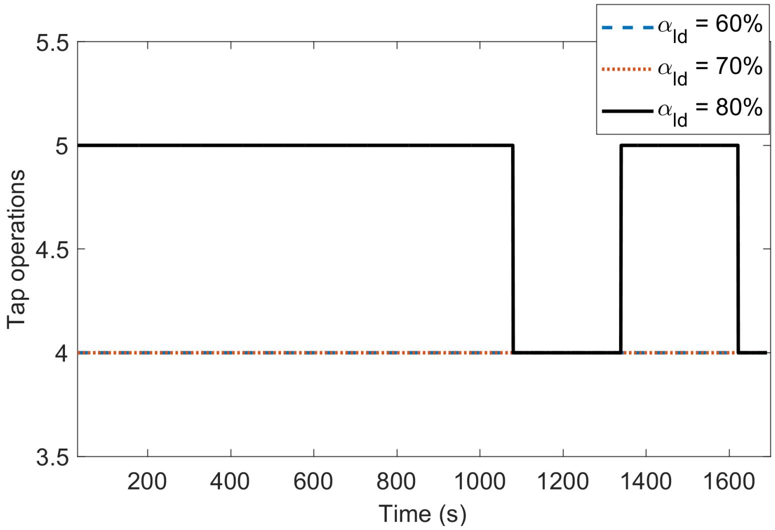

Figure 3.27: VR tap operations at different load conditions, with PV smoothing, $\alpha_{PV} = 50\%$ and SVR deadband = 0.00625p.u.

3.4.6 Comfort Impact from Thermal HIL Tests

Thermal HIL test results are presented in this section to analyze the potential impact of PV smoothing on indoor temperature regulation. The (air-side) cooling rate delivered by the AC unit was measured in real time and fed to the lumped load model described in Section 3.3.2. The zone temperature was simulated and used as return air temperature setpoint for the in-

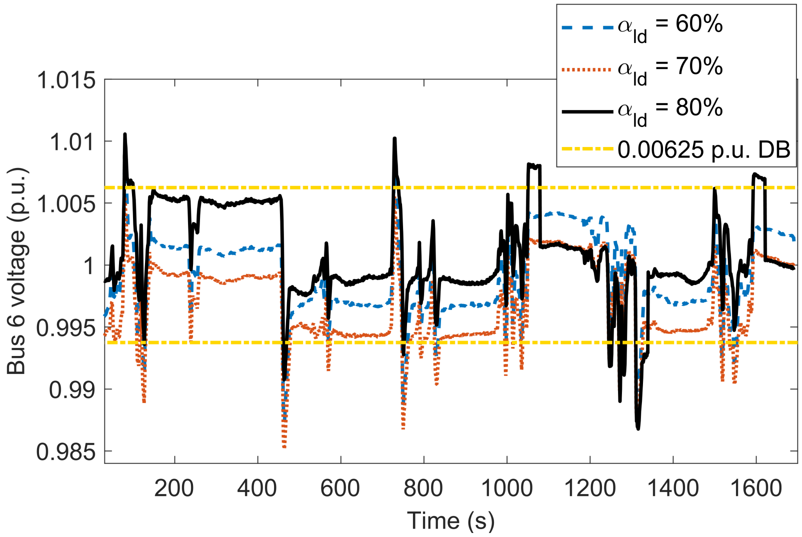

Figure 3.28: Bus 6 voltage at different load conditions, with PV smoothing, $\alpha_{PV} = 50\%$ and SVR deadband = 0.00625p.u. Voltage STDs are 0.0058 p.u., 0.0052 p.u. and 0.0051 p.u. for load ratios of 80%, 70% and 60%.

door control loop. Figure 3.29 depicts the cooling rate variation and compressor power for a test with a load ratio of 70% and compressor ramp rate limit of 360 RPM/s. Driven by the compressor speed modulation, the cooling rate moved up and down around the load line. The cooling rate had damped fluctuations relative to the compressor power, which was attributed to the thermal inertia associated with the fin-tube evaporator and condenser coils in the heat pump. Figure 3.30 shows the resultant indoor temperature variation. The temperature deviation from the setpoint (25°C) was within 0.2°C, due to a combined thermal buffering effect of the building construction and HVAC equipment. This proves that PV smoothing has negligible impact on indoor comfort, even at the maximum smoothing capacity.

3.4.7 Discussions

Distribution voltage variations and SVR tap operations are highly dependent on the load pattern, compressor speed ramp limit, PV penetration levels and SVR deadband settings. The thermal load determines the smoothing capacity while the compressor speed limit influences the power tracking accuracy. PV penetration and SVR dead band only affect distribution

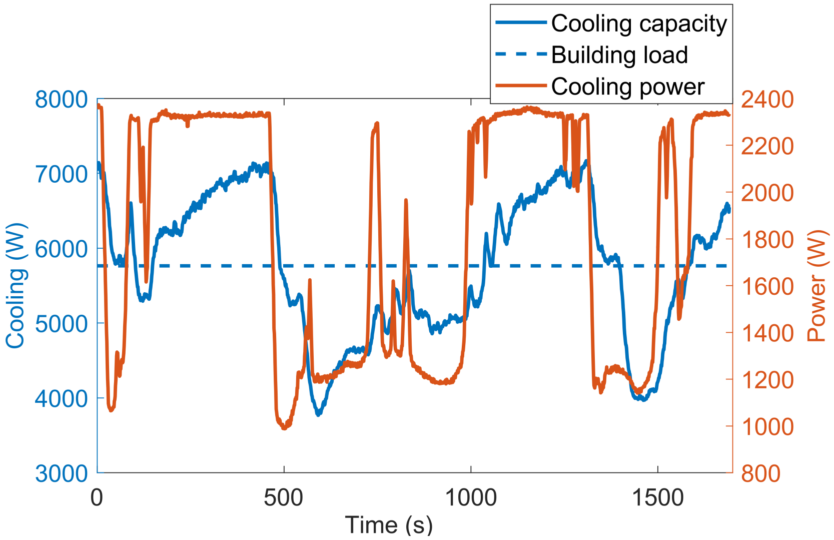

Figure 3.29: Variations of cooling capacity and compressor power for a test with α_{ld}=70% and compressor ramp rate limit of 360 RPM/s.

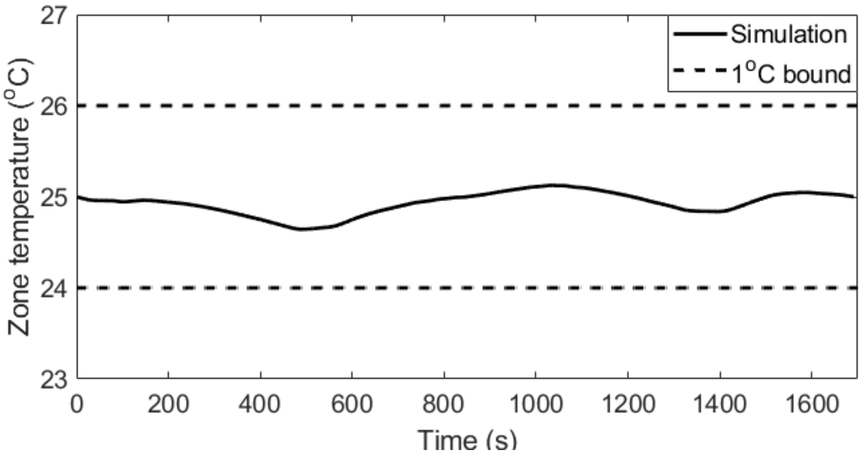

Figure 3.30: Indoor air temperature

Table 3.2: Tap operations for different test scenarios.

			Num. of tap operations	
			No PV-SC	W/ PV-SC
0.00625 DB, α_{PV}=50%	α_{ld}=60%		8	0
	α_{ld}=70%		7	0
	α_{ld}=80%		6	3
α_{ld}=70%	α_{PV}=50%	0.00625 DB	7	0
		0.016 DB	0	0
	α_{PV}=100%	0.00625 DB	9	6
		0.016 DB	5	0

voltage variations, which are related to benefits that PV smoothing can generate; but they have no direct effect on PV smoothing performance. The impact of PV smoothing on distribution voltage stability varies significantly. Table 3.2 summarizes the tap operations during the 30-minute test period for all test scenarios. With much mitigated voltage fluctuations, the PV smoothing strategy was able to reduce or even fully eliminate tap operations for all cases. For extreme load conditions and for cases with high PV penetrations but tight SVR deadband settings, tap position changes were present but effectively reduced with the PV smoothing control strategy. This is due to the combined effect of reduced smoothing capacity from HVAC equipment and more significant disturbance effect from volatile PV output. HVAC power flexibility was shown to vary with the building cooling load; at excessively high or low load levels, the smoothing capacity is reduced due to smaller margins to the compressor speed limits. To achieve consistent power flexibility, building load scheduling techniques, through dynamic zone temperature reset, can be leveraged to optimally shape the load profile.

The PV smoothing strategy was proved to be effective in mitigating the variations of net demand and voltage caused by solar power volatility. However, spiky tracking errors existed during sudden changes of solar power, due to the hardware limits of compressor ramp rate imposed by manufacturers. This analysis assumed the solar power generation at all buses follows exactly the same trajectory, which was extracted from power measurements in a 14 kW solar generator. For actual distribution networks with distributed solar generation, variation of the total solar power would be smoother with geometric averaging and better power tracking performance would be expected. In addition, the PV smoothing can be combined with advanced inverter control features to achieve improved PV smoothing performance. When solar power increases suddenly, curtailment control can be leveraged to reduce the upward ramping requirement of the compressor. During sharp drop of solar irradiance, reactive power can be injected to boost the nodal voltages. These control features can be implemented within either the PV inverter or the compressor VFD.

This feasibility study assumed identical control behaviors and did not consider diverse and random load patterns across the different buildings connected to a distribution network. As a result, the compressor speed limits between 40% and 100% have led to reduced power flexibility. For low load conditions, a variable-capacity HVAC system would cycle on (at minimum compressor speed of 40%) and off to meet the load and would not be able to provide any continuous smoothing capacity. However, HVAC units serving different buildings can coordinate the cycling cycles to offer semi-continuous power modulation. This could recover the flexibility loss caused by the speed limits and provide greater smoothing capacities.

3.5 Chapter Summary

This chapter presented an entirely new approach to PV power injection smoothing through a novel control strategy utilizing building HVAC equipment. The variable-capacity HVAC systems control strategy employs a quasi-steady-state heat pump model derived from either manufacturer performance data or field/laboratory measurements to determine on-the-fly unit power flexibility, which is determined by the base power and upward/downward ramping margins. The instantaneous PV output is monitored and projected onto the power modulation range in determining a desired heat pump power level. Then a feedforward-feedback controller is used to vary the speed of the heat pump compressor to follow the power setpoint. Experimental tests were carried out with a hardware-in-the-loop (HIL) testbed, which integrates a 3-ton heat pump (hardware) and numerical models for a representative building and a 33-bus distribution network (software). Test results are reported including power tracking performance, distribution nodal voltage variations, voltage regulator operations and indoor comfort impact. The tests cover a range of building thermal load, PV penetration, compressor ramp rate limit and voltage regulator setting. Considering the significant electrical energy consumption by buildings worldwide, the proposed technology can leverage the vast untapped storage resources associated with building end uses, helping mitigate the adverse impact and increase the hosting capacity of renewable resources on the electric grid.

CHAPTER 4

DISTRIBUTION VOLTAGE SUPPORT THROUGH COORDINATIVE CYCLING OF HVAC SYSTEMS

Chapter 3 demonstrated the feasibility of using variable-speed heat pumps to mitigate solar power fluctuations at the second time scale. The simulation tests assumed a synchronized control of all HVAC systems connected to the same distribution feeder. However, variable-speed systems are not common, especially in the residential sector, and synchronized control is not practical to implement because of the diversities in HVAC loads and operational constraints across different households.

This chapter presents a different distribution voltage control approach using single-stage (cycling) HVAC systems that are more commonly used in residential and small commercial buildings. This control approach coordinates the duty cycles of HVAC equipment serving different households to provide maximum voltage support. A co-simulation framework, which links 100 EnergyPlus building models and a power flow model for the 33-bus distribution network, has been developed to facilitate synthesis, analysis and verification of the voltage regulation strategy for cycling HVAC systems in buildings. The flexibility and diversity of residential thermal loads and their influence on the aggregate voltage regulation capacity, can be realistically simulated with the co-simulation framework. A priority-based control logic was developed for operations of cycling HVAC systems in the households to enable active voltage support.

This chapter is structured as follows. Section 4.1 introduces the co-simulation platform along with the component models for the residential building prototypes, a power distribution grid and solar PV. Section 4.2 describes the voltage regulation strategy using building thermal loads. Section 4.3 presents the key simulation results obtained from the co-simulation platform corresponding to five voltage regulation cases. A chapter summary is given in Section 4.4.

4.1 Co-Simulation Platform

This section introduces the co-simulation platform for a PV-rich distribution grid similar to that introduced in the preceding chapter. It is assumed that solar PV panels are installed across all buses with a uniform penetration of 70%, i.e., the nameplate capacity of the PV panels connected to each bus is equal to 70% of the apparent capacity of the corresponding bus. The aggregate PV capacity is 3.19 MW. A case study for a residential community, comprised of 100 residential dwellings, is used to demonstrate the efficacy of the co-simulation platform in analyzing and evaluating the distribution voltage regulation performance under various control scenarios. It is assumed that 3 buildings are connected to each of buses #1 to #32 while 4 buildings are served by bus #33. The different simulated buildings have comparable peak electric load while the nodal power capacity can differ significantly from one bus to another. Note that an actual feeder of similar sizes may serve up to 1000 residential dwellings. The case study only considers 100 households that are scaled up to a comparable aggregate capacity. This limitation is associated with the memory requirement of EnergyPlus for each building model and the fact that all simulations in the case study are carried out on a single desktop computer. The co-simulation framework supports distributed and parallel model implementations across different computers. However, it is believed 100 buildings are adequate to capture the load diversities and trends in the aggregate power flexibility. In the case study, the building loads are scaled so that the annual peak loads of all households served by the same bus add up to 80% of the node nominal capacity.

Figure 4.1 shows the schematic diagram of the co-simulation framework along with the data flow across the various components. The co-simulation framework adopts a loose coupling strategy (ping-pong). At each time step, data is being exchanged between the different tools for the pre-defined interfacing variables: for each simulation tool, the external interfacing variable values of the previous time step are used to calculate its model output for the current time step. The interaction between simulators is orchestrated by the python master algorithm. A group of residential dwellings (e.g., 100 houses in the case study) are simulated through parallel and independent EnergyPlus models each wrapped in the form of a functional mockup unit (FMU) which includes the building model and corresponding weather file. At each time step, two main interactions take place between the master code and the different building models: (1) the master code extracts outputs, e.g., the total power consumption and current zone/domestic hot water (DHW) temperatures, from the 100 building models which are run on the same computer sequentially, although the developed framework has the capability of simulating different buildings models in parallel on multiple cores or across multiple computers, and (2) when all building simulations are completed for the current time step, the controller accepts the simulated results and determine the control commands (cycling control signals) which are then sent to the building FMUs. The building power consumption is passed along with the solar power generation from the PV model to the distribution grid model, which calculates the voltage of the feeder. A homegrown grid simulator for radial distribution networks is utilized which offers both a nonlinear power flow model and a linear surrogate model; the latter is leveraged by the central controller to support control decision making. If a SVR is present, the tap position is adjusted and the corresponding turn ratio is applied to the distribution grid model to regulate the secondary voltage within its deadband. Finally, the central controller receives the voltage output from the distribution grid model and generates an cycling command to each controllable load. The framework then progresses to the following time step, repeating the described sequence. Note that the co-simulation engine operates with a one-minute time step and the solar data used in this study also has a time resolution of one minute. Therefore, the presented results only represent benefits that can be achieved up to the minute time scale.

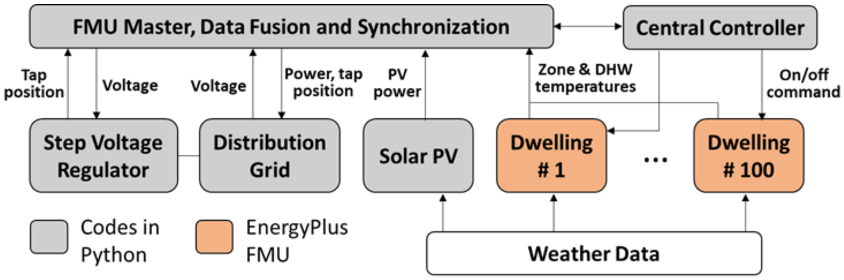

Figure 4.1: Co-simulation framework and interfacing variables

4.1.1 Building Load Model

The co-simulation framework incorporates the DOE prototypical residential building models developed by Pacific Northwest National Laboratory (PNNL) in the form of FMUs. The 100 dwellings simulated in the case study cover the 2006, 2009, 2012, 2015 and 2018 editions of the International Energy Conservation Code [88] specified for the climatic zone 2B (Tucson Arizona) to reflect the construction diversity in a representative residential community. Each EnergyPlus FMU models a two-story single-family dwelling with a total floor area of 2,376 ft2 and equipped with a central heat pump system for space cooling and heating (with a resistive auxiliary heater used in Emergency Heat mode), and a resistive water heater.

U.S. households typically employ staged HVAC and water heating equipment that cycle on and off (or between stages for multi-stage systems) to maintain the thermostat temperatures close to their setpoints. However, EnergyPlus is primarily designed to evaluate quasi-steady-state energy performance and cannot directly model cyclic operations of residential HVAC. In order to capture more realistic load responses, the control logics in EnergyPlus have been modified to receive cycling commands provided externally by the control module. Thermostat and water heater setpoints/deadbands are also implemented outside EnergyPlus in the co-simulation master code. Temperature setpoints of 23°C for the indoor spaces and

47°C for the hot water tank are assumed with a deadband of 0.5°C. Further, the thermal inertia, occupancy schedule and operational settings such as anti-cycling periods all impact the variations of flexibility and thus the ability of residential loads to provide voltage support across the different houses and at different times of the day. To better capture the aggregate load flexibility, occupancy schedules and thermostat cyclic patterns are randomized across the different household models in the co-simulation platform, to be discussed in the following subsections.

a. Building Thermal Model

EnergyPlus simulates quasi-steady-state temperature variation of the indoor air volume but cycling of a HVAC unit is dependent on the temperature reading inside a thermostat. Indoor furniture and thermostat enclosure may cause buffering effect in temperature reading and thus can affect the cycling pattern of a HVAC system. Since the combined thermal capacitance, associated with building construction and thermostat enclosures, has a significant impact on the load flexibility of a dwelling (elaborated later in this section), it is important to obtain representative capacitance estimates. A hybrid method is proposed here that combines the thermostat cyclic model and high-resolution field data collected in a dozen of U.S. houses to obtain a realistic range for the combined thermal capacitance; details of the method are presented in Section 3.1.4.

As previously mentioned, the capacitance significantly impacts the load flexibility of a dwelling, which is defined as the margin for the electrical load increase (ramp-up) or decrease (ramp-down) from the current load level. Figure 4.2 illustrates the effects of thermal capacitance and anti-cycling time on power flexibility of HVAC equipment. The red shaded area corresponds to load ramp-up flexibility. If the current time step falls within the red shaded area, the HVAC unit can be turned on if needed. Similarly, the blue shaded area presents the ramp-down flexibility during which period the HVAC equipment can be turned off anytime. A controller cannot turn a HVAC system on or off unless there is ramp-up or ramp-down flexibility. Note that load flexibility of HVAC equipment is highly dependent on the anti-cycling period, which is implemented by manufacturers to prevent frequent cycling of the compressor for the sake of equipment lifetime. After a shut-down (or start-up) of the HVAC equipment, the unit ramp-up (or ramp-down) flexibility will not be available until the anti-cycling timer expires. This is why larger anti-cycling time settings could lead to reduced load flexibility due to prolonged lock-out of a compressor, as evident from comparison of Figure 4.2 (a) and Figure 4.2 (c). In the case studies, the minimum on-time and off-time of a duty cycle both assume 4 minutes. HVAC load flexibility is also affected by the building thermal inertia. For a dwelling with high thermal mass or large thermostat inertia, the combined capacitance is high and the thermostat temperature variation would be slow, leading to greater load flexibility; on the other hand, houses with light construction typically involve low thermal capacitance and thereby smaller load flexibility. This can be clearly seen through comparison of Figure 4.2 (a) and Figure 4.2 (b). The available load flexibility of a community at any time instance is simply the sum of power flexibility across all households (see Figure 4.7 of the case study section for the aggregate flexibility). Note that EnergyPlus

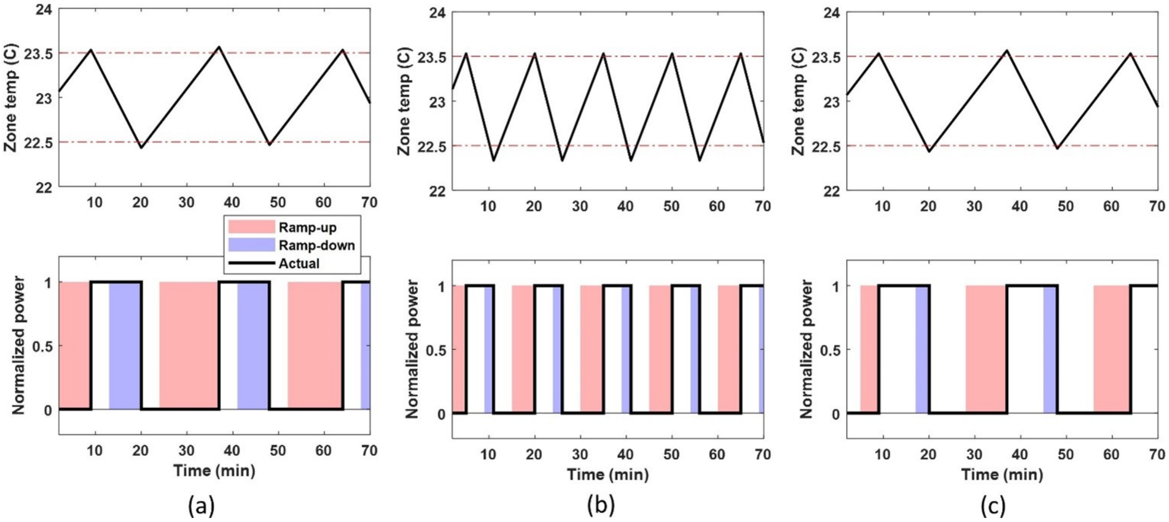

Figure 4.2: HVAC flexibilities for different simulation settings: (a) N_{max} = 2.5, anti-cycling time = 4 min; (b) N_{max} = 5, anti-cycling time = 4 min; (c) N_{max} = 2.5, anti-cycling time = 8 min.

does not offer a thermostat model directly, but the "zone temperature capacitance multiplier" parameter can be used to simulate the additional inertia associated with thermostat enclosure and indoor furniture [83]. This parameter is randomized across the different building models of the co-simulation so that the resultant peak cycling rate uniformly falls within the range identified in [83].

b. Occupancy and Electrical Load Schedules

The original prototypical building model has predefined occupancy and load schedules while these schedules are likely to differ significantly from one household to another. In order to capture the electrical load diversity, occupancy profiles in EnergPlus are randomized across different dwellings and each of the household end uses has been linked to the number of occupants for a given dwelling, e.g., 22.8 W/person for dishwasher, 35.5 W/person for refrigerator, 14.2 W/person for clothes washer, 72.5 W/person for electric dryer and 730 W/person for electric range; these end use densities are estimated based on the nominal end uses and occupancy of the original prototypical model. Occupancy schedule is randomized using the model developed by [89], based on a first order time inhomogeneous Markov chain derived from self-reported surveys. The occupancy schedules generated across the 100 buildings are depicted in Figure 4.3.

c. Weather Data

The EnergyPlus residential building simulations utilize measured meteorological (dry-bulb temperature, relative humidity, atmospheric pressure and windspeed) and solar irradiance data (global horizontal, direct normal and diffuse horizontal solar radiation), obtained from the OASIS database of National Renewable Energy Laboratory for Tucson, Arizona [90]. The data is available in a minute resolution and spans over the whole year of 2019. Note

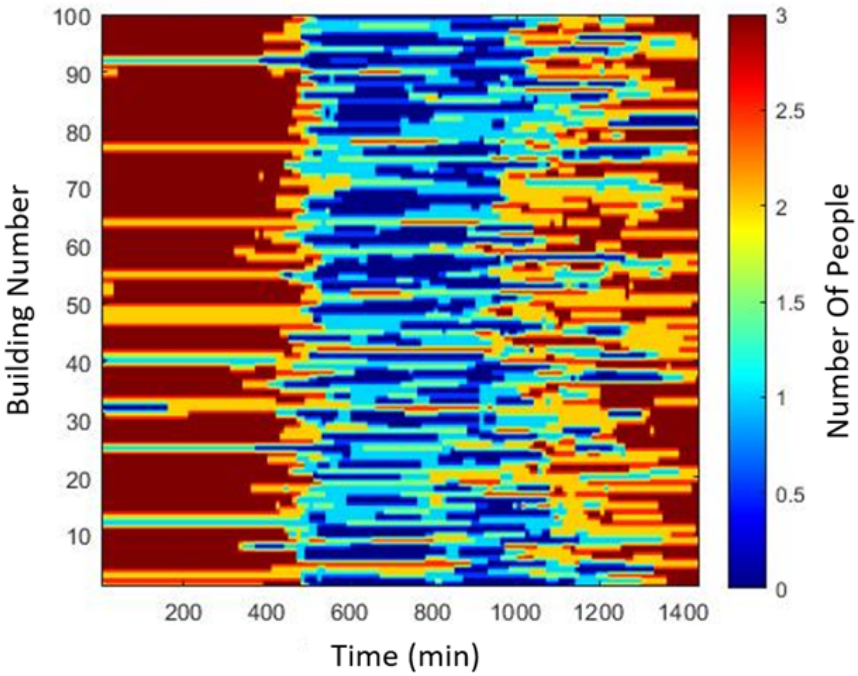

Figure 4.3: Occupancy schedules of all the simulated buildings throughout a summer day

that the temperature and solar irradiance data is also used by the solar PV model discussed in Section 4.1.2

4.1.2 Solar Photovoltaic Model

The solar irradiance fluctuations can occur at a range of frequencies from fractions of mHz to a few Hz. The daily solar irradiance parabolic profile is the source of the low frequency variation; medium frequency variation is mainly associated with moving clouds while local intermittent shading and passing flocks of birds contribute to high frequency variation of solar irradiance. [91] presented a thorough analysis of the frequency spectrum of solar PV power based on field measurements with one-second time resolution. The study found that 98% of the PV energy is attributed to the frequency band lower than 1mHz (15 mins).

In this study, the solar irradiance data from the NREL OASIS database is used which has a time resolution of one minute. A solar PV model is implemented to calculate the solar power output for the given solar irradiance and ambient temperature (the same as the weather data used in EnergyPlus building models) at each time step. The instantaneous PV power output (under maximum power point) can be estimated with

$$P_m = \eta_c A G_T \tag{4.1}$$

where A is the aperture area, G_T is the global horizontal solar irradiance and η_c is the PV power output efficiency. The PV efficiency was found to be linearly related to the cell temperature and can be estimated with the following correlation [92]

$$\eta_c = \eta_{T_{ref}}[1 - \beta_{ref}(T_c - T_{ref})] \tag{4.2}$$

where $\eta_{T_{ref}}$ is the PV power output efficiency at the standard test conditions, i.e., at the reference cell temperature $T_{ref} = 25°\text{C}$ and solar irradiance of 1000 W/m2, and β_{ref} is the temperature coefficient. This correlation assumes the impact of solar irradiance on the conversion efficiency is negligible, which is a common practice. These parameter values can be obtained from the manufacturer, e.g., $\eta_{T_{ref}} = 0.125$,$\beta_{ref} = 0.0044°\text{C}^{-1}$ for crystalline silicon modules [93]. It is difficult to reliably measure the PV cell temperature and a practical method is to use the ambient temperature T_a to estimate the cell temperature, such as [94]

$$T_c = T_a + \frac{G_T}{G_{NOCT}}(T_{NOCT} - T_a) \tag{4.3}$$

where G_{NOCT} is the nominal solar irradiance and T_{NOCT} is the nominal operating cell temperature measured under nominal terrestrial environment [95]. Note that the PV efficiency in Equation 4.1.2 has combined an inverter efficiency of 0.95, as the original parameter value for $\eta_{T_{ref}}$ is 0.13.

4.2 Voltage Regulation Strategies from Building Thermal Loads

This section describes the control strategy for building HVAC and DHW loads to enable proactive voltage regulation. The strategy always uses the HVAC regulation flexibility first and only when the HVAC flexibility is exhausted, the DHW flexibility is procured. Before the strategy is deployed, the target nodal voltage and a corresponding deadband need to be specified; the control voltage could be the nodal voltage on the secondary side of a SVR or the voltage of the worst case node across the feeder. Figure 4.4 shows the logics for procurement of HVAC and DHW load flexibility for voltage regulation. At each time step, the controllable loads are firstly separated into four groups: 1) a “lock-out” group including all the HVAC and DWH units with unexpired anti-cycling timers (thus these units cannot change operational status); 2) a “change of status” group comprised of the units that must change status, either on-to-off or off-to-on due to temperature excursions; 3) an “available to ramp-down” group including the units that are currently energized but can be turned off if needed; 4) an “available to ramp-up” group with units that are in idle mode but can be activated if needed. In addition, the units in the ramp-up and -down groups are ordered by the priority, e.g., if a HVAC unit has the thermostat temperature closer to the upper/lower bound of the deadband, it has a higher priority to be turned cycling. The voltage regulation strategy procures the regulation flexibility from the ramp-up or ramp-down group: if the control voltage tends to drop below the lower limit, the ramp-down flexibility is called for to reduce load of the feeder and boost voltage; similarly, if an overvoltage is about to occur, ramp-up resources will be leveraged; if the voltage falls within the deadband, no proactive voltage regulation is needed and thermal loads are controlled according to their original thermostat sequences. During proactive voltage control, the amount of the flexibility (number of units that need to be turned on or off) that is needed is determined with an iterative process in the simulation study. In real-world implementation, real-time voltage feedback can be leveraged for accurate flexibility procurement.

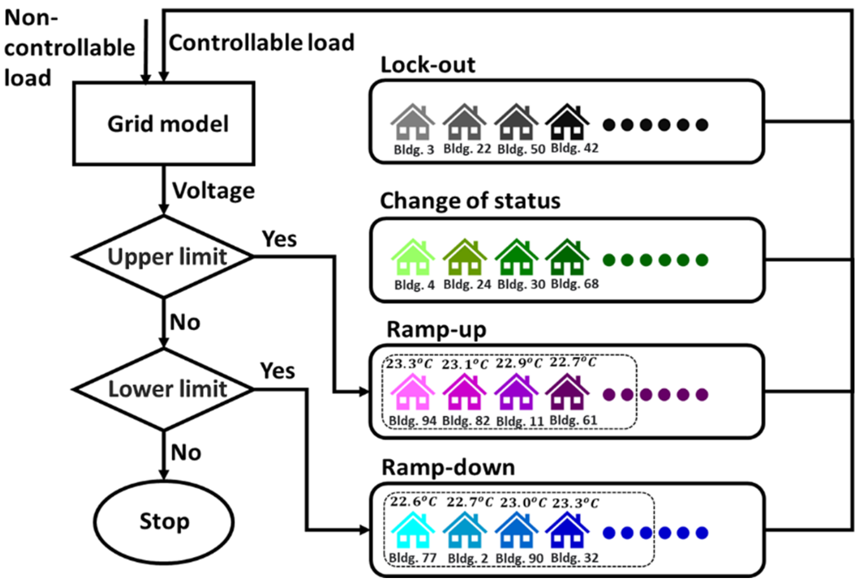

Figure 4.4: HVAC and DHW flexibility procurement logics

4.3 Simulation Case Studies

Five numerical test cases are considered to evaluate the performance improvement in voltage regulation using the proposed proactive building load control strategy. The five case studies cover distribution grids with and without SVR, different control targets (maintain feeder voltage within ANSI limits, minimize SVR operations) and different control settings (constant thermostat setpoint versus setpoint reset). The simulation parameters and settings for the five cases are shown in Table 4.1. All the simulations are carried out for the same summer day to enable cross-comparisons.

4.3.1 Baseline Control

The baseline case assumes a SVR is not in place and there is no proactive thermal load control; it is used as a benchmark to quantify the benefits of the proposed voltage regulation strategy. In the baseline case, the HVAC/DWH is controlled according to the indoor/water temperature regardless of voltage changes of the distribution grid. Figure 4.5 shows the

Table 4.1: Cases study parameter settings

	Baseline	Case 2	Case 3	Case 4	Case 5
Building voltage support	×	×	√	√	√
Setpoint for building voltage support	N/A	N/A	1.0 p.u. at bus #6	1.0 p.u. at bus #33	1.0 p.u. at bus #33
Deadband for building voltage support	N/A	N/A	0.0125 p.u.	0.05 p.u.	0.05 p.u.
SVR in place	×	√	√	×	×
SVR voltage setpoint	N/A	1.0 p.u. at bus #6	1.0 p.u. at bus #6	N/A	N/A
SVR voltage deadband	N/A	0.0125 p.u.	0.0125 p.u.	N/A	N/A
Thermostat setpoint reset	×	×	×	×	√

aggregate (active) load profile, which includes both HVAC/DWH loads and non-controllable end uses such as lighting, TV etc., along with the aggregate PV power generation, under the baseline control. The voltage variation of bus #6 is shown in Figure 4.6

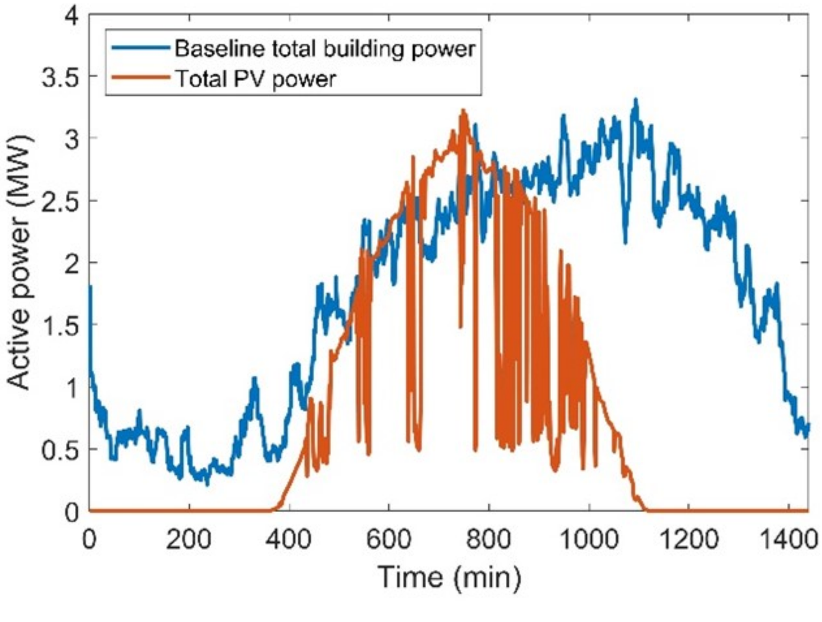

Figure 4.5: PV power output and the total building loads of the distribution grid on a typical summer day

The lowest voltage occurs at time 1103min (around 6 PM) after sunset, when there is still significant load but no solar power available. The voltage peak occurs around noon because

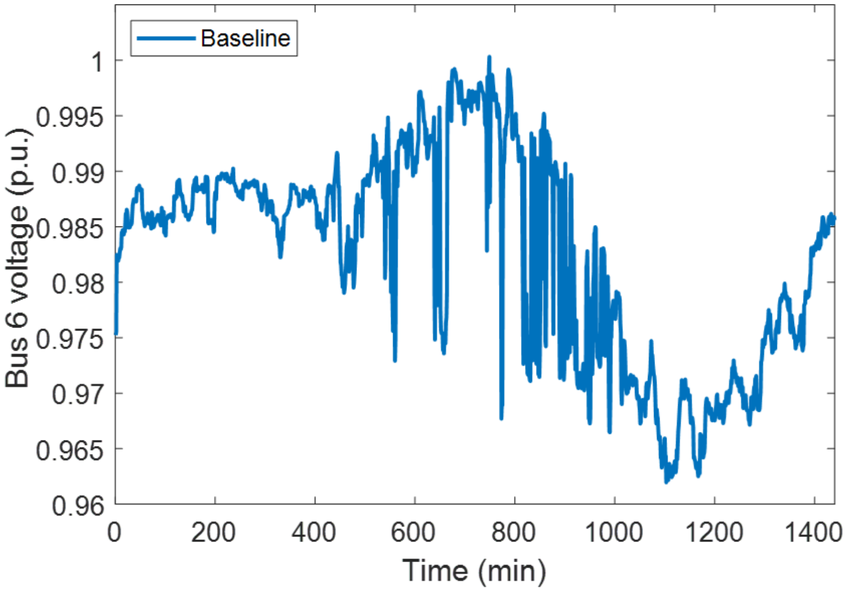

Figure 4.6: The voltage variation of bus 6 for the baseline case

of the high PV power output and relatively low building load. In addition to the diurnal voltage variation caused by the slowly changing building loads, high-frequency fluctuations of voltage are present mainly driven by the dramatic changes in the solar power due to passing clouds. This research aims to evaluate the feasibility of using flexible thermal loads to mitigate the adverse impact of PV integration on distribution voltage. Although on-site solar generation can neutralize a portion of the building loads, there is still a positive net demand and that is why the distribution voltage is almost always below 1 p.u..

Figure 4.7 shows the baseline building power usage and load flexibilities, represented by shaded areas above and underneath the power consumption curve. As described in Section 4.1.1, the red shaded areas indicate the ramp-up flexibility, which is the available power to bring on at a given time step by turning on HVAC and/or DWH units. When a change of status is applied to a HVAC unit, its flexibility becomes unavailable until the anti-cycling timer expires. Similarly, the blue shaded areas correspond to the ramp-down flexibility. It can be observed that the ramp-up flexibility of DHW is far greater than the downward flexibility. This is because the heater is sized to accommodate large instantaneous loads during active

HW usage (e.g., shower) but the average-to-peak ratio of DHW load is very low; therefore, the electrical heater is in idle mode for most of the day and can be turned on if needed, resulting in significant ramp-up flexibility. However, the water in the tank heats up very quickly after the heater is energized, due to the low average load, leading to poor sustainability of the ramp-up flexibility: the flexibility will be exausted very fast after being called upon. The available ramp-down flexibility from DHW is negligile, because DWH is off for a majority of the time. The HVAC load ratio spans over a good range from 10% to 68% for this simulated day, resulting in considerable upward and downward flexibilities. The flexibilities change sigificantly with the time of the day: during high load hours (around noon), the ramp-down flexibility is most significant and within low load hours (evening time), the upward flexibility is dominant. Since DHWs are not able to contribute sustainable load flexibility, only HVAC flexibility results will be presented throughout the rest of the chapter. Note that Figure 4.7 shows the available flexibility, which is not being utilized at all for this baseline case as active load control is not enabled. In subsequent sections, the utilized flexibility will be presented for cases when proactive voltage support is present.

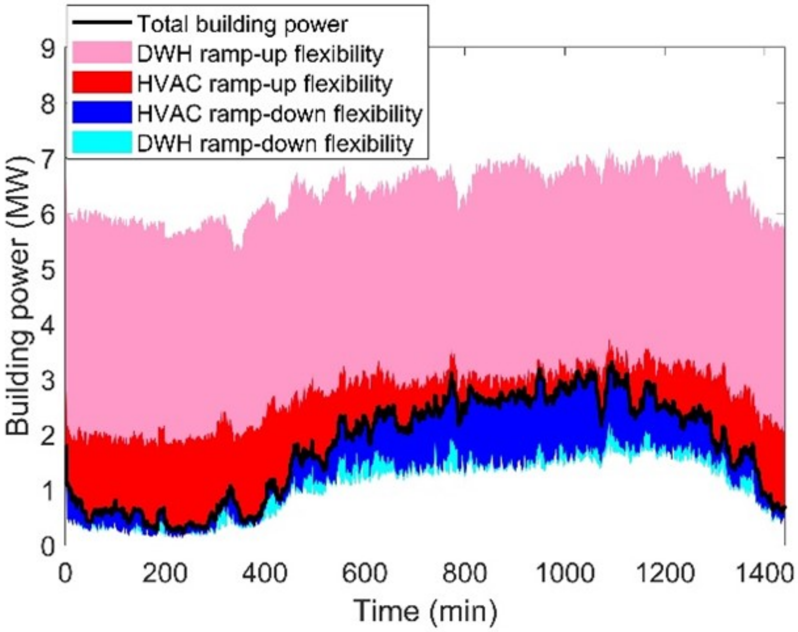

Figure 4.7: Building power consumption and load flexibilities for the baseline case

4.3.2 Case 2 (with SVR) and Case 3 (with SVR and Building Voltage Support)

When SVRs are in place, fluctuations of distribution voltage could trigger frequent SVR tap operations, which may accelerate aging of the tap changer and cause premature failures. To evaluate the potential of using flexible thermal loads to smooth distribution voltage and reduce SVR operations, simulations (Case 2 and Case 3) were carried out assuming a SVR is installed between buses #5 and #6 to maintain the bus #6 voltage within a prescribed range. The voltage setpoint for bus #6 is configured to 1.0 p.u. and the voltage deadband is set to 0.0125 p.u. If the bus #6 voltage stays within the deadband, the tap position remains unchanged; otherwise, the tap position is adjusted to vary the turn ratio of the autotransformer inside the SVR as a means to regulate the secondary voltage. Case 2 assumes no proactive regulation support from building thermal loads as a benchmark while Case 3 considers both SVR and proactive load control for voltage regulation. In Case 3, if the voltage of bus #6 tends to drift out of the deadband, the load flexibility is utilized first to pull the voltage back into the deadband and if the load flexibility is exhausted but the voltage is still out of range, the SVR then adjusts the tap position to prevent voltage excursion.

Figure 4.8 and Figure 4.9 compare the bus #6 voltage variations and SVR tap positions of Cases 2 and 3. For Case 2, the high-frequency voltage fluctuations caused by the volatile solar power lead to a total of 15 SVR tap operations within the simulated day. These SVR operations are effective in preventing voltage excursions. For Case 3, the HVAC and DHW units are proactively cycled on and off by the regulation controller as an attempt to maintain the voltage within the deadband and the load flexibility is utilized to minimize SVR operations. This can be clearly seen from Figure 4.10 which shows the available and utilized flexibilities of HVAC equipment. It can be observed that the flexibility is called upon around noon when the voltage fluctuation is significant. The proactive voltage support from HVAC can effectively reduce the number of SVR tap position changes, from 15 in Case 2 to 4 in Case 3. The four SVR tap position changes associated with Case 3 are attributed to

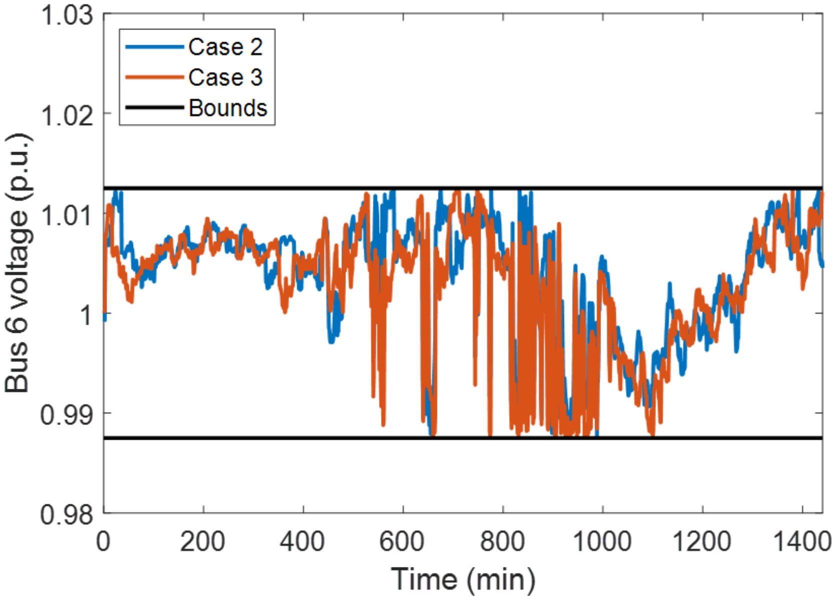

Figure 4.8: Voltage of bus 6 with and without HVAC & DHW voltage support for Cases 2 and 3

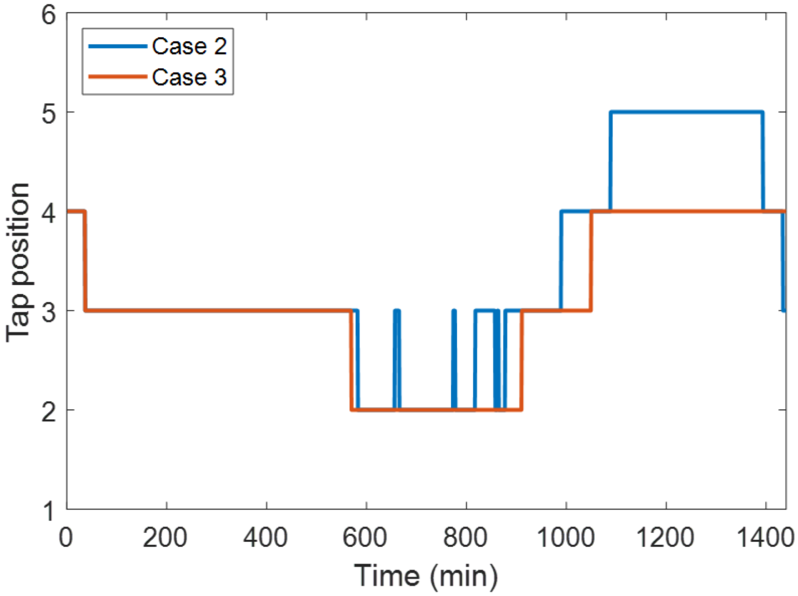

Figure 4.9: SVR tap positions with and without HVAC & DHW voltage support for Cases 2 and 3

exhausted flexibility caused by diurnal load variation (2nd, 3rd and 4th operations) and also partially due to the discrepancy between the predicted power usage and the actual power

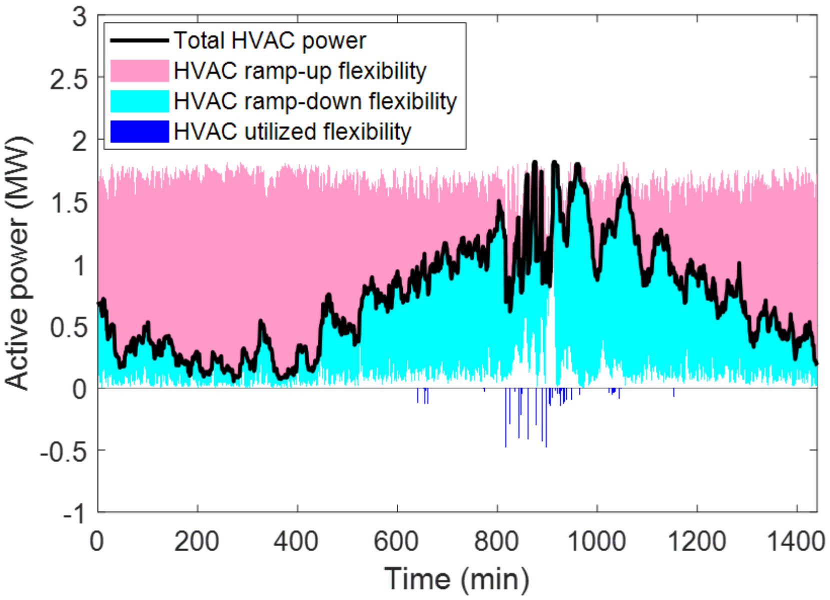

Figure 4.10: Variations of available and procured HVAC flexibility for Case 3

draw of HVAC equipment calculated in EnergyPlus (1st operation). In the HVAC regulation controller, the nominal HVAC power is used in determining the number of units to be turned on or off while the actual power draw simulated by EnergyPlus can vary significantly with ambient and indoor temperatures.

Figure 4.11 and Figure 4.12 compare the temperature variations of the 100 simulated dwellings along with the thermostat deadband, for Cases 2 and 3. It can be seen that for both cases, the indoor temperature can drift out of the deadband occasionally because of 1) the minimum time step (1 minute) implemented in EnergyPlus and 2) the anti-cycling logic for thermostats. The flexibility utilization is clearly reflected in the temperature plot of Case 3. For Case 2, the thermostat follows a conventional deadband logic where a HVAC unit is turned on or off only when the temperature reaches the upper or lower bound, while the HVAC voltage regulation controller in Case 3 tends to switch off HVAC units right after the expiration of the anti-cycling timer, even though the temperature is still far above the lower bound, during undervoltage events in order to reduce the overall electrical demand and to prevent SVR operations. The temperature excursions for Cases 2 and 3 are comparable,

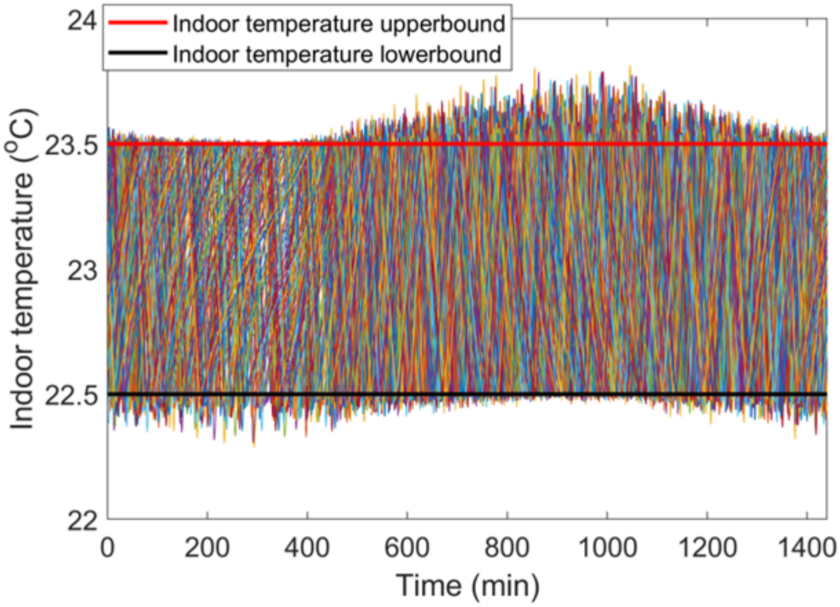

Figure 4.11: Zone temperatures of the 100 simulated buildings for Case 2

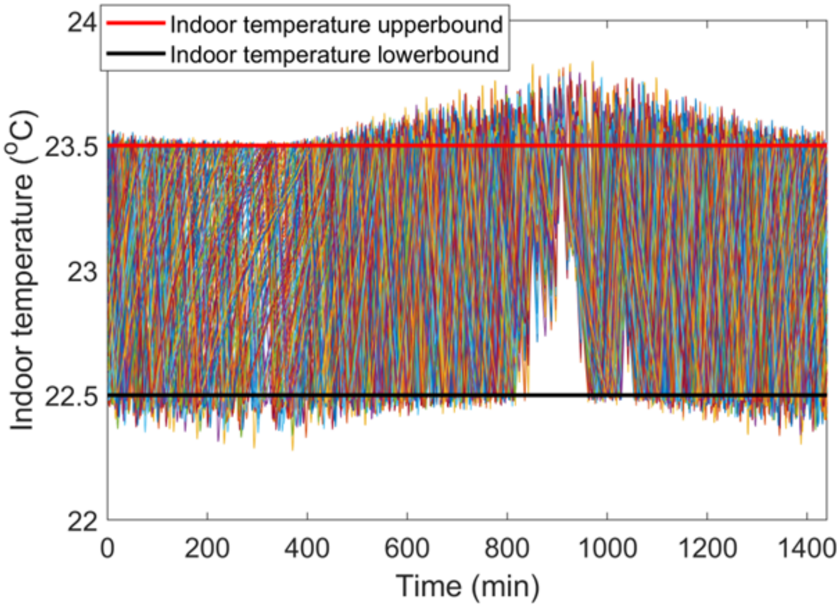

Figure 4.12: Zone temperatures of the 100 simulated buildings for Case 3

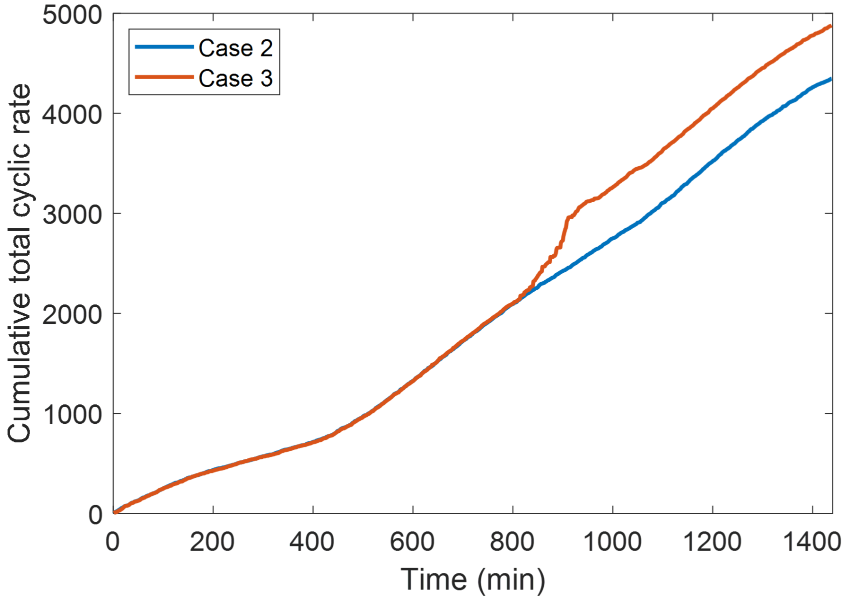

Figure 4.13: Total cumulative number of HVAC cycles for Case 2 and 3

both less than 0.3°C. This proves that the provision of flexibility has minimum comfort impact, which is consistent with results reported in previous studies [25]. To assess the potential lifetime impact, Figure 4.13 compares the cumulative number of HVAC cycles of Cases 2 and 3. Voltage regulation control results in increased cyclic operations of the HVAC equipment, from 4373 in Case 2 to 4870 in Case 3, across all 100 buildings for the simulated day. However, the increase of HVAC equipment operations (and thereby the lifetime impact) is minor compared to the benefit of SVR operation reduction.

4.3.3 Case 4 (with Building Voltage Support)

Case 4 evaluates the effectiveness of using load flexibility to maintain the whole feeder voltage within a desired range, e.g., the service voltage limit of 1.05 p.u. and 0.95 p.u for systems operating 600V and below imposed by ANSI C84.1 [96], without a SVR. The voltage of bus #33, located at the far end of the feeder, experiences the most significant variation, driven by diurnal load change and variable solar PV power injection across the feeder. Therefore, bus

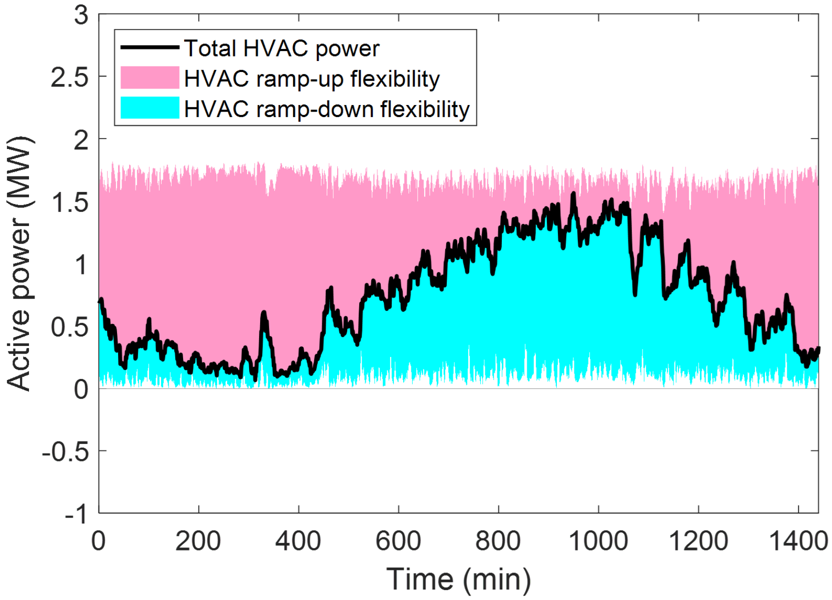

Figure 4.14: HVAC power and flexibilities for Case 1 (benchmark)

#33 voltage is the target control variable for thermal load control in Case 4. If the voltage of bus #33 exceeds the tolerable range (0.95 to 1.05 p.u.), the load flexibility controller will be triggered to turn on or off HVAC and DHW equipment to bring voltage back into range.

Figure 4.14 and Figure 4.15 depict the available and utilized HVAC power flexibility and Figure 4.16 compares the variations of bus #33 voltage between Case 1 (baseline) and Case 4. Note that without a SVR, undervoltage is present in the baseline case as the simulated results correspond to a peak summer day with aggregate load close to (75% of) the feeder nominal capacity. It can be seen from Figure 4.14 and Figure 4.15 that in late afternoon and early evening, the HVAC ramp-down flexibility is fully utilized by the voltage regulation controller as an attempt to boost the voltage of bus #33, as evident from results in Figure 4.16. However, even with full utilization of the flexibility, the voltage of bus #33 still drops below the lower bound occasionally. Compared to the baseline case, there is clear improvement on voltage performance with the proactive voltage support from HVAC and DHW: the lowest voltage has been bumped up from 0.93 p.u. in Case 1 to 0.94 p.u. in Case 4; the accumulative voltage excursion is also reduced from 1.4799 p.u.-min in Case 3 to 0.3971 p.u.-min in Case

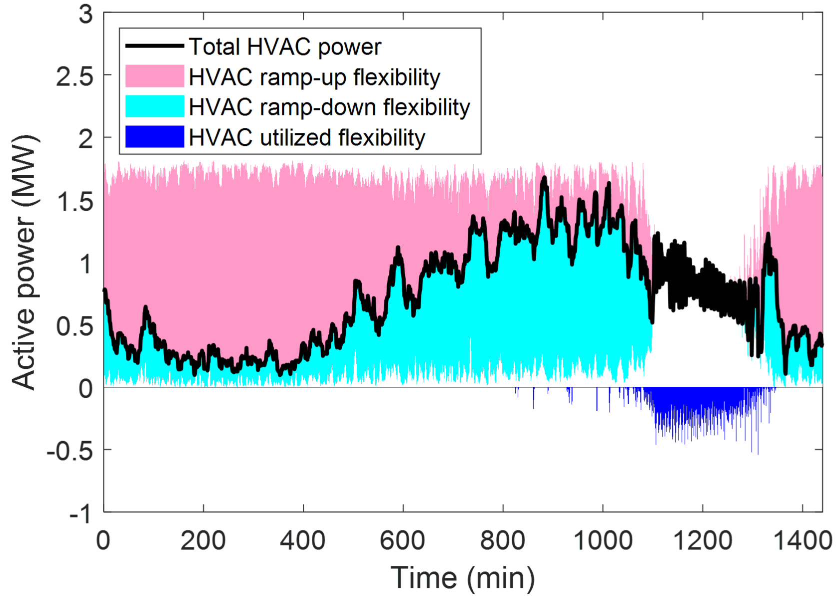

Figure 4.15: HVAC power and flexibilities for Case 4

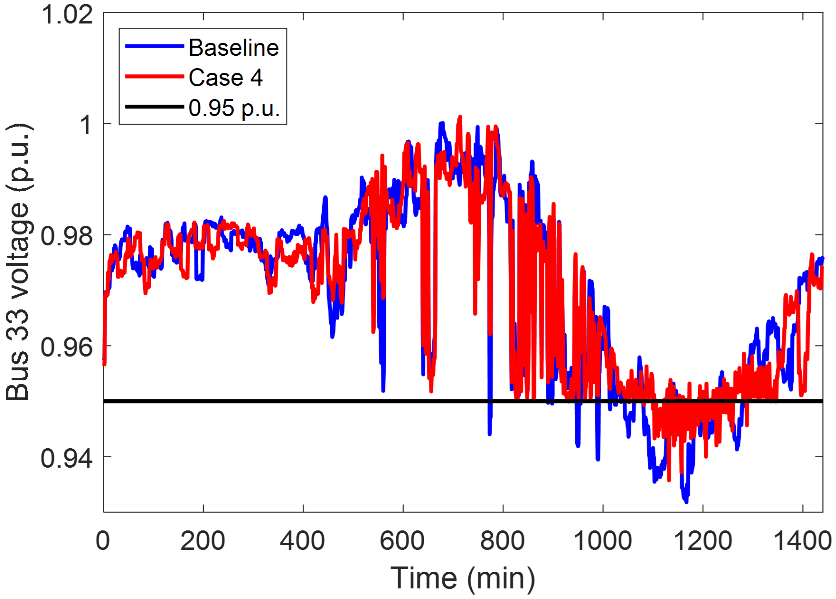

Figure 4.16: Bus #33 voltage variations of the baseline case and Case 4

4, representing a performance improvement of 73%.

4.3.4 Case 5 (with Building Voltage Support and Thermostat Setpoint Reset)

The voltage regulation controller in Case 4 fails to fully eliminate voltage excursions. In addition to the load being close to the network design capacity, the dissatisfactory control performance is also partially caused by the constant thermostat setpoint and deadband in the controller, which offers adequate flexibility to compensate for high-frequency (at minute time scale) voltage fluctuations but has limited capability in changing the overall trend of voltage variation.

It is well known that zone temperature scheduling is effective in changing a building's diurnal load profile. Therefore, in Case 5, the voltage regulation controller is modified to reset the thermostat setpoint through a droop controller: when the feeder voltage tends to drop below the lower bound, the thermostat setpoint is raised linearly with the potential voltage excursion to further reduce the load. The thermostat deadband remains unchanged in the modified regulation controller. This strategy can reduce HVAC load and thereby shift the feeder voltage upwards when the feeder voltage is close to its lower bound.

The variations of indoor temperatures of the 100 dwellings simulated for Case 5 are shown in Figure 4.17. When the feeder voltage stays within the range, the thermostat assumes the same setpoint of

Figure 18 shows the aggregate HVAC power along with the flexibilities with the proposed thermostat reset. It can be seen from Figure 4.18 and Figure 4.19 that as the indoor temperature setpoint in Case 5 is increased in the evening, the ramp-down flexibility provided by HVAC equipment can be significantly increased to offer better voltage support. Figure 4.19 compares the bus 33 voltage variation with and without indoor temperature reset. With the modified regulation controller, the accumulative voltage excursion for the simulated day can be reduced from 0.3971 p.u.-min (Case 4) to 0.0088 p.u.-min (Case 5). It should be noted that the modified voltage regulation controller may cause indoor discomfort with a temperature increase of 1.5°C from the desired level. An improvement is to optimize the setpoint trajectory throughout a day by leveraging pre-cooling actions to eliminate or reduce the comfort issues during the evening time. This will be addressed in future studies.

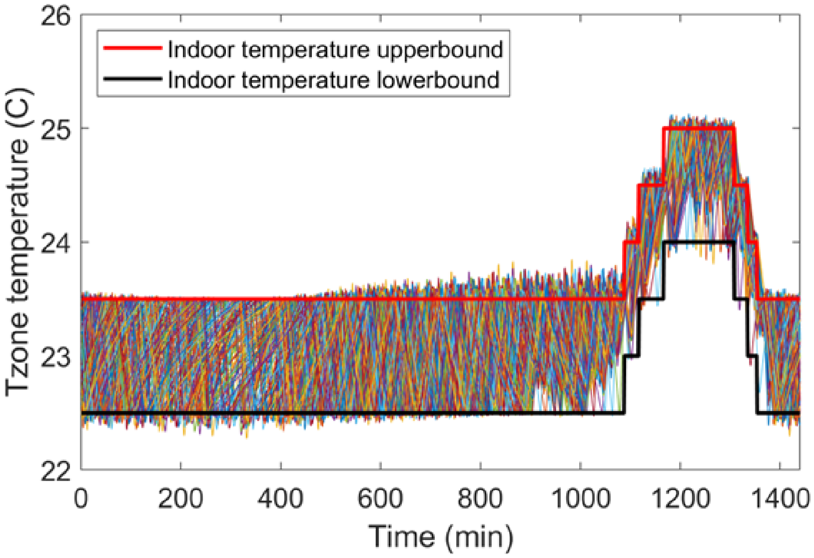

Figure 4.17: Zone temperatures of the 100 simulated buildings for Case 5

4.4 Chapter Summary

In this chapter, the use of flexible thermal loads in buildings' cycling HVAC systems to compensate for volatility of solar PV generation is proposed and its impact on distribution voltage control is investigated, with the aid of a community co-simulation platform. Five simulation cases have been considered that cover distribution grids with and without voltage regulation devices and scenarios with and without the proposed voltage regulation control strategy to evaluate the impact. Compared with Chapter 3, the analysis in this chapter is based on simulation models with one minute time step. Therefore, the presented results only reflect benefits that can be achieved at frequencies lower than 16.7mHz (1 min). The

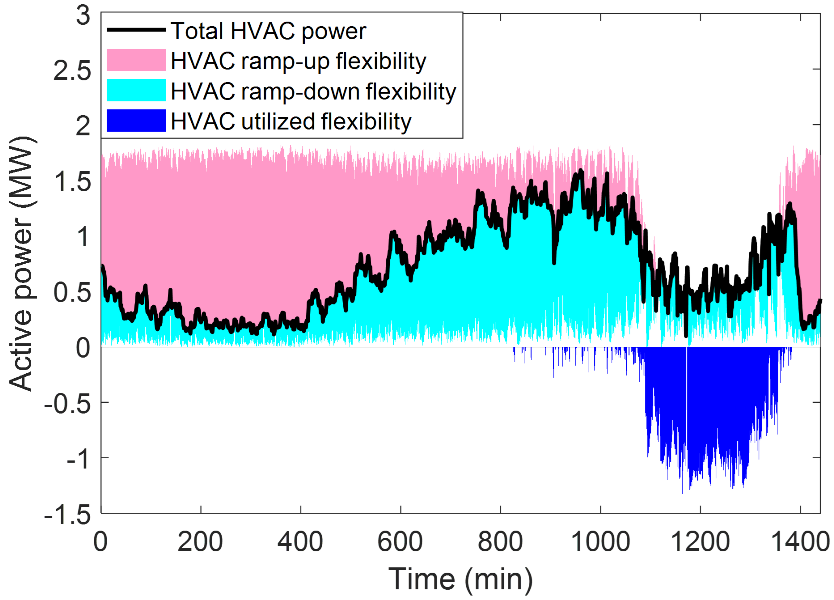

Figure 4.18: HVAC power and flexibilities for Case 5

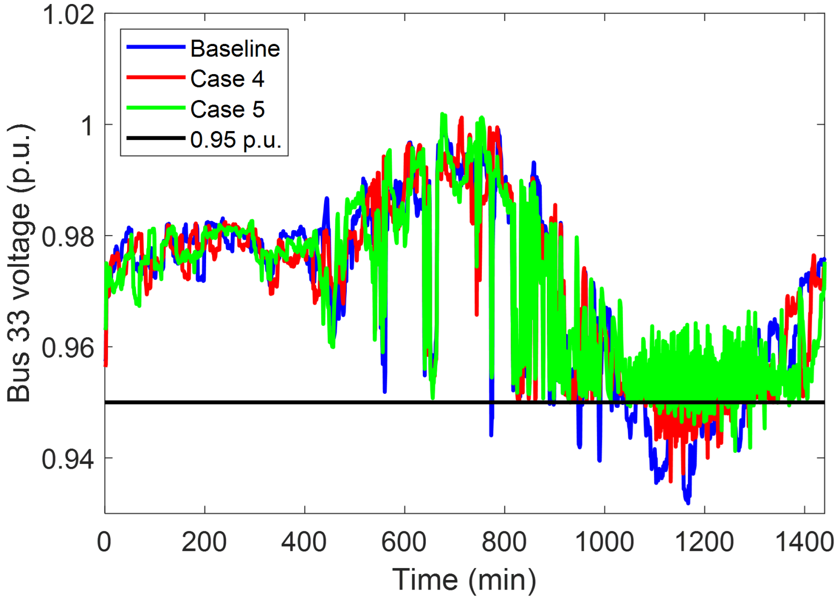

Figure 4.19: Bus #33 voltage variations of the baseline, and Cases 4 and 5

results are believed to capture a majority of the achievable performance of cycling HVAC systems given the slow response of zone temperatures and the presence of anti-cycling periods. Chapter 3 and Chapter 4 present a proof-of-concept and feasibility study of using thermal loads of residential buildings to mitigate voltage control issues caused by deeper solar photovoltaic integration. For practical implementation, the proposed control approach can be realized in a distributed manner, e.g., a reference ramping signal can be broadcast to all units and those having flexibility can respond in real-time until the ramping request is satisfied. Such event-triggered responses cannot be perfectly captured as most simulation tools use finite time steps. However, our current simulation framework can reproduce the overall trends and control behaviors. Economic factors also need to be accounted for in controller design, as voltage control actions would cause higher electricity costs for residential households and the extra costs need to be covered by distribution system operators. Unfortunately, there is no distribution markets yet in the U.S although the industry and regulatory agencies are exploring such possibilities. Next chapter will discuss fully distributed strategies and distribution market design based on game-theoretic formulations to encourage household flexibility contribution through financial incentives.

CHAPTER 5

MARKET-BASED GAME-THEORETIC CONTROL FOR PEAK DEMAND REDUCTION

Chapter 3 and Chapter 4 presented distribution voltage control strategies using building flexible loads in a dictator mode, where control actions of all buildings are determined by a central controller. Due to the heterogeneity of building load dynamics and the rising concerns for privacy, it is challenging to access operational parameters of individual buildings and make collective control decisions. Self-interestedness of the participating buildings further limits user acceptance of centralized and dictorial control strategies. This chapter introduces a novel game-theoretic control framework for building clusters to achieve near-optimal operation while respecting individual building control preferences.

This chapter focuses on a game-theoretic control strategy for building demand response aggregators whose electricity cost includes a demand charge. The demand charge is dependent on the aggregate peak demand of a control time horizon, which cannot be easily distributed among the participating buildings. Users are often reluctant to cooperate under an unfair cost allocation mechanism and may even choose to leave the alliance. To address this issue, a novel cost-sharing mechanism was developed based on the Shapley value function to ensure fair cost allocation while encouraging cooperative control actions of individual buildings. The problem is then reformulated and solved in a non-cooperative game framework to be introduced in this chapter. Coordination of buildings is achieved through a market mechanism. Section 5.1 summarizes basic theoretical foundations of VI and then show how to reformulate a non-cooperative game problem (i.e., Nash equilibrium problem (NEP)) as a VI problem. Section 5.2 introduces a non-cooperative game model for the game-theoretic control strategy, and discusses the existence and uniqueness of NE. Section 5.3 presents a VI reformulation of the NEP and provides a centralized algorithm and a distributed algorithm to find the solution. In Section 5.4, simulation tests of a six-building aggregator were carried out for the proposed strategy along with three benchmarking control methods. A chapter summary is given in Section 5.5.

5.1 Review of Convex Optimization, Variational Inequality and Non-cooperative Game Theory

5.1.1 Convex Optimization Problem

A generic convex optimization problem has the following form.

$$\underset{\mathbf{x}}{\text{minimize}} \quad W(\mathbf{x}) \tag{5.1}$$

$$\text{subject to} \quad \mathbf{x} \in \mathcal{X} \tag{5.2}$$

where $\mathcal{X} \subseteq \mathbb{R}^n$ is a convex set and W is a convex function. Assume that $\mathcal{X}$ is closed and bounded and the objective function W is continuously differentiable on $\mathcal{X}$ (i.e., its gradient ∇W exists at any point in $\mathcal{X}$). $\mathbf{x}^*$ is an optimal solution, if $\mathbf{x}^* \in \mathcal{X}$ and $W(\mathbf{x}^*) \leq W(\mathbf{x})$ for all $\mathbf{x} \in \mathcal{X}$. According to the optimality criterion for differentiable W [97], $\mathbf{x}^*$ is optimal if and only if $\mathbf{x}^* \in \mathcal{X}$ and

$$\nabla W(\mathbf{x}^*)^{\intercal}(\mathbf{x} - \mathbf{x}^*) \geq 0 \qquad \forall \mathbf{x} \in \mathcal{X} \tag{5.3}$$

5.1.2 Variational Inequality Problem

A VI problem can be written as the problem of finding a point $\mathbf{x}^*$ with the property

$$\mathbf{F}(\mathbf{x}^*)^\intercal(\mathbf{x} - \mathbf{x}^*) \geq 0 \qquad \forall \mathbf{x} \in \mathcal{X} \tag{5.4}$$

where $\mathbf{F} : \mathcal{X} \rightarrow \mathbb{R}^n$ is a nonlinear operator, and $\mathcal{X}$ is a closed and convex subset of $\mathbb{R}^n$. The above VI problem is denoted as VI($\mathcal{X}, \mathbf{F}$). Note that if the Jacobian of $\mathbf{F}$, denoted by $\mathbf{JF}$, is symmetric for all $\mathbf{x} \in \mathcal{X}$ then there exists a differential function W such that $\nabla W = \mathbf{F}$ and thus, the VI problem is equivalent to a convex optimization problem.

5.1.3 Existence and Uniqueness of the Solution of Variational Inequality

Theorem 1. ***(Existence).*** *If $\mathcal{X}$ is a closed and bounded convex set and $\mathbf{F}(\mathbf{x})$ is continuous for all $\mathbf{x} \in \mathcal{X}$, then the problem $\mathbf{VI}(\mathcal{X}, \mathbf{F})$ admits at least one solution $\mathbf{x}^*$.*

Before diving into the uniqueness of the solution of VI problem, the monotonicity properties of the vector-valued function $\mathbf{F}$ on a convex set $\mathcal{X}$ should first be defined:

Definition 1 (Monotonicity). $\mathbf{F}(\mathbf{x})$ is monotone on $\mathcal{X}$ if

$$(\mathbf{F}(\mathbf{x}) - \mathbf{F}(\mathbf{y}))^\intercal(\mathbf{x} - \mathbf{y}) \geq \mathbf{0} \qquad \forall \mathbf{x}, \mathbf{y} \in \mathcal{X} \tag{5.5}$$

Definition 2 (Strict Monotonicity). $\mathbf{F}(\mathbf{x})$ is strictly monotone on $\mathcal{X}$ if

$$(\mathbf{F}(\mathbf{x}) - \mathbf{F}(\mathbf{y}))^\intercal(\mathbf{x} - \mathbf{y}) > \mathbf{0} \qquad \forall \mathbf{x}, \mathbf{y} \in \mathcal{X} \tag{5.6}$$

Definition 3 (Strong Monotonicity). $\mathbf{F}(\mathbf{x})$ is strongly monotone on $\mathcal{X}$ if

$$(\mathbf{F}(\mathbf{x}) - \mathbf{F}(\mathbf{y}))^\intercal(\mathbf{x} - \mathbf{y}) \geq c||\mathbf{x} - \mathbf{y}||^\mathbf{2} \qquad \forall \mathbf{x}, \mathbf{y} \in \mathcal{X} \tag{5.7}$$

It may be noted that the role of monotonicity for a VI problem is similar to convexity in convex optimization analysis. More VI details can be found in [98].

Theorem 2. ***(Uniqueness).***

1. *If $\mathcal{X}$ is a closed convex set and $\mathbf{F}$ is monotone on $\mathcal{X}$, the solution set of the VI problem is closed and convex.*
2. *If $\mathcal{X}$ is a closed bounded convex set and $\mathbf{F}$ is strictly monotone on $\mathcal{X}$, the solution of the VI problem is unique.*
3. *If $\mathcal{X}$ is a closed convex set and $\mathbf{F}$ is strongly monotone on $\mathcal{X}$, the solution of the VI problem is unique.*

In practical applications, the original definitions are rarely used to determine the monotonicity properties of the vector-valued function $\mathbf{F}$; instead, the monotonicity can be established by investigating the positive-definiteness of the Jacobian matrix of $\mathbf{F}$ (i.e., $\mathbf{JF}$) through the following theorem.

Theorem 3. ***(Monotonicity condition).*** *If $\mathcal{X}$ is convex, $\mathbf{F}$ is continuously differentiable on $\mathcal{X}$ and the Jacobian matrix $\mathbf{JF}$ is positive-semidefinite (positive-definite), then $\mathbf{F}$ is monotone (strictly monotone).*

5.1.4 Review of Non-Cooperative Game Theory

Non-cooperative game theory is concerned of strategies played by partially or totally conflicting agents, in which individuals behave in a selfish way to maximize their own utilities. The NE is an equilibrium of a non-cooperative game where no players can receive a larger benefit from changing only their individual strategies. Therefore, the NE is the most fundamental concept in the non-cooperative games. In this section, the mathematical expressions of the NEP, as well as the existence and uniqueness of NE, will be discussed.

a. Definition of Nash Equilibrium

An N-player game with the player set $\mathcal{N} = \{1, ..., N\}$ is defined. The control variable of player i is denoted by $\mathbf{x}_i \in \mathcal{X}_i$, where $\mathcal{X}_i$ is the action set of player i. Let $\mathbf{x}$ denote the vector of control actions of all players $\mathbf{x} = (\mathbf{x}_1^\intercal, ..., \mathbf{x}_N^\intercal)^\intercal$. $\mathbf{x}_{-i}$ is used to indicate the collective control actions of the rivals of player i, i.e., $\mathbf{x}_{-i} = (\mathbf{x}_1^\intercal, .., \mathbf{x}_{i-1}^\intercal, \mathbf{x}_{i+1}^\intercal, ..., \mathbf{x}_N^\intercal)^\intercal$. Each player minimizes his/her cost function $w_i(\mathbf{x}_i, \mathbf{x}_{-i})$ by identifying his/her optimal control actions $\mathbf{x}_i \in \mathcal{X}_i$, i.e.,

$$\underset{\mathbf{x}_i \in \mathcal{X}_i}{\text{minimize}} \qquad w_i(\mathbf{x}_i, \mathbf{x}_{-i}) \tag{5.8}$$

Assuming $\mathcal{X}$ is the Cartesian product of $\mathcal{X}_i$ (i.e., $\mathcal{X} = \mathcal{X}_1 \times, ..., \times \mathcal{X}_N$) and the formal definition of NEP can be written as

$$w_i(\mathbf{x}_i^*, \mathbf{x}_{-i}^*) \leq w_i(\mathbf{x}_i, \mathbf{x}_{-i}^*), \quad \forall \mathbf{x}_i \in \mathcal{X}_i, \forall i \in \mathcal{N} \tag{5.9}$$

where $\mathbf{x}_i^*$ is the ith player's best response when his/her rivals play $\mathbf{x}_{-i}^*$. The strategy $(\mathbf{x}_i^*, \mathbf{x}_{-i}^*) \in \mathcal{X}$ is an NE (i.e., a solution of NEP) such that no player has an incentive to deviate from it.

b. Existence and Uniqueness of Nash Equilibrium

Theorem 4 (Existence of NE). *If* $\forall i \in \mathcal{N}$, $\mathcal{X}_i$ *is nonempty, convex and compact,* $w_i : \mathcal{X} \to \mathbb{R}$ *is continuous within* $\mathcal{X}$ *and* $\forall \mathbf{x}_{-i} \in \mathcal{X}_{-i}$, $\mathbf{x}_i \to w_i$ *is convex on* $\mathcal{X}_i$*, then there exists a Nash equilibrium.*

The proof of the existence theorem relies on a fixed point argument; [99] is referred to for the details. Before analyzing the uniqueness of NE, a connection between the NEP and the VI problem should be established and the NEP should be reformulated using a VI.

Assume that the individual's objective function $w_i(\mathbf{x}_i, \mathbf{x}_{-i})$ is continuously differentiable at any $\mathbf{x} \in \mathcal{X}$ and convex in $\mathbf{x}_i$ for every fixed $\mathbf{x}_{-i}$, and the strategy set of player i is compact and convex. According to the optimality criterion given in Equation 5.3, $\mathbf{x}_i^*$ should satisfy

$$\nabla_{\mathbf{x}_i} w_i(\mathbf{x}_i^*, \mathbf{x}_{-i}^*)^\intercal (\mathbf{x}_i - \mathbf{x}_i^*) \geq 0, \quad \forall \mathbf{x}_i \in \mathcal{X}_i \tag{5.10}$$

and this condition holds for all $i \in \mathcal{N}$. Assume $\mathbf{F}(\mathbf{x}) = (\nabla_{\mathbf{x}_i} w_i(\mathbf{x}))_{i=1}^N$, then $\mathbf{x}^*$ is an NE if and only if

$$\mathbf{F}(\mathbf{x}^*)^\intercal (\mathbf{x} - \mathbf{x}^*) \geq 0, \qquad \forall \mathbf{x} \in \mathcal{X} \tag{5.11}$$

This shows the equivalence between a NEP and a VI problem. The uniqueness of NE can be guaranteed if **JF** is positive-definite.

5.2 NEP reformulation of the peak demand reduction problem

A load aggregator is considered, consisting of N buildings, the set of which is denoted by $\mathcal{N} := \{1, ..., N\}$. The goal is to identify an appropriate internal pricing mechanism and to develop an algorithm to seek the NE for the building thermal loads over a given time horizon $\mathcal{T} := \{1, ..., T\}$. Let x_n^t denote the power consumption of building n at time slot $t \in \mathcal{T}$. $\mathbf{x}^t = \{x^t\}_{t \in \mathcal{T}} \in \mathbb{R}^T$ is defined as the aggregated power consumption over the considered time horizon, i.e., $x^t = \sum_{n \in \mathcal{N}} x_n^t$, and define $\mathbf{x}_n = \{x_n^t\}_{t \in \mathcal{T}} \in \mathbb{R}^T$ as the power profile of building n over all the time slots. The vector $\mathbf{x} = \{\mathbf{x}_n\}_{n \in \mathcal{N}} \in \mathbb{R}^{TN \times 1}$ concatenates the power use trajectories of all buildings. For building n, $\mathbf{x}_{-n} = (\mathbf{x}_1^\intercal, ..., \mathbf{x}_{n-1}^\intercal, \mathbf{x}_{n+1}^\intercal, ...\mathbf{x}_N^\intercal)^\intercal$ is used to represent the control actions of the other participants in the aggregator.

5.2.1 Electricity Cost Formulation

Assume that the aggregator purchases electricity from the wholesale energy market at an energy price of p^t (with unit of \$/kWh). In addition, an anytime demand charge rate of p_d (unit \$/kW) that penalizes the peak electricity usage of the aggregator during the considered time horizon is studied. Therefore, the total collective cost for all customers is:

$$W = \sum_{t=1}^{T} p^t \cdot x^t + p_d \cdot \max_{t \in \mathcal{T}}(x^t) \tag{5.12}$$

Building owners are often reluctant to cooperative control programs because of privacy/security concerns. The lack of interoperability across different building controller vendors represents a major barrier of technical feasibility of centralized control solutions. Therefore, a non-cooperative game setting is considered in this chapter in which an appropriate pricing mechanism is imposed and individual buildings are to minimize their own electricity costs, by taking into consideration of the aggregate demand that is in turn dependent on strategies adopted by others. Under this setting, each building tends to identify its optimal control strategy given the rivals' control actions, i.e.,

$$\min_{\mathbf{x}_n \in \mathcal{X}_n} w_n(\mathbf{x}_n, \mathbf{x}_{-n}), \forall n \in \mathcal{N} \tag{5.13}$$

where

$$w_n(\mathbf{x}_n, \mathbf{x}_{-n}) = \left(\sum_{t=1}^{T} p^t \cdot x_n^t \right) + p_d \cdot R_n, \forall n \in \mathcal{N} \tag{5.14}$$

where R_n is building n's share of the aggregator peak demand and $\mathcal{X}_n$ is the strategy set of building n. For cost-sharing games with convex cost functions, the Shapley value cost-sharing rule provides the optimal price of anarchy, followed by the price of stability [100]. Therefore, the Shapley value is used to distribute the collective demand charge among the players:

$$\begin{aligned} R_n(\mathbf{x}) &= \sum_{S_n \subseteq \mathcal{N} \setminus \{n\}} \frac{(|S_n|)!(|\mathcal{N}| - |S_n| - 1)!}{|\mathcal{N}|!} \Big(V(S_n \cup \{n\}) \\ &- V(S_n) \Big), \forall n \in \mathcal{N} \end{aligned} \tag{5.15}$$

where

$$V(S_n) = \max_{t \in \mathcal{T}} \{x^t_{S_n}\}, \quad x^t_{S_n} = \sum_{m \in S_n} x^t_m. \tag{5.16}$$

So S_n is a coalition that excludes player n and $V(S_n)$ is the characteristic function of coalition S_n, which describes the total expected sum of costs that the members of S_n can obtain by cooperation. Therefore, V estimates the collective peak demand that the coalition S_n would result in. The summand of Equation 5.15 is the marginal cost contribution of a player $n \in \mathcal{N}$ to a coalition $S_n \cup \{n\}$ that is defined as the variation of the cost function of coalition after player n leave. The share of peak demand for player n is his/her weighted average marginal contribution over all possible coalitions that he/she joins; the weight associated with each coalition only depends on its size and can be interpreted as the probability that a coalition of the particular size is formed. For an example case with 3 buildings and 2 time slots in the scheduling horizon (i.e., $N = 3$ and $T = 2$), the characteristic function V can be expressed as

$$V(S) = \begin{cases} v_0 = 0 & \text{if} \quad S = \varnothing \\ v_1 = \max(x_1^1, x_1^2) & \text{if} \quad S = \{1\} \\ v_2 = \max(x_2^1, x_2^2) & \text{if} \quad S = \{2\} \\ v_3 = \max(x_3^1, x_3^2) & \text{if} \quad S = \{3\} \\ v_4 = \max(x_1^1 + x_2^1, x_1^2 + x_2^2) & \text{if} \quad S = \{1,2\} \\ v_5 = \max(x_1^1 + x_3^1, x_1^2 + x_3^2) & \text{if} \quad S = \{1,3\} \\ v_6 = \max(x_2^1 + x_3^1, x_2^2 + x_3^2) & \text{if} \quad S = \{2,3\} \\ v_7 = \max(x_1^1 + x_2^1 + x_3^1, x_1^2 + x_2^2 + x_3^2) & \text{if} \quad S = \{1,2,3\} \end{cases} \tag{5.17}$$

Under the Shapley value allocation mechanism, the estimated shares of the peak demand for individual players are:

$$\begin{aligned} R_1(\mathbf{x}) &= \frac{(0)!(3-0-1)!}{3!}(v_1 - v_0) + \frac{(1)!(3-1-1)!}{3!}(v_4 - v_2) \\ &+ \frac{(1)!(3-1-1)!}{3!}(v_5 - v_3) + \frac{(2)!(3-2-1)!}{3!}(v_7 - v_6) \qquad (5.18) \\ R_2(\mathbf{x}) &= \frac{(0)!(3-0-1)!}{3!}(v_2 - v_0) + \frac{(1)!(3-1-1)!}{3!}(v_4 - v_1) \\ &+ \frac{(1)!(3-1-1)!}{3!}(v_6 - v_3) + \frac{(2)!(3-2-1)!}{3!}(v_7 - v_5) \qquad (5.19) \\ R_3(\mathbf{x}) &= \frac{(0)!(3-0-1)!}{3!}(v_3 - v_0) + \frac{(1)!(3-1-1)!}{3!}(v_5 - v_1) \\ &+ \frac{(1)!(3-1-1)!}{3!}(v_6 - v_2) + \frac{(2)!(3-2-1)!}{3!}(v_7 - v_4) \qquad (5.20) \end{aligned}$$

5.2.2 Feasible Solution Sets

Thermal network models are used to characterize the dynamics and constraints of building thermal loads. The indoor temperature of building n is described by a linear state-space model:

$$\mathbf{r}_n^{t+1} = \mathbf{A}_n \mathbf{r}_n^t + \mathbf{B}_{w,n}\mathbf{u}_n^t + \mathbf{B}_{u,n} x_n^t, \forall n \in \mathcal{N} \tag{5.21}$$

$$T_n^{t+1} = \mathbf{C}_n \mathbf{r}_n^{t+1}, \forall n \in \mathcal{N} \tag{5.22}$$

where $\mathbf{r}$ is the state vector consisting of all nodal temperatures in the thermal network, $\mathbf{u}$ contains all the uncontrollable inputs such as ambient weather conditions and internal heat gains, and x_n^t is the cooling power of the air-conditioning system. The state-space matrices $\mathbf{A}$, $\mathbf{B}_w$, $\mathbf{B}_u$ and $\mathbf{C}$ are constructed with the thermal resistances and capacitances of the building thermal network; the details of the modeling approach can be found in [101].

The following indoor temperature constraints need to be satisfied through the entire control horizon to ensure indoor comfort.

$$\underline{T}_n^t \leq T_n^t \leq \overline{T}_n^t, \forall t \in \mathcal{T}, \forall n \in \mathcal{N} \tag{5.23}$$

where $\underline{T}_n^t$ and $\overline{T}_n^t$ are the lower and upper bounds of the comfortable temperature zone. The air-conditioning power should be bounded by the system capacity $\overline{x}_n$ for building n, i.e.,

$$0 \leq x_n^t \leq \overline{x}_n, \forall t \in \mathcal{T}, \forall n \in \mathcal{N} \tag{5.24}$$

Constraints presented in Equation 5.21 to Equation 5.24 can be reformulated as $\mathbb{R}^{m_n} \ni \mathbf{g}_n(\mathbf{x}_n) := \mathbf{D}_n \mathbf{x}_n - \mathbf{b}_n \geq \mathbf{0}$ and the strategy set of building n is $\mathcal{X}_n = \{\mathbf{x}_n | \quad \mathbf{g}_n(\mathbf{x}_n) \geq \mathbf{0}\}$. The feasible set of the whole game is given as

$$\mathcal{X} = \mathcal{X}_1 \times \mathcal{X}_2 \times ... \times \mathcal{X}_N = \{\mathbf{x} | \mathbf{g}(\mathbf{x}) \geq 0\} \tag{5.25}$$

where $\mathbf{g}(\mathbf{x}) = \{\mathbf{g}_n\}_{n \in \mathcal{N}} \in \mathbb{R}^M$ and $M = m_1 + ... + m_N$. The function $\mathbf{g}$ is a mapping from

$\mathbb{R}^{NT}$ to $\mathbb{R}^{M}$

5.2.3 Nash Equilibrium Problem

The game problem $\mathcal{G} = \langle \mathcal{X}, \mathbf{w} \rangle$ described above is a typical NEP summarized as below:

1) Players: buildings in set $\mathcal{N}$.

2) Cost function: $w_n(\mathbf{x}_n, \mathbf{x}_{-n})$ for building player n.

3) Strategy set: $\mathcal{X} = \prod_{n \in \mathcal{N}} \mathcal{X}_n \subseteq \mathbb{R}^{NT}$ is nonempty, compact and convex.

A vector $\mathbf{x}^* = (\mathbf{x}_n^*, \mathbf{x}_{-n}^*) \in \mathcal{X}$ is called a NE if $w_n(\mathbf{x}_n^*, \mathbf{x}_{-n}^*) \leq w_n(\mathbf{x}_n, \mathbf{x}_{-n}^*), \forall \mathbf{x}_n \in \mathcal{X}_n$ and $\forall n \in \mathcal{N}$. At a NE, no player can lower his/her cost by unilaterally changing his/her strategy.

Note that the max operator is not everywhere differentiable in its domain. To make this problem easier to solve, the max operator is approximated with the log-sum-exponential function:

Model approximation: Replace $\max_{t \in \mathcal{T}}\{x^t\}$ with the smooth function $\frac{1}{\hat{k}}\log\left(\sum_{t=1}^{T} e^{\hat{k}x^t}\right)$ where $\hat{k}$ assumes a large constant value. The following bounds can be derived for this approximation.

$$\begin{aligned}
\max_{t \in \mathcal{T}}\{x^t\} &= \frac{1}{\hat{k}}\log\left(e^{\hat{k}\max\{x^t\}}\right) \leq \frac{1}{\hat{k}}\log\left(\sum_{t=1}^{T} e^{\hat{k}x^t}\right) \\
&\leq \frac{1}{\hat{k}}\log\left(Te^{\hat{k}\max\{x^t\}}\right) \\
&= \max_{t \in \mathcal{T}}\{x^t\} + \frac{\log(T)}{\hat{k}} \qquad (5.26)
\end{aligned}$$

Therefore, the approximation error is bounded by $\log(T)/\hat{k}$ and vanishes as $\hat{k} \to \infty$. Convexity is preserved in the surrogate log-sum-exponential model. A sketch of the proof is given here for completeness through verifying the positive semidefiniteness of the Hessian matrix. For simplicity, it is assumed that $\hat{k} = 1$. Then the subsequent equation can be obtained:

$$\nabla^2 f(x) = \frac{1}{\mathbf{1}^\intercal \varrho}\text{diag}(\varrho) - \frac{1}{(\mathbf{1}^\intercal \varrho)^2}\varrho\varrho^\intercal \tag{5.27}$$

where $\varrho = (e^{x^t})_{t=1}^T$ and diag(ϱ) is the diagonal matrix whose diagonal elements are those in ϱ. To show the Hessian matrix $\nabla^2 f(x) \succeq 0$, $\mathbf{b}^\intercal \nabla^2 f(x)\mathbf{b} \geq 0$ should be verified for all $\mathbf{b} = (b_1, ..., b_T)^\intercal \in \mathbb{R}^T$:

$$\mathbf{b}^\intercal \nabla^2 f(x)\mathbf{b} = \frac{(\sum_t \varrho_t b_t^2)(\sum_t \varrho_t) - (\sum_t \varrho_t b_t)^2}{(\sum_t \varrho_t)^2} \geq 0 \tag{5.28}$$

since $(\sum_t \varrho_t b_t^2)(\sum_t \varrho_t) - (\sum_t \varrho_t b_t)^2 \geq 0$ (Cauchy-Schwarz inequality). According to the equality conditions of Cauchy-Schwarz inequality, Equation 5.28 is equal to zero if and only if b_i's are all identical.

5.2.4 Existence and Uniqueness of Nash Equilibrium

If the $\max$ function is replaced with log-sum-exponential function in Equation 5.15 and the player n's demand charge function $R_n(\mathbf{x})$ is modified accordingly, w_n can be obtained as follows:

$$\begin{aligned} w_n(\mathbf{x}) \;\; = \;\; & \left(\sum_{t=1}^{T} p^t \cdot x_n^t\right) + p_d \cdot \sum_{S_n \subseteq \mathcal{N} \setminus \{n\}, j=1}^{j=2^{N-1}} \left(\pi_{s_{n,j}} \frac{1}{\hat{k}} \log(\mathbf{1}^\top \mathbf{exp}(\hat{k} \cdot \mathbf{H}_{s_{n,j}} \mathbf{x}))\right. \\ & \left. -\pi_{s_{n,j}} \frac{1}{\hat{k}} \log(\mathbf{1}^\top \mathbf{exp}(\hat{k} \cdot \overline{\mathbf{H}}_{s_{n,j}} \mathbf{x}))\right), \forall n \in \mathcal{N}, \end{aligned} \tag{5.29}$$

where

$$\pi_{s_{n,j}} = \frac{(|S_{n,j}|)!(|\mathcal{N}| - |S_{n,j}| - 1)!}{|\mathcal{N}|!}, \tag{5.30}$$

$$\mathbf{H}_{s_{n,j}} = \Big((\mathbf{H}^{i}_{s_{n,j}})_{i=1}^{N}\Big)^{\intercal}, \mathbf{H}^{i}_{s_{n,j}} = \begin{cases} \mathbf{I}^{T\times T} & i \in S_{n,j} \cup \{n\} \\ \mathbf{0}^{T\times T} & otherwise \end{cases} \tag{5.31}$$

$$\overline{\mathbf{H}}_{s_{n,j}} = \Big((\overline{\mathbf{H}}^{i}_{s_{n,j}})_{i=1}^{N}\Big)^{\intercal}, \overline{\mathbf{H}}^{i}_{s_{n,j}} = \begin{cases} \mathbf{I}^{T\times T} & i \in S_{n,j} \\ \mathbf{0}^{T\times T} & otherwise \end{cases} \tag{5.32}$$

where the operator $\mathbf{exp}(\mathbf{x})$ performs point-wise exponential of elements in $\mathbf{x}$, i.e., $\mathbf{exp}(\mathbf{x}) = (e^{x_i})_{x_i \in \mathbf{x}}$. The binary matrix $\mathbf{H}_{s_{n,j}} = (\mathbf{H}^{1}_{s_{n,j}}, ..., \mathbf{H}^{N}_{s_{n,j}}) \in \mathbb{B}^{T\times TN}$ indicates the control variables of the players in the alliance $S_{n,j}$ with the elements $\mathbf{H}^{n}_{S_{n,j}}$, $n \in \mathcal{N}$. $\mathbf{I}_T$ denote $T\times T$ identity matrix, $\mathbf{0}_T$ denote $T\times T$ zeros matrix. For example, consider a game with three players and two time slots, i.e., $\mathcal{N} = \{1, 2, 3\}$, $\mathcal{T} = \{1, 2\}$ and $\mathbf{x} = [x_1^1, x_1^2, x_2^1, x_2^2, x_3^1, x_3^2]^{\top}$. The first player's cost function is

$$\begin{aligned} w_1(\mathbf{x}_1, \mathbf{x}_{-1}) &= \left(\sum_{t=1}^{2} p^t \cdot x_1^t\right) + p_d \cdot R_1 \\ &\cong \left(\sum_{t=1}^{2} p^t \cdot x_1^t\right) + p_d\Big(\frac{1}{3}\big(\log(e^{x_1^1} + e^{x_1^2})\big) \\ &+ \frac{1}{6}\big(\log(e^{x_1^1+x_2^1} + e^{x_1^2+x_2^2}) - \log(e^{x_2^1} + e^{x_2^2})\big) \\ &+ \frac{1}{6}\big(\log(e^{x_1^1+x_3^1} + e^{x_1^2+x_3^2}) - \log(e^{x_3^1} + e^{x_3^2})\big) \\ &+ \frac{1}{3}\big(\log(e^{x_1^1+x_2^1+x_3^1} + e^{x_1^2+x_2^2+x_3^2}) - \log(e^{x_2^1+x_3^1} + e^{x_2^2+x_3^2})\big)\Big) \end{aligned} \tag{5.33}$$

The family of coalitions including the player 1 is $S_1 \cup \{1\} = \{\{1\},\{1,2\},\{1,3\},\{1,2,3\}\}$. The corresponding $\mathbf{H}_{s_{1,j}}$ of each alliance can be expressed as

$$\mathbf{H}_{s_{1,j}} = \begin{cases} \mathbf{H}_{s_{1,1}} = \begin{pmatrix} \mathbf{I}_2 & \mathbf{0}_2 & \mathbf{0}_2 \end{pmatrix} & for \quad S_{1,j} \cup \{1\} = \{1\} \\ \mathbf{H}_{s_{1,2}} = \begin{pmatrix} \mathbf{I}_2 & \mathbf{I}_2 & \mathbf{0}_2 \end{pmatrix} & for \quad S_{1,j} \cup \{1\} = \{1,2\} \\ \mathbf{H}_{s_{1,3}} = \begin{pmatrix} \mathbf{I}_2 & \mathbf{0}_2 & \mathbf{I}_2 \end{pmatrix} & for \quad S_{1,j} \cup \{1\} = \{1,3\} \\ \mathbf{H}_{s_{1,4}} = \begin{pmatrix} \mathbf{I}_2 & \mathbf{I}_2 & \mathbf{I}_2 \end{pmatrix} & for \quad S_{1,j} \cup \{1\} = \{1,2,3\} \end{cases} \tag{5.34}$$

and $\overline{\mathbf{H}}_{s_{1,j}}$ is given by

$$\overline{\mathbf{H}}_{s_{1,j}} = \begin{cases} \overline{\mathbf{H}}_{s_{1,1}} = \begin{pmatrix} \mathbf{0}_2 & \mathbf{0}_2 & \mathbf{0}_2 \end{pmatrix} & for \quad S_{1,j} = \{0\} \\ \overline{\mathbf{H}}_{s_{1,2}} = \begin{pmatrix} \mathbf{0}_2 & \mathbf{I}_2 & \mathbf{0}_2 \end{pmatrix} & for \quad S_{1,j} = \{2\} \\ \overline{\mathbf{H}}_{s_{1,3}} = \begin{pmatrix} \mathbf{0}_2 & \mathbf{0}_2 & \mathbf{I}_2 \end{pmatrix} & for \quad S_{1,j} = \{3\} \\ \overline{\mathbf{H}}_{s_{1,4}} = \begin{pmatrix} \mathbf{0}_2 & \mathbf{I}_2 & \mathbf{I}_2 \end{pmatrix} & for \quad S_{1,j} = \{2,3\} \end{cases} \tag{5.35}$$

Existence of NE Since the log-sum-exponential function is smooth and convex everywhere in its domain, Equation 5.29 is C^2 in both $\mathbf{x}_n$ and $\mathbf{x}_{-n}$, Theorem 4 guarantees the existence of NE for this game.

Uniqueness of NE The uniqueness solution of NE solution can be proven using the well-developed uniqueness theorem of VI. Assume $\mathbf{F}(\mathbf{x}) = (\nabla_{\mathbf{x}_n} w_n(\mathbf{x}))_{n=1}^N$, and by Theorem 3 and Section 5.1.4, this game admits a unique solution if the Jacobian matrix of $\mathbf{F}(\mathbf{x})$ below is positive definite for all $\mathbf{x} \in \mathcal{X}$:

$$\mathbf{F}(\mathbf{x}) = \begin{pmatrix} \nabla_{\mathbf{x}_1} w_1(\mathbf{x_1}, \mathbf{x_{-1}}) \\ \vdots \\ \nabla_{\mathbf{x}_N} w_N(\mathbf{x}_N, \mathbf{x}_{-N}) \end{pmatrix} \tag{5.36}$$

It may be noted that the term $\log(\mathbf{1}^\top \mathbf{exp}(\overline{\mathbf{H}}_{s_{n,j}})$ in w_n does not depend on the player n's control variables and therefore, its gradient with respect to $\mathbf{x}_n$ is equal to zero. For uniqueness analysis, this term from w_n can be safely dropped and the remaining terms can be analyzed. The truncated cost $\tilde{w}_n$ can be obtained by:

$$\tilde{w}_n(\mathbf{x}_n, \mathbf{x}_{-n}) \quad = \quad \left(\sum_{t=1}^{T} p^t \cdot x_n^t\right) + p_d \cdot \sum_{j=1}^{2^{N-1}} \left(\pi_{n,j} \cdot \frac{1}{\hat{k}} \cdot \log(\mathbf{1}^\top \mathbf{exp}(\hat{k} \cdot \mathbf{H}_{s_{n,j}} \mathbf{x}))\right) \tag{5.37}$$

where

$$\pi_{s_{n,j}} = \frac{(|S_{n,j}|)!(|\mathcal{N}| - |S_{n,j}| - 1)!}{|\mathcal{N}|!}$$

Assume that $\mathbf{p}_n = \nabla_{\mathbf{x}} \left(\sum_{t=1}^{T} p^t \cdot x_n^t\right) \in \mathbb{R}^{TN}$. Then the gradient of $\tilde{w}_n$ is

$$\nabla_{\mathbf{x}} \tilde{w}_n = \mathbf{p}_n + p_d \sum_{j=1}^{2^{N-1}} \left(\pi_{n,j} \cdot \left(\frac{1}{\left(\mathbf{1}^\top \mathbf{exp}(\hat{k} \cdot \mathbf{H}_{s_{n,j}} \mathbf{x})\right)} \cdot \mathbf{H}_{s_{n,j}}^\top \cdot \mathbf{exp}(\hat{k} \cdot \mathbf{H}_{s_{n,j}} \mathbf{x})\right)\right) \tag{5.38}$$

To obtain Equation 5.36, $\nabla_{\mathbf{x}} \tilde{w}_n$ needs only the gradient with respect to x_n. For convenience, the gradient with respect to x_{-n} of w_n can be set to zero by replacing $\mathbf{H}_{s_{n,j}}^\intercal$ with $\mathbf{B}_n^\intercal = (\mathbf{B}_n^i)_{i=1}^N \in \mathbb{B}^{TN \times T}$ where

$$\mathbf{B}_n^i = \begin{cases} \mathbf{I}_T, & \text{if} \quad i = n \\ \mathbf{0}_T, & \text{otherwise} \end{cases} \tag{5.39}$$

For example, the game with three players with $\mathcal{N} = \{1, 2, 3\}$, $\mathcal{T} = \{1, 2\}$, and $\mathbf{x} = [x_1^1, x_1^2, x_2^1, x_2^2, x_3^1, x_3^2]^\top$ has the following form:

$$\mathbf{B}_n = \begin{cases} \mathbf{B}_1 = \begin{pmatrix} \mathbf{I}_2 & \mathbf{0}_2 & \mathbf{0}_2 \end{pmatrix} & for \quad n = 1 \\ \mathbf{B}_2 = \begin{pmatrix} \mathbf{0}_2 & \mathbf{I}_2 & \mathbf{0}_2 \end{pmatrix} & for \quad n = 2 \\ \mathbf{B}_3 = \begin{pmatrix} \mathbf{0}_2 & \mathbf{0}_2 & \mathbf{I}_2 \end{pmatrix} & for \quad n = 3 \end{cases} \tag{5.40}$$

Assume that

$$\nabla_{\mathbf{x}}\tilde{w}_n^* = \mathbf{p}_n + p_d \sum_{j=1}^{2^{N-1}} \left(\pi_{n,j} \cdot \left(\frac{1}{\left(\mathbf{1}^\top \mathbf{exp}(\hat{k} \cdot \mathbf{H}_{s_{n,j}}\mathbf{x})\right)} \cdot \mathbf{B}_n^\top \cdot \mathbf{exp}(\hat{k} \cdot \mathbf{H}_{s_{n,j}}\mathbf{x})\right)\right) \quad (5.41)$$

$\mathbf{F}$ can therefore be expressed as

$$\begin{aligned}\mathbf{F} &= \sum_{n=1}^{N} \nabla_{\mathbf{x}}\tilde{w}_n^* && (5.42)\\ &= \left(\sum_{n=1}^{N} \mathbf{p}_n\right) + p_d \left(\sum_{n=1}^{N}\sum_{j=1}^{2^{N-1}} \left(\pi_{n,j} \cdot \left(\frac{1}{\left(\mathbf{1}^\top \mathbf{exp}(\hat{k} \cdot \mathbf{H}_{s_{n,j}}\mathbf{x})\right)} \cdot \mathbf{B}_n^\top \cdot \mathbf{exp}(\hat{k} \cdot \mathbf{H}_{s_{n,j}}\mathbf{x})\right)\right)\right) && (5.43)\end{aligned}$$

The Jacobian matrix of $\mathbf{F}$ can be written as

$$\begin{aligned}\mathbf{JF} &= p_d \sum_{n=1}^{N}\sum_{j=1}^{2^{N-1}} \left(\pi_{n,j} \cdot \hat{k} \cdot \left(\frac{1}{(\mathbf{1}^\top \mathbf{exp}(\hat{k} \cdot \mathbf{H}_{s_{n,j}}\mathbf{x}))} \cdot \Big(\mathrm{diag}(\mathbf{exp}(\hat{k} \cdot \mathbf{H}_{s_{n,j}}\mathbf{x}))\mathbf{B_i}\Big)^\top \right.\right.\\ &\quad \left.\left. \cdot \mathbf{H}_{s_{n,j}} - \frac{1}{(\mathbf{1}^\top \mathbf{exp}(\hat{k} \cdot \mathbf{H}_{s_{n,j}}\mathbf{x}))^2} \mathbf{B}_n^\top \mathbf{exp}(\hat{k} \cdot \mathbf{H}_{s_{n,j}}\mathbf{x}) \mathbf{exp}(\hat{k} \cdot \mathbf{H}_{s_{n,j}}\mathbf{x})^\top \mathbf{H}_{s_{n,j}}\right)\right)\\ &= p_d \sum_{n=1}^{N}\sum_{j=1}^{2^{N-1}} \left(\pi_{n,j} \cdot \hat{k} \cdot \Big(\mathbf{B}_n^\top \mathrm{diag}(\mathbf{g}_{s_{n,j}})\mathbf{H}_{s_{n,j}} \right.\\ &\quad \left. - \mathbf{B}_n^\top \mathbf{g}_{s_{n,j}} \mathbf{g}_{s_{n,j}}^\top \mathbf{H}_{s_{n,j}}\Big)\right)\\ &= \sum_{n=1}^{N}\sum_{j=1}^{2^{N-1}} \Big(\pi_{n,j} \cdot \hat{k} \cdot \big(\mathbf{B}_n^\top \mathbf{M}_{s_{n,j}} \mathbf{H}_{s_{n,j}}\big)\Big) && (5.44)\end{aligned}$$

where

$$\mathbf{g}_{s_{n,j}} = \frac{1}{(\mathbf{1}^\top \mathbf{exp}(\hat{k} \cdot \mathbf{H}_{s_{n,j}}\mathbf{x}))} \mathbf{exp}(\hat{k} \cdot \mathbf{H}_{s_{n,j}}\mathbf{x}), \quad \mathbf{M}_{s_{n,j}} = \mathrm{diag}(\mathbf{g}_{s_{n,j}}) - \mathbf{g}_{s_{n,j}} \mathbf{g}_{s_{n,j}}^\top$$

Assume that $\hat{S} = \{\hat{S}_1, ..., \hat{S}_{2^N}\}$ is a family of combinatorial subsets of the set of all players and corresponding weight associated with each coalition is $\hat{r} = (\hat{\pi}_l)_{l=1}^{2^N}$. Since S_n is a family of combinatorial subsets of players that includes the player n, so if $n \in \hat{S}_l$ for some $l \in \{1, .., 2^N\}$, then it implies that $\hat{S}_l \in S_n$. Combining the alike terms of Equation 5.44 and replacing $\mathbf{M}_{s_{n,j}} \mathbf{H}_{s_{n,j}}$ with the corresponding $\mathbf{M}_{\hat{S}_l} \mathbf{H}_{\hat{s}_l}$, the following equation can be obtained:

$$\mathbf{JF} = \sum_{l=1}^{2^N} \hat{\pi}_l \big(\sum_{n \in \hat{S}_l} \mathbf{B}_n^\intercal \big) \mathbf{M}_{\hat{s}_l} \mathbf{H}_{\hat{s}_l} \tag{5.45}$$

By the definitions of $\mathbf{B}_n$ and $\mathbf{H}_{\hat{s}_l}$, a relationship between these two matrices can be established:

$$\sum_{n \in \hat{S}_l} (\mathbf{B}_n^\intercal) = \mathbf{H}_{\hat{s}_l}^\intercal, \forall \hat{S}_l \in \hat{S} \tag{5.46}$$

Therefore, Equation 5.44 can be re-written as

$$\mathbf{JF} = \sum_{l=1}^{2^N} \hat{\pi}_l \mathbf{H}_{\hat{s}_l}^\intercal \mathbf{M}_{\hat{s}_l} \mathbf{H}_{\hat{s}_l} \tag{5.47}$$

From Cauchy Schwarz inequality of Equation 5.28, it is easy to obtain that $\mathbf{x}^\top \mathbf{H}_{\hat{s}_l}^\top \mathbf{M}_{\hat{s}_l} \mathbf{H}_{\hat{s}_l} \mathbf{x}^\top \geq 0$ for any $\mathbf{x}$ and $\mathbf{x}^\top \mathbf{H}_{\hat{s}_l}^\top \mathbf{M}_{\hat{s}_l} \mathbf{H}_{\hat{s}_l} \mathbf{x}^\top = 0$ if and only if $\mathbf{x}^\top \mathbf{H}_{\hat{s}_l}^\top = y\mathbf{1}^\intercal$. The conclusion is that $\mathbf{JF} \succeq 0$ and $\mathbf{JF} = 0$ if and only if $\mathbf{x}^\top \mathbf{H}_{\hat{s}_l}^\top = y\mathbf{1}^\intercal$ with some $y \in \mathbb{R}$. To show that this problem has a uniqueness NE, it suffices to verify that $\mathbf{JF} \succ 0$ for all $\mathbf{x} \in \mathcal{X}$ (i.e., $\mathbf{x}$ that satisfies $\mathbf{x}^\top \mathbf{H}_{\hat{s}_l}^\top = y\mathbf{1}^\intercal$ is not in the feasible set $\mathcal{X}$). The vector $\mathbf{x}$ satisfying $\mathbf{x}^\top \mathbf{H}_{\hat{s}_l}^\top = y\mathbf{1}^\intercal$ means that $x_n^1 = x_n^2 = ... = x_n^T$ for all $n \in \mathcal{N}$, i.e., the electricity consumption is constant throughout the whole day for all buildings; this strategy would likely violate the building operational constraints considering the load variations from building to building and from hour to hour. In practical implementations, one can perform a quick feasibility check by imposing additional constraints of $x_n^1 = x_n^2 = ... = x_n^T$ for any $n \in \mathcal{N}$ before solving the NEP. If the modified problem is infeasible, then $\mathbf{JF} \succ 0$ for any $\mathbf{x} \in \mathcal{X}$ and the game has a unique NE.

5.3 Solution Algorithm for the NEP

5.3.1 Reformulate NEP as VI Problem

The control optimization problem for player n in the game problem $\mathcal{G} = \langle \mathcal{X}, \mathbf{w} \rangle$ described above is

$$\min_{\mathbf{x}_n} \{w_n(\mathbf{x}_n, \mathbf{x}_{-n}) | \mathbf{D}_n \mathbf{x}_n - \mathbf{b}_n \geq \mathbf{0}\}, \forall n \in \mathcal{N} \tag{5.48}$$

After introducing the Lagrange multipliers $\lambda_n \in \mathbb{R}_+^{m_n}$, the following Lagrangian function can be obtained:

$$L_n = w_n(\mathbf{x}_n, \mathbf{x}_{-n}) - \lambda_n^\intercal (\mathbf{D}_n \mathbf{x}_n - \mathbf{b}_n), \forall n \in \mathcal{N}, \lambda_n \in \mathbb{R}_+^{m_n}, \forall \mathbf{x}_n \in \mathbb{R}^T \tag{5.49}$$

Let $(\mathbf{x}_n^*, \lambda_n^*)$ be the saddle point of the following min-max problem for given $\mathbf{x}_{-n}^*$:

$$\max_{\lambda_n} \min_{\mathbf{x}_n} \{L_n(\mathbf{x}_n, \mathbf{x}_{-n}^*, \lambda_n) | \lambda_n \geq \mathbf{0}\}, \forall n \in \mathcal{N} \tag{5.50}$$

which is equivalent to

$$L_n(\mathbf{x}_n^*, \mathbf{x}_{-n}^*, \lambda_n) \leq L_n(\mathbf{x}_n^*, \mathbf{x}_{-n}^*, \lambda_n^*), \forall n \in \mathcal{N}, \forall \lambda_n \in \mathbb{R}_+^{m_n}, \forall \mathbf{x}_n \in \mathbb{R}^T \tag{5.51}$$

$$L_n(\mathbf{x}_n^*, \mathbf{x}_{-n}^*, \lambda_n^*) \leq L_n(\mathbf{x}_n, \mathbf{x}_{-n}^*, \lambda_n^*), \forall n \in \mathcal{N}, \forall \lambda_n \in \mathbb{R}_+^{m_n}, \forall \mathbf{x}_n \in \mathbb{R}^T. \tag{5.52}$$

Then, substituting the expression in Equation 5.49 for L_n in Equation 5.51 and Equation 5.52 leads to:

$$\begin{aligned}
& L_n(\mathbf{x}_n^*, \mathbf{x}_{-n}^*, \lambda_n^*) - L_n(\mathbf{x}_n^*, \mathbf{x}_{-n}^*, \lambda_n) \\
= \; & w_n(\mathbf{x}_n^*, \mathbf{x}_{-n}^*) - (\lambda_n^*)^\intercal(\mathbf{D}_n\mathbf{x}_n^* - \mathbf{b}_n) - w_n(\mathbf{x}_n^*, \mathbf{x}_{-n}^*) + \lambda_n^\intercal(\mathbf{D}_n\mathbf{x}_n^* - \mathbf{b}_n) \\
= \; & (\lambda_n - \lambda_n^*)^\intercal(\mathbf{D}_n\mathbf{x}_n^* - \mathbf{b}_n) \\
\geq \; & 0, \forall n \in \mathcal{N}, \forall \lambda_n \in \mathbb{R}_+^{m_n}, \forall \mathbf{x}_n \in \mathbb{R}^T \qquad (5.53)
\end{aligned}$$

and

$$\begin{aligned}
& L_n(\mathbf{x}_n, \mathbf{x}_{-n}^*, \lambda_n^*) - L_n(\mathbf{x}_n^*, \mathbf{x}_{-n}^*, \lambda_n^*) \\
= \; & w_n(\mathbf{x}_n, \mathbf{x}_{-n}^*) - (\lambda_n^*)^\intercal(\mathbf{D}_n\mathbf{x}_n - \mathbf{b}_n) - w_n(\mathbf{x}_n^*, \mathbf{x}_{-n}^*) + (\lambda_n^*)^\intercal(\mathbf{D}_n\mathbf{x}_n^* - \mathbf{b}_n) \\
= \; & w_n(\mathbf{x}_n, \mathbf{x}_{-n}^*) - w_n(\mathbf{x}_n^*, \mathbf{x}_{-n}^*) + (\mathbf{x}_n - \mathbf{x}_n^*)^\intercal(-\mathbf{D}_n^\intercal\lambda_n^*) \\
\geq \; & 0, \forall n \in \mathcal{N}, \forall \lambda_n \in \mathbb{R}_+^{m_n}, \forall \mathbf{x}_n \in \mathbb{R}^T \qquad (5.54)
\end{aligned}$$

Define $\mathbf{y}_n = (\mathbf{x}_n^\intercal, \lambda_n^\intercal)^\intercal$. The following compact inequality is obtained by adding the left and right sides of Equation 5.53 to the left and right sides of Equation 5.54, respectively:

$$\begin{aligned}
& w_n(\mathbf{x}_n, \mathbf{x}_{-n}^*) - w_n(\mathbf{x}_n^*, \mathbf{x}_{-n}^*) + (\mathbf{y}_n - \mathbf{y}_n^*)^\intercal\mathbf{\Phi}_n(\mathbf{y}_n^*) \geq 0, \\
& \forall n \in \mathcal{N}, \forall \lambda_n \in \mathbb{R}_+^{m_n}, \forall \mathbf{x}_n \in \mathbb{R}^T \qquad (5.55)
\end{aligned}$$

where

$$\begin{aligned}
\mathbf{\Phi}_n(\mathbf{y}_n^*) &= \begin{bmatrix} \mathbf{0} & -\mathbf{D}_n^\intercal \\ \mathbf{D}_n & \mathbf{0} \end{bmatrix} \mathbf{y}_n^* - \begin{bmatrix} \mathbf{0} \\ \mathbf{b}_n \end{bmatrix} \qquad (5.56) \\
&= \mathbf{\Upsilon}_n\mathbf{y}_n^* - \mathbf{\Sigma}_n. \qquad (5.57)
\end{aligned}$$

Therefore, in game problem $\mathcal{G} = \langle \mathcal{X}, \mathbf{w} \rangle$, the optimal strategy for each player n must satisfy Equation 5.55. Since w_n is a convex function on $\mathbf{x}_n$, w_n should satisfy:

$$\begin{aligned} & w_n(\mathbf{x}_n, \mathbf{x}^*_{-n}) - w_n(\mathbf{x}^*_n, \mathbf{x}^*_{-n}) \geq (\mathbf{x}_n - \mathbf{x}^*_n)^\intercal \nabla_{\mathbf{x}_n} w_n(\mathbf{x}^*_n, \mathbf{x}^*_{-n}), \\ & \forall n \in \mathcal{N}, \forall \lambda_n \in \mathbb{R}^{m_n}_+, \forall \mathbf{x}_n \in \mathbb{R}^T \end{aligned} \tag{5.58}$$

Therefore, the following inequality is a necessary condition of Equation 5.51 and Equation 5.52.

$$\begin{aligned} & (\mathbf{x}_n - \mathbf{x}^*_n)^\intercal \nabla_{\mathbf{x}_n} w_n(\mathbf{x}^*_n, \mathbf{x}^*_{-n}) + (\mathbf{y}_n - \mathbf{y}^*_n)^\intercal \mathbf{\Phi}_n(\mathbf{y}^*_n) \geq 0, \\ & \forall n \in \mathcal{N}, \forall \lambda_n \in \mathbb{R}^{m_n}_+, \forall \mathbf{x}_n \in \mathbb{R}^T \end{aligned} \tag{5.59}$$

Since all players have to satisfy Equation 5.59 in their optimal play, the NE problem is equivalent to finding a vector $\mathbf{y}^* = (\mathbf{y}^*_n)^N_{n=1}$ such that

$$\begin{cases} (\mathbf{x}_1 - \mathbf{x}^*_1)^\intercal \nabla_{\mathbf{x}_1} w_1(\mathbf{x}^*_1, \mathbf{x}^*_{-1}) + (\mathbf{y}_1 - \mathbf{y}^*_1)^\intercal \mathbf{\Phi}_1(\mathbf{y}^*_1) \geq 0, \forall \lambda_1 \in \mathbb{R}^{m_1}_+, \forall \mathbf{x}_1 \in \mathbb{R}^T \\ (\mathbf{x}_2 - \mathbf{x}^*_2)^\intercal \nabla_{\mathbf{x}_2} w_2(\mathbf{x}^*_2, \mathbf{x}^*_{-2}) + (\mathbf{y}_2 - \mathbf{y}^*_2)^\intercal \mathbf{\Phi}_2(\mathbf{y}^*_2) \geq 0, \forall \lambda_2 \in \mathbb{R}^{m_2}_+, \forall \mathbf{x}_2 \in \mathbb{R}^T \\ (\mathbf{x}_3 - \mathbf{x}^*_3)^\intercal \nabla_{\mathbf{x}_3} w_3(\mathbf{x}^*_3, \mathbf{x}^*_{-3}) + (\mathbf{y}_3 - \mathbf{y}^*_3)^\intercal \mathbf{\Phi}_3(\mathbf{y}^*_3) \geq 0, \forall \lambda_3 \in \mathbb{R}^{m_3}_+, \forall \mathbf{x}_3 \in \mathbb{R}^T \\ \quad \vdots \\ (\mathbf{x}_N - \mathbf{x}^*_N)^\intercal \nabla_{\mathbf{x}_N} w_N(\mathbf{x}^*_N, \mathbf{x}^*_{-N}) + (\mathbf{y}_N - \mathbf{y}^*_N)^\intercal \mathbf{\Phi}_N(\mathbf{y}^*_N) \geq 0, \forall \lambda_N \in \mathbb{R}^{m_N}_+, \forall \mathbf{x}_N \in \mathbb{R}^T \end{cases} \tag{5.60}$$

Therefore, the NE $(\mathbf{x}^*_n, \mathbf{x}^*_{-n})$ of the game problem $\mathcal{G} = \langle \mathcal{X}, \mathbf{w} \rangle$ should also satisfy the following compact inequality:

$$(\mathbf{x} - \mathbf{x}^*)^\intercal \mathbf{F}(\mathbf{x}^*) + (\mathbf{y} - \mathbf{y}^*)^\intercal \mathbf{\Psi}(\mathbf{y}^*) \geq 0, \forall \mathbf{x} \in \mathbb{R}^{NT}, \forall \mathbf{y} \in \mathbb{R}^{NT+M} \tag{5.61}$$

where $\mathbf{y} = (\mathbf{y}_n)_{n=1}^N$, $\mathbf{y}_n = (\mathbf{x}_n^\intercal, \lambda_n^\intercal)^\intercal$, and

$$\boldsymbol{\Psi}(\mathbf{y}) = \begin{bmatrix} \boldsymbol{\Upsilon}_1 & & & \\ & \boldsymbol{\Upsilon}_2 & & \\ & & \ddots & \\ & & & \boldsymbol{\Upsilon}_N \end{bmatrix} \mathbf{y} - \begin{bmatrix} \boldsymbol{\Sigma}_1 \\ \boldsymbol{\Sigma}_2 \\ \vdots \\ \boldsymbol{\Sigma}_N \end{bmatrix} \tag{5.62}$$

Since $\boldsymbol{\Upsilon}_n, \forall n \in \mathcal{N}$ is a skew-symmetric matrix, $\boldsymbol{\Psi}(\mathbf{y})$ satisfies the following equation:

$$\left(\boldsymbol{\Psi}(\mathbf{y}^*) - \boldsymbol{\Psi}(\mathbf{y})\right)^\intercal (\mathbf{y}^* - \mathbf{y}) \equiv 0 \tag{5.63}$$

Therefore, according to Definition 1, $\boldsymbol{\Psi}(\mathbf{y})$ is monotone. Since $\mathbf{JF}$ is positive definite, which has been proved in Section 5.2.4, Equation 5.61 represents a monotone VI problem.

5.3.2 Centralized Algorithm

To solve the game and find the NE, there are three commonly used methods:

- Best response method, which has a stringent convergence requirement that cannot be satisfied for the problem under study.
- Nikaido-Isoda (NI) function method, which features high computational complexity, has been examined in my prior work [102]. The solution returned by this method satisfies the necessary optimality conditions but may not be a NE.
- VI algorithm, which is reported in this section. It offers guaranteed global convergence under mild conditions and features less computational complexity than the NI method [102]. The solution obtained by the VI method is guaranteed to be a NE.

Firstly, this section presents a centralized solution algorithm as shown in Algorithm 1. Note that $\mathbf{I}^n$ is an $n \times n$ identity matrix. The convergence of the algorithm is discussed next. At each interaction, the new iterate $\mathbf{x}^{k+1}$ is generated by finding the root of Equation 5.69 and the new iterate lagrange multiplier λ^{k+1} is generated using a max function that guarantees that $\lambda^{k+1} \in \mathbb{R}_{+}^{M}$.

Algorithm 1 Customized centralized algorithm

```
Initial $j = 0, \mathbf{y}^j \in \mathbb{R}^{TN+M}, \epsilon_1 \geq 0, \epsilon_2 \geq 0,\ r_n = (\|\mathbf{D}_n^{\top}\mathbf{D}_n\| + \epsilon_1)^{\frac{1}{2}}, \forall n \in \mathcal{N}, \omega_z > \epsilon_2$
    $\mathbf{D} = \begin{bmatrix} \mathbf{D}_1 & & & \\ & \mathbf{D}_2 & & \\ & & \ddots & \\ & & & \mathbf{D}_N \end{bmatrix}$   (5.64)
    $\mathbf{E} = \begin{bmatrix} r_1\mathbf{I}^T & & & \\ & r_2\mathbf{I}^T & & \\ & & \ddots & \\ & & & r_N\mathbf{I}^T \end{bmatrix}$   (5.65)
    $\lambda = \begin{bmatrix} \lambda_1^{\top} & \lambda_2^{\top} & \dots & \lambda_N^{\top} \end{bmatrix}^{\top}$   (5.66)
    $\mathbf{P}^{-1} = \begin{bmatrix} \frac{1}{r_1}\mathbf{I}^{m_1} & & & \\ & \frac{1}{r_2}\mathbf{I}^{m_2} & & \\ & & \ddots & \\ & & & \frac{1}{r_N}\mathbf{I}^{m_N} \end{bmatrix}$   (5.67)
while $\omega_z > \epsilon_2$ do
    Newton's method to find $\mathbf{x}^{k+1}$ that satisfies:
    $\mathbf{F}(\mathbf{x}^{k+1}) - \mathbf{D}^{\top}\lambda^k + \mathbf{E}^{\top}(\mathbf{x}^{k+1} - \mathbf{x}^k) = \mathbf{0}$   (5.68)
    $\lambda^{k+1} = \max\left(\lambda^k - \mathbf{P}^{-1}(\mathbf{D}(2\mathbf{x}^{k+1} - \mathbf{x}^k) - \mathbf{b}), \mathbf{0}\right)$   (5.69)
    $\omega_z = \|\mathbf{x}^{k+1} - \mathbf{x}^k\| + \|\lambda^{k+1} - \lambda^k\|$   (5.70)
end
```

5.3.3 Convergence of Centralized Algorithm

For given $(\mathbf{x}^k, \lambda^k)$, the process for calculating $(\mathbf{x}^{k+1}, \lambda^{k+1})$ in Equation 5.69 and Equation 5.70 is equivalent to finding $(\mathbf{x}^{k+1}, \lambda^{k+1})$ satisfying the following two VI problems.

$$(\mathbf{x} - \mathbf{x}^{k+1})^\intercal \left(\mathbf{F}(\mathbf{x}^{k+1}) - \mathbf{D}^\intercal \lambda^k + \mathbf{E}(\mathbf{x}^{k+1} - \mathbf{x}^k)\right) \geq 0, \forall \mathbf{x} \in \mathbb{R}^{TN} \tag{5.71}$$

$$\begin{aligned}&(\lambda - \lambda^{k+1})^\intercal \big(\mathbf{D}\mathbf{x}^{k+1} - \mathbf{b} + \mathbf{D}(\mathbf{x}^{k+1} - \mathbf{x}^k)\\ &+\mathbf{P}(\lambda^{k+1} - \lambda^k)\big) \geq 0, \forall \lambda \in \mathbb{R}^M_+\end{aligned} \tag{5.72}$$

To obtain a structure similar to Equation 5.61, it is necessary to assemble a vector function $\mathbf{F}$, which already exists in Equation 5.71, and a vector function $\mathbf{\Psi}$, which can be obtained by adding $(\mathbf{x} - \mathbf{x}^{k+1})^\intercal(-\mathbf{D}^\intercal\lambda^{k+1} + \mathbf{D}^\intercal\lambda^{k+1})$ to the left-hand side of Equation 5.71. The following expression shows the modified Equation 5.71

$$\begin{aligned}&(\mathbf{x} - \mathbf{x}^{k+1})^\intercal \left(\mathbf{F}(\mathbf{x}^{k+1}) - \mathbf{D}^\intercal\lambda^{k+1} + \mathbf{D}^\intercal(\lambda^{k+1} - \lambda^k) + \mathbf{E}(\mathbf{x}^{k+1} - \mathbf{x}^k)\right) \geq 0,\\ &\forall \mathbf{x} \in \mathbb{R}^{TN}\end{aligned} \tag{5.73}$$

The following compact expression represents a necessary condition for Equation 5.73 and Equation 5.72

$$\begin{aligned}&(\mathbf{x} - \mathbf{x}^{k+1})^\intercal\mathbf{F}(\mathbf{x}^{k+1}) + (\mathbf{y} - \mathbf{y}^{k+1})^\intercal\mathbf{\Psi}(\mathbf{y}^{k+1})\\ \geq\ &(\mathbf{y} - \mathbf{y}^{k+1})^\intercal\mathbf{\Omega}(\mathbf{y}^k - \mathbf{y}^{k+1}), \forall \mathbf{x} \in \mathbb{R}^{TN}, \forall \mathbf{y} \in \mathbb{R}^{TN+M}\end{aligned} \tag{5.74}$$

where $\mathbf{y} = (\mathbf{y}_n)_{n=1}^N$, $\mathbf{y}_n = (\mathbf{x}_n^\intercal, \lambda_n^\intercal)^\intercal$,

$$\begin{aligned}\mathbf{\Omega} &= \begin{bmatrix} \mathbf{\Theta}_1 & & & \\ & \mathbf{\Theta}_2 & & \\ & & \ddots & \\ & & & \mathbf{\Theta}_N \end{bmatrix}, \mathbf{\Theta}_n = \begin{bmatrix} r_n\mathbf{I} & \mathbf{D}_n^\intercal \\ \mathbf{D}_n & r_n\mathbf{I} \end{bmatrix}, n \in \mathcal{N}, \\ \mathbf{\Psi}(\mathbf{y}) &= \begin{bmatrix} \mathbf{\Upsilon}_1 & & & \\ & \mathbf{\Upsilon}_2 & & \\ & & \ddots & \\ & & & \mathbf{\Upsilon}_N \end{bmatrix} \mathbf{y} - \begin{bmatrix} \mathbf{\Sigma}_1 \\ \mathbf{\Sigma}_2 \\ \vdots \\ \mathbf{\Sigma}_N \end{bmatrix}. \end{aligned} \tag{5.75}$$

If r_n satisfies the following criterion, $\mathbf{\Theta}_n$ is guaranteed to be a positive definite matrix

$$r_n^2 > \|\mathbf{D_n}^\intercal \mathbf{D}_n\|, \forall n \in \mathcal{N}, \tag{5.76}$$

where $\|\cdot\|$ is the spectral norm of the matrix (i.e., the largest singular value of matrix). $\mathbf{\Omega}$ is thus a positive definite matrix, as a block diagonal matrix is positive definite if and only if each diagonal block is positive definite. Note that if $\mathbf{y}^k = \mathbf{y}^{k+1}$, the right-hand side of Equation 5.74 becomes zero, and the structures of Equation 5.74 and Equation 5.61 become identical, i.e., $\mathbf{x}^{k+1}$ is the NE ($\mathbf{x}^*$).

Since $(\mathbf{x}^{k+1}, \lambda^{k+1})$ is the solution of Equation 5.74 for all $\mathbf{x} \in \mathbb{R}^{TN}$ and $\lambda \in \mathbb{R}_+^M$, the following inequality holds by substituting $\mathbf{x} = \mathbf{x}^*$ into Equation 5.74

$$\begin{aligned} & (\mathbf{x}^* - \mathbf{x}^{k+1})^\intercal \mathbf{F}(\mathbf{x}^{k+1}) + (\mathbf{y}^* - \mathbf{y}^{k+1})^\intercal \mathbf{\Psi}(\mathbf{y}^{k+1}) \\ \geq \; & (\mathbf{y}^* - \mathbf{y}^{k+1})^\intercal \mathbf{\Omega}(\mathbf{y}^k - \mathbf{y}^{k+1}) \end{aligned} \tag{5.77}$$

Multiplying both sides of Equation 5.77 by a negative sign, the following inequality can be obtained:

$$\begin{aligned} & (\mathbf{y}^{k+1} - \mathbf{y}^*)^\intercal \boldsymbol{\Omega}(\mathbf{y}^k - \mathbf{y}^{k+1}) \\ \geq \ & (\mathbf{x}^{k+1} - \mathbf{x}^*)^\intercal \mathbf{F}(\mathbf{x}^{k+1}) + (\mathbf{y}^{k+1} - \mathbf{y}^*)^\intercal \boldsymbol{\Psi}(\mathbf{y}^{k+1}) \end{aligned} \tag{5.78}$$

Since $\mathbf{F}$ and $\boldsymbol{\Psi}$ are both monotone, the following inequality can be obtained:

$$\begin{aligned} & (\mathbf{x}^{k+1} - \mathbf{x}^*)^\intercal \mathbf{F}(\mathbf{x}^{k+1}) + (\mathbf{y}^{k+1} - \mathbf{y}^*)^\intercal \boldsymbol{\Psi}(\mathbf{y}^{k+1}) \\ \geq \ & (\mathbf{x}^{k+1} - \mathbf{x}^*)^\intercal \mathbf{F}(\mathbf{x}^*) + (\mathbf{y}^{k+1} - \mathbf{y}^*)^\intercal \boldsymbol{\Psi}(\mathbf{y}^*) \\ \geq \ & 0 \end{aligned} \tag{5.79}$$

From Equation 5.79 and Equation 5.78, the following inequality can be obtained:

$$(\mathbf{y}^{k+1} - \mathbf{y}^*)^\intercal \boldsymbol{\Omega}(\mathbf{y}^k - \mathbf{y}^{k+1}) \geq 0 \tag{5.80}$$

Note that if two vectors $\hat{\mathbf{a}}$ and $\hat{\mathbf{b}}$ satisfy $\hat{\mathbf{b}}^\intercal \mathbf{M}(\hat{\mathbf{a}} - \hat{\mathbf{b}}) \geq 0$ and $\mathbf{M}$ is positive definite, the following property can be derived:

$$\begin{aligned} \|\hat{\mathbf{a}}\|_{\mathbf{M}}^2 &= \|\hat{\mathbf{b}} + (\hat{\mathbf{a}} - \hat{\mathbf{b}})\|_{\mathbf{M}}^2 \\ &= \|\hat{\mathbf{b}}\|_{\mathbf{M}}^2 + \|\hat{\mathbf{a}} - \hat{\mathbf{b}}\|_{\mathbf{M}}^2 + \hat{\mathbf{b}}^\intercal \mathbf{M}(\hat{\mathbf{a}} - \hat{\mathbf{b}}) \\ &\geq \|\hat{\mathbf{b}}\|_{\mathbf{M}}^2 + \|\hat{\mathbf{a}} - \hat{\mathbf{b}}\|_{\mathbf{M}}^2 \end{aligned} \tag{5.81}$$

where $\|\mathbf{x}\|_{\mathbf{M}}^2 = \mathbf{x}^\intercal \mathbf{M}\mathbf{x}$. The following inequality can be obtained by moving $\|\hat{\mathbf{a}} - \hat{\mathbf{b}}\|_{\mathbf{M}}^2$ from the right-hand side of Equation 5.81 to the left side:

$$\|\hat{\mathbf{b}}\|_{\mathbf{M}}^2 \leq \|\hat{\mathbf{a}}\|_{\mathbf{M}}^2 - \|\hat{\mathbf{a}} - \hat{\mathbf{b}}\|_{\mathbf{M}}^2 \tag{5.82}$$

Assuming $\hat{\mathbf{a}} = \mathbf{y}^k - \mathbf{y}^*$ and $\hat{\mathbf{b}} = \mathbf{y}^{k+1} - \mathbf{y}^*$, the following inequality can be obtained:

$$\|\mathbf{y}^{k+1} - \mathbf{y}^*\|^2_{\mathbf{\Omega}} \leq \|\mathbf{y}^k - \mathbf{y}^*\|^2_{\mathbf{\Omega}} - \|\mathbf{y}^k - \mathbf{y}^{k+1}\|^2_{\mathbf{\Omega}} \tag{5.83}$$

Since $0 \leq \|\mathbf{y}^{k+1} - \mathbf{y}^*\|^2_{\mathbf{\Omega}} \leq \|\mathbf{y}^0 - \mathbf{y}^*\|^2_{\mathbf{\Omega}}$, $\|\mathbf{y}^k - \mathbf{y}^{k+1}\|^2_{\mathbf{\Omega}} \to 0$ as $k \to \infty$. Then, it can be concluded that the sequence $\{\mathbf{y}^k\}$ is bounded and has at least one cluster point and at least one convergent subsequence. If $\mathbf{y}^* \in \mathbf{\Gamma}^* = \{\mathbf{y}^* | w_n(\mathbf{x}_n, \mathbf{x}_{-n}) - w_n(\mathbf{x}^*_n, \mathbf{x}_{-n}) + (\mathbf{y} - \mathbf{y}^*)^\intercal \mathbf{\Phi}_n(\mathbf{y}^*) \geq 0\}$ is a cluster point of the sequence $\{\mathbf{y}^k\}$, and the subsequence $\{\mathbf{y}^{ik}\}$ converges to $\mathbf{y}^*$. Because $\mathbf{y}^{ik} - \mathbf{y}^{ik+1}$ is continuous in $\mathbf{y}^{ik}$, then $\mathbf{y}^* - \mathbf{y}^{ik+1} = \lim_{i\to\infty}(\mathbf{y}^{ik} - \mathbf{y}^{ik+1}) = 0$ and $\mathbf{y}^*$ is a solution of Equation 5.61. Since $\|\mathbf{y}^k - \mathbf{y}^*\|^2_{\mathbf{\Omega}}$ is bounded nonincreasing and contains a convergent subsequence $\|\mathbf{y}^{ik} - \mathbf{y}^*\|^2_{\mathbf{\Omega}} \to 0$ as $ik \to \infty$, then $\|\mathbf{y}^k - \mathbf{y}^*\|^2_{\mathbf{\Omega}} \to 0$ as $k \to \infty$, i.e., $\{\mathbf{y}^k\}$ converges to $\{\mathbf{y}^*\}$.

5.3.4 Distributed Solution Method

In this section, a distributed solution to find the NE is presented. The iterative scheme of customized distributed method follows

$$\begin{aligned}
\mathbf{x}^{k+1}_n &= \arg\min_{\mathbf{x}_n} L_n(\mathbf{x}^{k+1}_n, \mathbf{x}^k_{-n}, \lambda^k_n) + \frac{p_d\hat{k}[(N-1)]}{2}||\mathbf{x}_n - \mathbf{x}^k_n||^2 \\
&\quad + \frac{r_n}{2}||\mathbf{x}_n - \mathbf{x}^k_n||^2, \forall n \in \mathcal{N}, \forall \lambda_n \in \mathbb{R}^{m_n}_+, \forall \mathbf{x}_n \in \mathbb{R}^T && (5.84) \\
\lambda^{k+1}_n &= \arg\max_{\lambda_n \geq \mathbf{0}} \Big(L_n(2\mathbf{x}^{k+1}_n - \mathbf{x}^k_n, \mathbf{x}^k_{-n}, \lambda_n) \\
&\quad - \frac{r_n}{2}||\lambda_n - \lambda^k_n||^2 \Big), \forall n \in \mathcal{N}, \forall \lambda_n \in \mathbb{R}^{m_n}_+, \forall \mathbf{x}_n \in \mathbb{R}^T && (5.85)
\end{aligned}$$

Equation 5.84 involves a smooth unconstrained optimization problem whose optimality condition is the gradient of the objective function with respect to $\mathbf{x}_n$ is equal to zero. In additionally, since λ^{k+1}_n is obtained by solving a quadratic optimization problem with $\lambda \in \mathbb{R}^{m_n}_+$, the close form of λ^{k+1}_n can be obtained by Equation 5.88 . The distributed algorithm implementation is given in Algorithm 2.

Algorithm 2 Customized Distributed Algorithm

```
Initial $j = 0$, $\mathbf{y_n}^j \in \mathbb{R}^{T+m_n}$, $\epsilon_1 \geq 0$, $\epsilon_2 \geq 0$, $r_n = (\|\mathbf{D}_n^\intercal \mathbf{D}_n\| + \epsilon_1)^{\frac{1}{2}}, \forall n \in \mathcal{N}$, $\omega_z > \epsilon_2$
while $\omega_z > \epsilon_2$ do
    Newton's method to find $\mathbf{x}_n^{k+1}$ that satisfies:
    $\nabla_{\mathbf{x}_n} w_n(\mathbf{x}_n^{k+1}, \mathbf{x}_{-n}^k) - \mathbf{D}_n^\intercal \lambda_n^k + \Big(r_n + p_s \hat{k}[(N-1)]\Big)(\mathbf{x}_n^{k+1} - \mathbf{x}_n^k) = 0$   (5.86)
    $\lambda_n^{k+1} = \max\big(\lambda_n^k - r_n^{-1}(\mathbf{D}_n(2\mathbf{x}_n^{k+1} - \mathbf{x}_n^k) - \mathbf{b}_n), \mathbf{0}\big)$   (5.87)
    $\omega_z = \|\mathbf{x}_n^{k+1} - \mathbf{x}_n^k\| + \|\lambda_n^{k+1} - \lambda_n^k\|$   (5.88)
end
```

Note that the convergence conditions of the distributed algorithm have not bee established yet. However, the distributed algorithm was able to converge with the generated solution identical to that returned by the centralized algorithm, in the simulation tests to be discussed next.

5.4 Simulation Case Study

In order to verify the effectiveness of the proposed game-theoretic control approach, three benchmarking control strategies are considered and introduced in the following subsections.

5.4.1 Baseline Control

During cooling seasons, higher zone air temperature (ZAT) settings are effective in lowering cooling power consumption. Therefore, the baseline control, which best represents the current practices, maintains the ZAT setpoint at the upper bound of the comfortable zone to minimize cooling energy consumption. The air-conditioning power is estimated by using the zone air temperature setpoint and the load model:

$$x_n^t = \max\Big(0, \mathbf{B}_u^{-1}(\mathbf{C}^{-1}\overline{T}_n^{t+1} - \mathbf{A}\mathbf{r}_n^t - \mathbf{B}_w\mathbf{u}_n^t)\Big) \tag{5.89}$$

5.4.2 Individual Optimal Control

A second benchmarking strategy, termed individual optimal control, is considered where each customer purchases electricity from the market independently under the same rate structure and optimizes his/her electricity usage schedule to minimize his/her electricity cost. The control problems across the different players are totally decoupled. For building n, the control problem is

$$\min_{\mathbf{x}_n \in \mathcal{X}_n} \left\{ \Big(\sum_{t=1}^{T} p^t \cdot x_n^t \Big) + p_d \cdot \max_{t \in \mathcal{T}} \{x_n^t\} \right\} \tag{5.90}$$

5.4.3 Centralized Control

A centralized and fully cooperative control strategy is evaluated, in which all customers coordinate with each other to minimize the collective electricity cost in Equation 5.12. The centralized control leads to the social optimum and deviations from it represent suboptimalities due to lack of cooperation. The centralized control problem has the following formulation

$$\min_{\mathbf{x} \in \mathcal{X}} \left\{ \Big(\sum_{t=1}^{T} p^t \cdot x^t \Big) + P_d \cdot \max_{t \in \mathcal{T}} \{x^t\} \right\}. \tag{5.91}$$

5.4.4 Case Study Descriptions

Simulation tests were carried out for six commercial buildings with the proposed and the three benchmarking control strategies. The thermal network model described in subsection 5.2.2 was used for both control decision making and the simulation testbed. The model was developed from field data collected in an office building in West Lafayette, IN and was replicated for the six-building case study assuming different occupancy schedules to represent diverse load patterns in a building cluster. Simulations with one-shot control optimization were performed for a typical summer day with actual weather data collected in the case study building [103]. However, the proposed strategy can also be implemented in a receding horizon scheme for continuous operations. Table 5.1 shows the time-of-use rates used in the simulation tests. The rate structure has two pricing periods, namely on-peak and off-peak periods. The on-peak period starts at 11:00 am and ends at 2:00 pm; the rest of the day is considered as off-peak. An all-time peak demand charge of 4$/kW is considered. The six buildings have very different baseline load profiles due to different occupancy schedules.

Table 5.1: Summer TOU Tariffs with demand charge

Rate periods	**Electricity price ($/kWh)**	**Hours**	**Demand charge ($/kW)**
On-peak	0.3	11:00 AM-2PM	4
Off-peak	0.1	2PM-11:00AM	

The thermal loads and control strategies vary from one building to anther driven by the different occupancy schedules. Figure 5.1 to Figure 5.12 depict the simulation test results for buildings #1 to #6, respectively, to illustrate the behaviors of the various players. The first subplot shows the cooling power associated with the different control strategies, and the second subplot presents the zone temperature trajectories along with the ZAT upper and lower bounds (dash-dotted lines). In the case study, the comfortable temperature band is assumed to be 21-23 °C during occupied hours and 19-25 °C during unoccupied hours. Figure 5.13 plots the variations of the aggregate power of all six buildings. The electricity costs for the various strategies are listed in Table 5.2.

In the baseline control results, the zone temperature is kept at the upper bound during occupied hours resulting in the lowest energy consumption. During unoccupied hours, the air-conditioning system is off and the indoor temperature floats within the comfort band. Due to the lack of coordination, the baseline control leads to the highest peak demand among the four strategies. From Table 5.2, it can be seen that the aggregate peak demand is lower than the sum of individual building demands due to the diverse baseline load patterns across different buildings. The demand charge differential represents one benefit of aggregation, under baseline control. Although the baseline strategy results in the lowest energy cost, the demand charge is the highest leading to the highest total cost among the four strategies.

For the individual optimal control, each customer minimizes his/her own electricity costs disregarding how other players behave. The performance is optimal if the building were to purchase electricity directly from the market. The individual control precools the building before occupied hours to store "cooling" energy into the building thermal mass. During peak load hours, the zone temperature is adjusted upwards which allows the stored cooling energy to be released to help offset the air-conditioning power. With this load shifting effect, the peak demand can be effectively reduced compared to the baseline strategy. In the individual optimal control, the air-conditioner operation time is longer than the baseline case, but each building's demand charge is much reduced. However, from Figure 5.13 it can clearly see that the individual control strategy causes new load peaks during the precooling and morning hours, since there is no coordination among the players.

The centralized control assumes full cooperation of all buildings in the aggregator. Therefore, the aggregate performance is optimal with the lowest total electricity cost. A major differentiating behavior compared to the individual control approach is that more aggressive precooling actions are utilized, which leads to the maximum peak demand reduction. Although the individual peaks are much higher compared to those associated with the other strategies, the aggregate peak demand is the lowest because the peaks of different players are shifted in time.

The game theoretic control approach, proposed in this study, results in depths of precooling between those of the centralized and individual optimal strategies. Deeper precooling is utilized compared to the individual control strategy to achieve more demand reductions of the whole community. However, the precooling power in the game theoretic approach is not as spiky as the centralized controller, since too high of an individual peak could cause a higher share of the collective demand charge (reflected by a high Shapley value). It can be seen that the game theoretic control strategy could achieve a Price of Anarchy of 1.019 for this specific case. This strategy achieves aggregate electricity cost savings of 8.9% compared to the individual controller and 11.5% compared to the baseline strategy. Also it can be seen that the individual building costs under the proposed game setting are the lowest for all buildings among the implementable strategies (baseline and individual), which is critical for alliance stability. For the centralized controller, it is not a trivial task to distribute the aggregate demand cost across the various buildings. This is why the demand and total costs are missing for the individual buildings under the centralized control in Table 5.2.

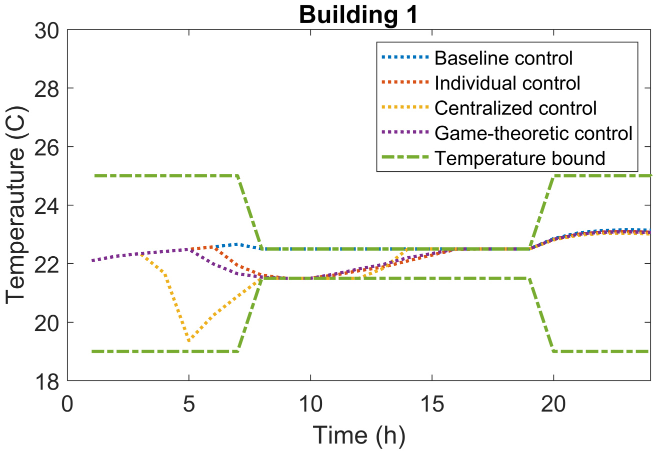

Figure 5.1: Zone temperature of building #1

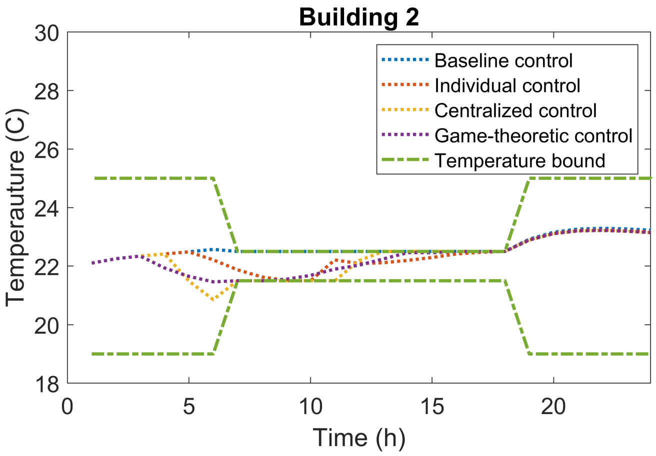

Figure 5.2: Zone temperature of building #2

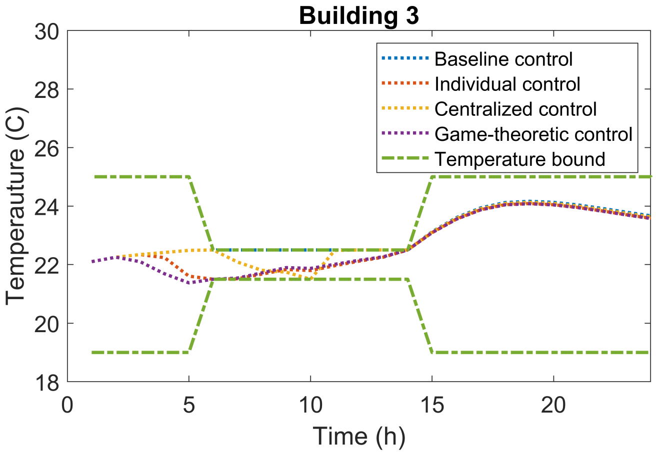

Figure 5.3: Zone temperature of building #3

5.5 Chapter Summary

This chapter presents a game-theoretic control strategy for demand response aggregators of buildings whose electricity cost includes a demand charge. The demand charge is based on the aggregate peak demand, which cannot be simply split across the participating buildings. This building cluster coordination problem is formulated as a Nash equilibrium problem where the Shapley value function is used to estimate the share of demand charge of each

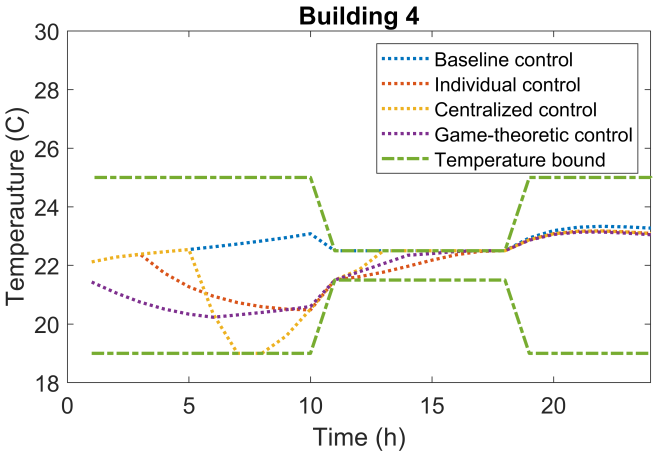

Figure 5.4: Zone temperature of building #4

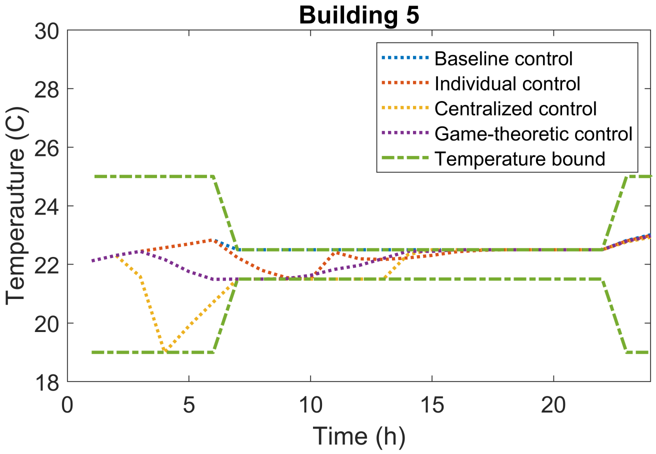

Figure 5.5: Zone temperature of building #5

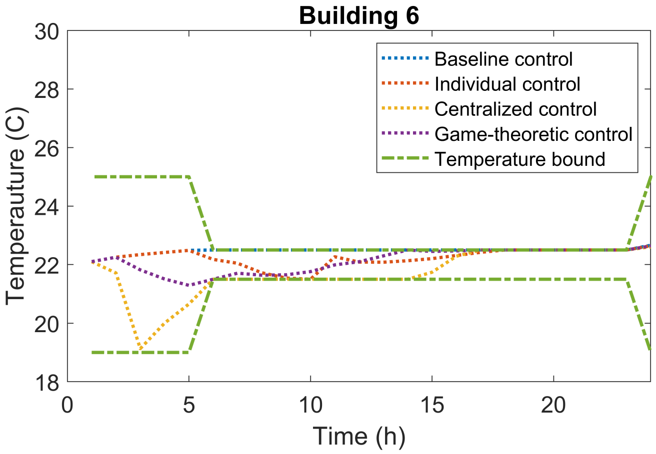

Figure 5.6: Zone temperature of building #6

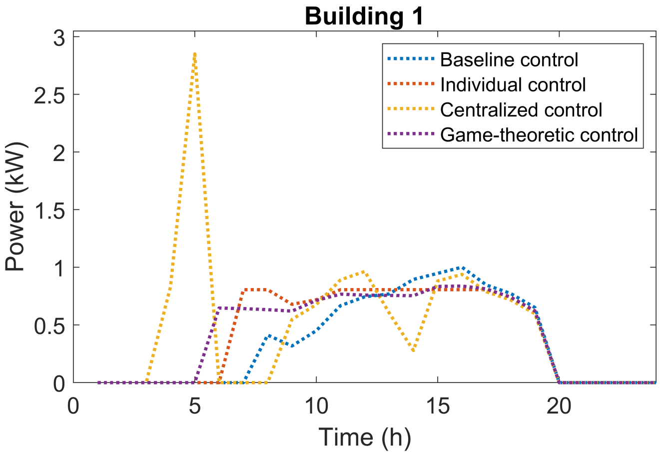

Figure 5.7: Power consumption of building #1

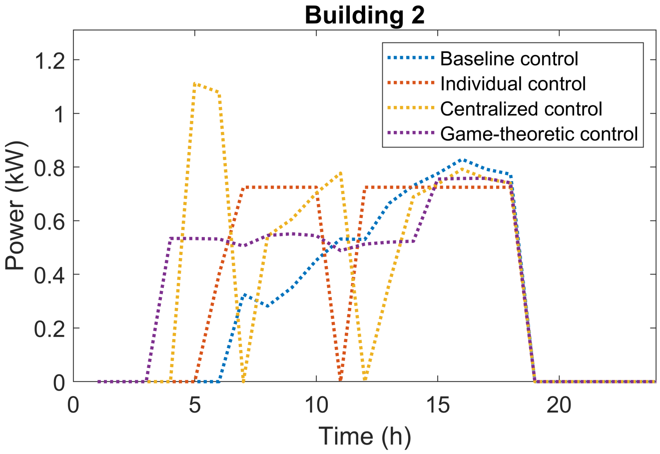

Figure 5.8: Power consumption of building #2

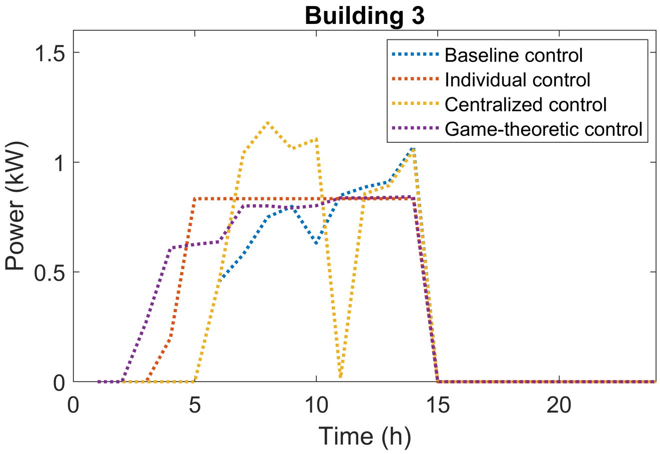

Figure 5.9: Power consumption of building #3

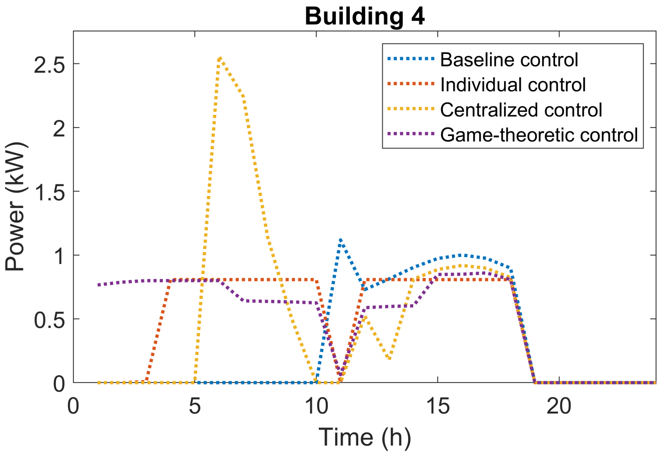

Figure 5.10: Power consumption of building #4

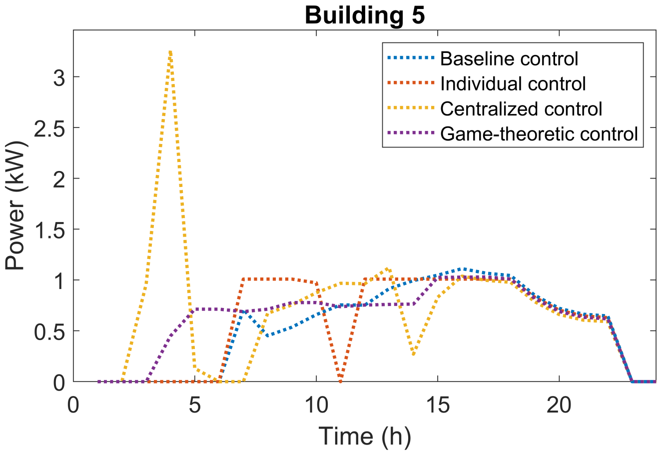

Figure 5.11: Power consumption of building #5

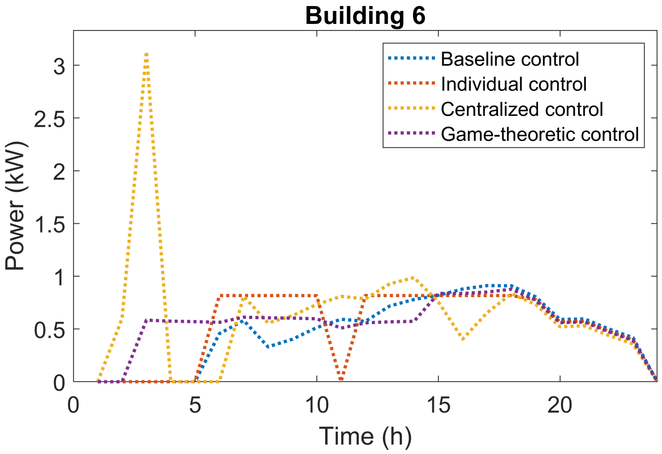

Figure 5.12: Power consumption of building #6

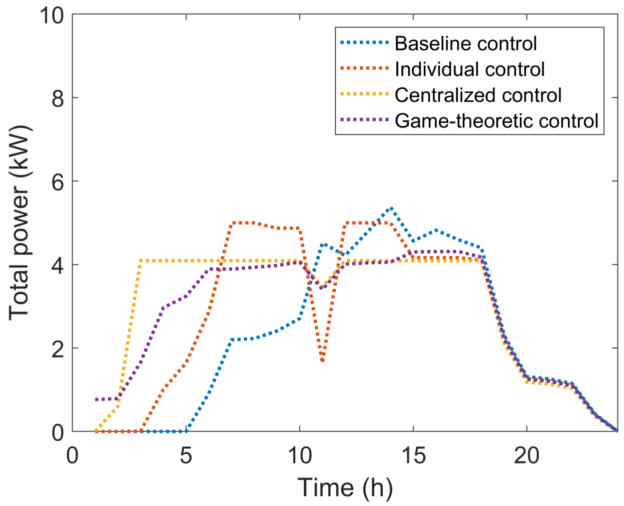

Figure 5.13: Total power consumption

Table 5.2: HVAC electricity costs for the various strategies

	Demand charge ($)				**Energy charge ($)**				**Total charge ($)**			
	Base	Indiv.	Cent.	Game	Base	Indiv.	Cent.	Game	Base	Indiv.	Cent.	Game
Bld #1	4.01	3.23	N/A	2.98	1.46	1.65	1.71	1.79	5.47	4.87	N/A	4.77
Bld #2	3.32	2.90	N/A	2.57	1.20	1.27	1.26	1.43	4.57	4.17	N/A	4.00
Bld #3	4.28	3.33	N/A	1.44	1.44	1.52	1.33	1.58	5.72	4.85	N/A	3.02
Bld #4	4.47	3.23	N/A	2.87	1.45	1.62	1.45	1.62	5.93	4.85	N/A	4.49
Bld #5	4.45	4.04	N/A	3.55	1.98	1.99	2.31	2.22	6.42	6.03	N/A	5.77
Bld #6	3.64	3.27	N/A	2.88	1.67	1.75	2.22	1.90	5.31	5.02	N/A	4.78
Sum of individual	24.17	20.00	N/A	16.60	9.20	10.55	10.28	9.86	33.36	29.79	N/A	27.15
Aggregate	21.49	20.00	16.37	16.60	10.55	9.80	10.28	9.86	30.69	29.79	26.64	27.15

building. Using the Lagrangian function, the game problem is transformed to an equivalent VI problem. Two algorithms are presented to solve the VI problem: a centralized algorithm and a distributed approach. The convergence conditions to NE solutions are discussed. Simulation tests of a six-building aggregator were carried out for the proposed strategy along with three benchmarking control methods and the game-theoretic control performance attained was very close to the social optimum with a Price of Anarchy of 1.019.

CHAPTER 6

MAKET-BASED GAME-THEORETIC CONTROL FOR FLEXIBLE LOAD DISPATCHING

In the preceding chapter, a game-theoretic control strategy for collective peak demand reduction of building clusters with a nonsmooth and non-strongly-convex function is presented, which uses a Shapely value function to allocate the collective cost among players. In this chapter, a game-theoretic control approach for flexible load dispatching with various marginal price models is presented. An NE problem is formulated and the existence and uniqueness of NE under various marginal price frameworks are discussed in Section 6.1. To evaluate the game-theoretic control performance for flexible load dispatching in a building clusters, a six-building simulation case study under a linear marginal price model is presented in Section 6.2 where a distributed best response method is used to find the NE. A chapter summary is given in Section 6.3.

6.1 Cost Model for Power Generation

The load dispatch problem and the corresponding non-cooperative game problem of concern in this chapter are similar to those discussed in Chapter 5. The player set, control variables and feasible action set are all identical to those described in Chapter 5. The major difference lies on the cost function and allocation mechanism. In this chapter, each player's impact on the collective performance is reflected by its influence on the marginal price of electricity generation and an individual's utility bill can be calculated as the marginal price multiplied by his/her electricity consumption; therefore, each building's cost is well defined and there is no need for cost allocation.

In this chapter, two families of marginal price models will be introduced, along with proof of the existence and uniqueness of NE under these two marginal price types. One cost model assumes the marginal electricity generation cost increases following a power function with the total load. The second model features an exponential increase of the marginal cost with total electrical demand.

6.1.1 Power Marginal Price Model

Assume that the marginal electricity generation cost p^t (with unit of \$/kWh) at each hour $t \in \mathcal{T}$ is dependent on the collective load following a power function:

$$p^t = a_h \cdot (\sum_{n=1}^{N} x_n^t)^{a_p} \tag{6.1}$$

where a_h and a_p are positive scalars. Under this setting, each building identifies his/her optimal control strategy given the rivals' control actions, i.e.,

$$\min_{\mathbf{x}_n \in \mathcal{X}_n} w_n(\mathbf{x}_n, \mathbf{x}_{-n}) = \sum_{t=1}^{T} p^t x_n^t = \sum_{t=1}^{T} a_h \Big(\sum_{n=1}^{N} x_n^t \Big)^{a_p} x_n^t \tag{6.2}$$

The second-order derivative of w_n with respect to $\mathbf{x}_n$ is:

$$\nabla^2_{\mathbf{x}_n} w_n(\mathbf{x}_n, \mathbf{x}_{-n}) = \begin{bmatrix} W_1 & 0 & 0 & \dots & 0 \\ 0 & W_2 & 0 & \dots & 0 \\ 0 & 0 & W_3 & \dots & 0 \\ \vdots & \vdots & \vdots & \ddots & \vdots \\ 0 & 0 & 0 & \dots & W_T \end{bmatrix} \tag{6.3}$$

where

$$W_i = \begin{cases} a_h a_p(a_p-1)(\sum_{n=1}^{N} x_n^i)^{a_p-2} x_n^i + 2a_h a_p(\sum_{n=1}^{N} x_n^i)^{a_p-1} & a_p \neq 1 \\ 2a_h a_p & a_p = 1 \end{cases}, \\ \forall i \in \mathcal{T} \tag{6.4}$$

Since $x_n^t \geq 0$ and $W_i \geq 0$, $\nabla^2_{\mathbf{x}_n} w_n$ is positive semidefinite. According to second-order derivative condition for convexity, $w_n(\mathbf{x}_n, \mathbf{x}_{-n})$ is convex in $\mathbf{x}_n$ for fixed $\mathbf{x}_{-n}$. Theorem 4 implies this game admits at least one NE. By Theorem 3 and Theorem 2, this game admits a unique solution if the Jacobian matrix of $\mathbf{F}(\mathbf{x})$ shown below is positive definite for all $\mathbf{x} \in \mathcal{X}$:

$$\mathbf{F}(\mathbf{x}) = \begin{pmatrix} \nabla_{\mathbf{x}_1} w_1(\mathbf{x_1}, \mathbf{x_{-1}}) \\ \vdots \\ \nabla_{\mathbf{x}_N} w_N(\mathbf{x}_N, \mathbf{x}_{-N}) \end{pmatrix} = \begin{pmatrix} \nabla_{\mathbf{x}_1^1} w_1(\mathbf{x_1}, \mathbf{x_{-1}}) \\ \nabla_{\mathbf{x}_1^2} w_1(\mathbf{x_1}, \mathbf{x_{-1}}) \\ \vdots \\ \nabla_{\mathbf{x}_1^T} w_1(\mathbf{x_1}, \mathbf{x_{-1}}) \\ \vdots \\ \nabla_{\mathbf{x}_N^1} w_N(\mathbf{x}_N, \mathbf{x}_{-N}) \\ \nabla_{\mathbf{x}_N^2} w_N(\mathbf{x}_N, \mathbf{x}_{-N}) \\ \vdots \\ \nabla_{\mathbf{x}_N^T} w_N(\mathbf{x}_N, \mathbf{x}_{-N}) \end{pmatrix} \tag{6.5}$$

$\hat{\mathbf{x}} = (x_1^1, x_2^1, ...x_N^1, \ldots, x_1^T, x_2^T, \ldots x_N^T)$ is defined by reordering/regrouping the entries of $\mathbf{x}$ $= (x_1^1, x_1^2, ...x_1^T, \ldots, x_N^1, x_N^2, \ldots x_N^T)$ according to the time index. The following matrix form can be obtained with the reordered vector $\hat{\mathbf{x}}$.

$$\mathbf{F}(\hat{\mathbf{x}}) = \begin{pmatrix} \nabla_{\mathbf{x}_1^1} w_1(\mathbf{x_1}, \mathbf{x_{-1}}) \\ \nabla_{\mathbf{x}_2^1} w_1(\mathbf{x_1}, \mathbf{x_{-1}}) \\ \vdots \\ \nabla_{\mathbf{x}_N^1} w_1(\mathbf{x_1}, \mathbf{x_{-1}}) \\ \vdots \\ \nabla_{\mathbf{x}_1^T} w_N(\mathbf{x}_N, \mathbf{x}_{-N}) \\ \nabla_{\mathbf{x}_2^T} w_N(\mathbf{x}_N, \mathbf{x}_{-N}) \\ \vdots \\ \nabla_{\mathbf{x}_N^T} w_N(\mathbf{x}_N, \mathbf{x}_{-N}) \end{pmatrix} \tag{6.6}$$

Since the derivative $\nabla_{\mathbf{x}_n^t} w_n(\mathbf{x}_n, \mathbf{x}_{-n}), \forall n \in \mathcal{N}, \forall t \in \mathcal{T}$ contains only the entries corresponding to time t, the Jacobian matrix $\mathbf{JF}(\hat{\mathbf{x}})$ can be expressed as a block diagonal matrix as follows:

$$\mathbf{JF}(\hat{\mathbf{x}}) \;\; = \;\; \begin{bmatrix} \mathbf{F}^1 & 0 & 0 & \dots & 0 \\ 0 & \mathbf{F}^2 & 0 & \dots & 0 \\ 0 & 0 & \mathbf{F}^3 & \dots & 0 \\ \vdots & \vdots & \vdots & \ddots & \vdots \\ 0 & 0 & 0 & \dots & \mathbf{F}^T \end{bmatrix}, \tag{6.7}$$

where

$$
\begin{aligned}
\mathbf{F}^t &= (f_{ij}) \in \mathbb{R}^{N\times N}, \forall t \in \mathcal{T} \\
f_{ij} &= \begin{cases} a_h a_p(a_p-1)(\sum_{n=1}^N x_n^t)^{a_p-2} x_i^t + a_h a_p(\sum_{n=1}^N x_n^t)^{a_p-1} & i \neq j, a_p \neq 1 \\ a_h a_p(a_p-1)(\sum_{n=1}^N x_n^t)^{a_p-2} x_i^t + 2a_h a_p(\sum_{n=1}^N x_n^t)^{a_p-1} & i = j, a_p \neq 1 \\ a_h a_p & i \neq j, a_p = 1 \\ 2a_h a_p & i = j, a_p = 1 \end{cases}, \\
& \forall i, j \in \mathcal{N}
\end{aligned}
\tag{6.8}
$$

It is clear that $\forall t \in \mathcal{T}$, $\mathbf{F}^t$ is a summation of a diagonal matrix and a rank-1 matrix, where the diagonal entries of the diagonal matrix are $a_h a_p(\sum_{n=1}^N x_n^t)^{a_p-1}$ and the rank-1 matrix is a matrix with identical columns and non-negative entries. Since $\sum_{n=1}^N x_n^t \geq 0$, the diagonal matrix is semi-positive definite. Therefore, It is obvious that $\mathbf{JF}$ is positive definite matrix if it satisfies the following condition:

- if $a_p > 1$ and $\sum_{n=1}^N x_n^t > 0, \forall t \in \mathcal{T}$, $\mathbf{JF}$ is positive definite.
- if $0 \leq a_p \leq 1$, $\mathbf{JF}$ is positive definite matrix.

6.1.2 Exponential Marginal Price Model

The second cost model assumes that the electricity generation cost $\bar{p}^t$ at each hour $t \in \mathcal{T}$ is exponentially dependent on the collective demand

$$
\bar{p}^t = \bar{a}_h \cdot \mathbf{exp}(\sum_{n=1}^N x_n^t), \tag{6.9}
$$

where $\bar{a}_h$ is positive parameter. The optimal control strategy for each building is given by

$$\min_{\mathbf{x}_n \in \mathcal{X}_n} w_n(\mathbf{x}_n, \mathbf{x}_{-n}) = \sum_{t=1}^{T} \bar{p}^t x_n^t = \sum_{t=1}^{T} \bar{a}_h \cdot \mathbf{exp}(\sum_{n=1}^{N} x_n^t) \cdot x_n^t \tag{6.10}$$

The second-order derivative of w_n with respect to $\mathbf{x}_n$ is

$$\nabla^2_{\mathbf{x}_n} w_n(\mathbf{x}_n, \mathbf{x}_{-n}) = \begin{bmatrix} \bar{w}_1 & 0 & 0 & \dots & 0 \\ 0 & \bar{w}_2 & 0 & \dots & 0 \\ 0 & 0 & \bar{w}_3 & \dots & 0 \\ \vdots & \vdots & \vdots & \ddots & \vdots \\ 0 & 0 & 0 & \dots & \bar{w}_N \end{bmatrix} \tag{6.11}$$

where

$$\bar{w}_i = \bar{a}_h \cdot \mathbf{exp}(\sum_{n=1}^{N} x_n^t) \cdot x_n^t + 2\bar{a}_h \cdot \mathbf{exp}(\sum_{n=1}^{N} x_n^t), \forall i \in \mathcal{N} \tag{6.12}$$

Since the diagonal entries $\bar{w}_i \geq 2\bar{a}_h > 0, \forall i \in \mathcal{N}$, the diagonal matrix $\nabla^2_{x_n} w_n(\mathbf{x}_n, \mathbf{x}_{-n})$ is a positive definite matrix, which guarantees the existence of NE according to Theorem 4. The Jacobian matrix of $\mathbf{F}(\hat{\mathbf{x}})$ is given by

$$\mathbf{JF}(\hat{\mathbf{x}}) \quad = \quad \begin{bmatrix} \bar{f}^1 & 0 & 0 & \dots & 0 \\ 0 & \bar{f}^2 & 0 & \dots & 0 \\ 0 & 0 & \bar{f}^3 & \dots & 0 \\ \vdots & \vdots & \vdots & \ddots & \vdots \\ 0 & 0 & 0 & \dots & \bar{f}^T \end{bmatrix} \tag{6.13}$$

where

$$\begin{aligned}
\bar{f}^t &= (\bar{f}_{ij}) \in \mathbb{R}^{N\times N}, \forall t \in \mathcal{T} \\
\bar{f}_{ij} &= \begin{cases} \bar{a}_h \cdot \mathbf{exp}(\sum_{n=1}^{N} x_n^t) \cdot x_i^t + \bar{a}_h \cdot \mathbf{exp}(\sum_{n=1}^{N} x_n^t) & i \neq j \\ \bar{a}_h \cdot \mathbf{exp}(\sum_{n=1}^{N} x_n^t) \cdot x_i^t + 2\bar{a}_h \cdot \mathbf{exp}(\sum_{n=1}^{N} x_n^t) & i = j \end{cases}, \\
& \forall i, j \in \mathcal{N}
\end{aligned} \tag{6.14}$$

Since $\mathbf{exp}(z) \geq 1, \forall z \geq 0$, the Jacobian matrix of $\mathbf{F}(\mathbf{x})$ is a positive definite matrix in the feasible set, which guarantees the uniqueness of NE according to Theorem 2. Following is a case study using a linear marginal price model to evaluate the effectiveness of game-theoretic control strategies.

6.2 Case Study with a Linear Marginal Price Model

In this section, a linear marginal cost model is used to numerically demonstrate a distributed NE solution algorithm. Under this assumption, the marginal electricity generation cost p^t (with unit of \$/kWh) at each hour $t \in \mathcal{T}$ is linearly dependent on the collective demand

$$p^t = a_h(\sum_{n=1}^{N} x_n^t) \tag{6.15}$$

where a_h is a positive scalar. Note that this linear price model is built based on the typical operating cost curve of the electricity market with respect to system power capacity, such as the one reported by PJM as shown in Figure 6.1. This linear price model is widely used in game theoretic-control analysis of electricity markets [52, 51].

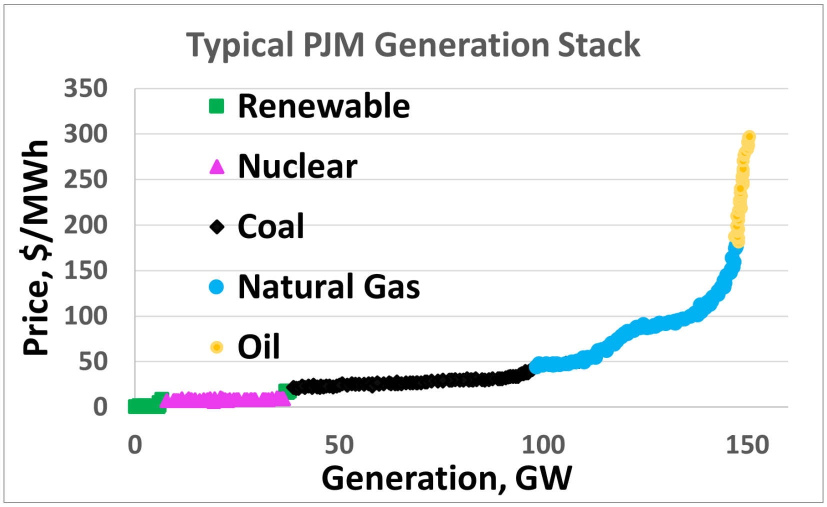

Figure 6.1: Typical operating cost curve. Source: The Pennsylvania State University (https://www.e-education.psu.edu/ebf200/node/151)

Under this setting, each building determines its optimal control strategy given the control activities of its rivals, i.e.,

$$\min_{\mathbf{x}_n \in \mathcal{X}_n} w_n(\mathbf{x}_n, \mathbf{x}_{-n}) = \sum_{t=1}^{T} p^t x_n^t = \sum_{t=1}^{T} \big(a_h \sum_{n=1}^{N} x_n^t\big) x_n^t \tag{6.16}$$

6.2.1 Distributed Algorithm

a. Best Response Algorithm

The best response $\mathcal{BR}_n(\mathbf{x})$ is the set of actions minimizing the cost function for player n under state $\mathbf{x}$:

$$\mathcal{BR}_n(\mathbf{x}) = \{\mathbf{x}_n | \mathbf{x}_n = \arg \min_{\mathbf{z}_n \in \mathcal{X}_n} w_n(\mathbf{z}_n, \mathbf{x}_{-n})\} \tag{6.17}$$

Therefore, $\mathbf{x}^*$ is the NE if and only if $\mathbf{x}_n^* \in \mathcal{BR}_n(\mathbf{x}^*)$ for every player n. A best response strategy is proposed which is implemented through Jacobi iterations, i.e., at each iteration only one player performs optimization to identify his/her optimal control actions $\mathbf{x}_n$ where $\mathbf{x}_{-n}$ assumes the most recent values. A pre-defined update sequence R is followed by the players, e.g., the round robin sequence $R = \{1, ..., N, 1, ..., N, 1, ...\}$.

Algorithm 3 Best Response Algorithm

```
Result: $\mathbf{x} = \mathbf{x}^k$ is a Nash equilibrium
Input: Initial state $\mathbf{x} := \mathbf{x}^0$; $k = 1$; $L := \varnothing$
while $size(L) \neq N$ do
    Pick next player $n := R^k$
    $\mathbf{x}_n^k = \mathcal{BR}_n(\mathbf{x}_n^{k-1}, \mathbf{x}_{-n}^{k-1})$
    $\mathbf{x}_{-n}^k = \mathbf{x}_{-n}^{k-1}$
    $e = ||\mathbf{x}^k - \mathbf{x}^{k-1}||$
    if $e = 0$ then
        $L := \varnothing$
    else
        $L := L \cup \{n\}$
    end
    $k = k + 1$
end
```

In this algorithm, $\mathbf{x}^0$ is chosen arbitrarily and the energy consumption schedules are sequentially updated based on the round robin sequence R. L is the list of players that have not changed their control actions since the last change of the state $\mathbf{x}$. It is reset to an empty list every time a player updates his/her actions. When this list reaches size N, a fixed point is obtained and the solution is a NE.

b. Convergence of the Algorithm

Theorem 5 ([104])**.** *In a potential game, from an arbitrary initial outcome, best response dynamics converge to a NE.*

By Theorem 5, to prove the convergence of the best response algorithm, it is sufficient to show that the game under concern is a potential game. The definition of potential game is given below

Definition 4 (Potential game)**.** Give a game $M := (\mathcal{X}_1, ..., \mathcal{X}_N, w_1, ..., w_N)$, where $\mathcal{X}_n$ is player n's strategy set and w_n is player n's cost function. The game M is a potential game if there exists a function $P : \mathcal{X}_1 \times ... \times \mathcal{X}_N \to \mathbb{R}$, such that $\forall n \in \mathcal{N}$, $\forall \mathbf{x}_{-n} \in \mathcal{X}_{-n}$, $\forall \mathbf{x}_n, \mathbf{x}_n^{'} \in \mathcal{X}_n$

$$w_n(\mathbf{x}_n, \mathbf{x}_{-n}) - w_n(\mathbf{x}_n^{'}, \mathbf{x}_{-n}) = P(\mathbf{x}_n, \mathbf{x}_{-n}) - P(\mathbf{x}_n^{'}, \mathbf{x}_{-n}) \tag{6.18}$$

Since w_n is a quadratic function, Equation 6.16 can be expressed as a linear function (i.e., $\mathbf{F}(\mathbf{x}) = \overline{\mathbf{F}}\mathbf{x}$).

Lemma 6. *The following function is a potential function of the NEP*

$$P(\mathbf{x}_n, \mathbf{x}_{-n}) = \frac{1}{2}\mathbf{x}^\top \overline{\mathbf{F}}\mathbf{x}. \tag{6.19}$$

Proof. Substituting the expression of $\overline{\mathbf{F}}$ into Equation 6.19, the following equation can be derived:

$$P(\mathbf{x}_n, \mathbf{x}_{-n}) = \frac{1}{2}\mathbf{x}^\top (\sum_{n=1}^{N}(a_h \mathbf{B}_n^\top \mathbf{B}_n + \mathbf{B}_n^\top \mathbf{A}))\mathbf{x} \tag{6.20}$$

For each player n and fixed strategy $\mathbf{x}_{-n}$ the following holds

$$\begin{aligned}
\nabla_{\mathbf{x}_n} P(\mathbf{x}_n, \mathbf{x}_{-n}) &= \mathbf{B}_n(\sum_{n=1}^{N}(a_h \mathbf{B}_n^\top \mathbf{B}_n + \mathbf{B}_n^\top \mathbf{A}))\mathbf{x} && (6.21)\\
&= \big(a_h \mathbf{B}_n(\sum_{n=1}^{N} \mathbf{B}_n^\top \mathbf{B}_n) + \mathbf{B}_n(\sum_{n=1}^{N} \mathbf{B}_n^\top)\mathbf{A}\big)\mathbf{x} && (6.22)\\
&= \big(a_h \mathbf{B}_n(\mathbf{I}) + \mathbf{B}_n \mathbf{B}_n^\top \mathbf{A}\big)\mathbf{x} && (6.23)\\
&= \big(a_h \mathbf{B}_n + (\mathbf{I})\mathbf{A}\big)\mathbf{x} && (6.24)\\
&= \big(a_h \mathbf{B}_n + \mathbf{A}\big)\mathbf{x} && (6.25)
\end{aligned}$$

$$\begin{aligned}
\nabla_{\mathbf{x}_n} w_n(\mathbf{x}_n, \mathbf{x}_{-n}) &= \mathbf{B}_n(a_h \mathbf{B}_n^\top \mathbf{B}_n + \mathbf{B}_n^\top \mathbf{A})\mathbf{x} && (6.26)\\
&= \big(a_h \mathbf{B}_n \mathbf{B}_n^\top \mathbf{B}_n + \mathbf{B}_n \mathbf{B}_n^\top \mathbf{A}\big)\mathbf{x} && (6.27)\\
&= \big(a_h \mathbf{B}_n(\mathbf{I}) + \mathbf{B}_n \mathbf{B}_n^\top \mathbf{A}\big)\mathbf{x} && (6.28)\\
&= \big(a_h \mathbf{B}_n + (\mathbf{I})\mathbf{A}\big)\mathbf{x} && (6.29)\\
&= \big(a_h \mathbf{B}_n + \mathbf{A}\big)\mathbf{x} && (6.30)
\end{aligned}$$

Clearly, one can obtain that $\nabla_{\mathbf{x}_n} w_n(\mathbf{x}_n, \mathbf{x}_{-n}) = \nabla_{\mathbf{x}_n} P(\mathbf{x}_n, \mathbf{x}_{-n})$. According to Theorem 7 shown below, $M := (\mathcal{X}_1, ..., \mathcal{X}_N, w_1, ..., w_N)$ is a potential game and therefore, the best response algorithm is convergent.

Theorem 7 ([60]). *Assuming that each player's strategy set $\mathcal{X}_n$ is a compact convex set and each utility function $w_n(\mathbf{x})$ is everywhere continuous and differentiable. Then $\nabla_{\mathbf{x}_n} w_n(\mathbf{x}_n, \mathbf{x}_{-n}) = \nabla_{\mathbf{x}_n} P(\mathbf{x}_n, \mathbf{x}_{-n})$ is equivalent to Equation 6.19.*

□

6.2.2 Case Study Results

In order to verify the effectiveness of the proposed game-theoretic control approach, two benchmarking control strategies are considered and introduced in the following subsections.

a. Baseline Control

The same baseline control strategy as described in Section 5.4.1 is considered as the first benchmark, where all zone temperatures are maintained at the comfortable upper bound for minimum cooling power consumption.

b. Centralized Control

A centralized and fully cooperative control strategy similar to that described in Section 5.4.2 is considered as a second benchmark. The major difference is on the central cost function:

$$\min_{\mathbf{x}\in\mathcal{X}} \sum_{t=1}^{T} \Big(a_h(\sum_{n=1}^{N} x_n^t) \cdot (\sum_{n=1}^{N} x_n^t) \Big). \tag{6.31}$$

d. Case Study Descriptions

Simulation tests were carried out with six commercial buildings with the proposed and the benchmarking control strategies. The six buildings have the same dynamics and operational constraints as those involved in the peak demand reduction aggregator case study. The thermal loads and control strategies vary from one building to another. Figure 6.2 to Figure 6.13 depict the simulation test results for buildings #1 and #6, respectively, to illustrate the behaviors of the various players. Figure 6.2 to Figure 6.7 present the zone temperature trajectories along with the zone air temperature (ZAT) upper and lower bounds (dash-dotted lines), and Figure 6.8 to Figure 6.13 show the cooling power associated with the different control strategies. Figure 6.14 plots the variations of the aggregate power of all six buildings. The electricity costs for the various strategies are listed in Table 6.1.

In the baseline control results, the zone temperature is kept at the upper bound during occupied hours resulting in the lowest energy consumption. During unoccupied hours, the air-conditioning system is off and the indoor temperature floats within the comfort band. Although the baseline strategy results in the lowest energy usage, the peak demand is the highest among the three strategies causing higher cost penalties. As a consequence, the resultant total electricity cost is the highest. The centralized control assumes full cooperation of all buildings and tends to precool the building in the early morning to flatten the load profile to reduce the electricity cost. It can be observed that the controller calls for precooling at different times in different buildings so that the collective demand trajectory is smooth, although individual building loads have occasional spikes. There is a tradeoff between the total electricity usage and peak demand. Aggressive precooling is effective in reducing peak demand but may result in higher total energy usage. The centralized controller identifies the balancing point leading to the lowest total electricity cost. The game theoretic distributed control approach, proposed in this study, results in very different behaviors in individual building loads compared to the centralized controller. In the distributed control results, the precooling power is smooth for all buildings since even small spikes can cause increases in the individual costs. However, the total demand profile of the game theoretic control case is very similar to that of the centralized results. Although the total cost associated with the game-theoretic distributed control strategy is slightly higher than the centralized controller, a lower PAR can be achieved. It can be seen that the game theoretic distributed control strategy could achieve a Price of Anarchy of 1.007 for this specific case and reduce the aggregate electricity cost by 6% compared to the baseline strategy. The detailed individual and total costs for all three control strategies are summarized in Table 6.1.

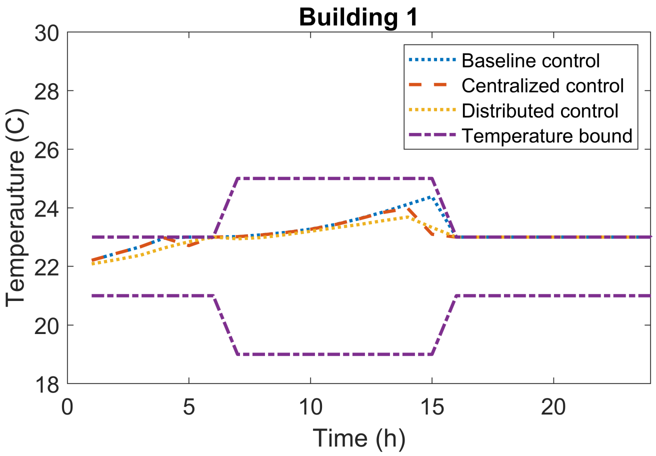

Figure 6.2: Zone temperature of building #1

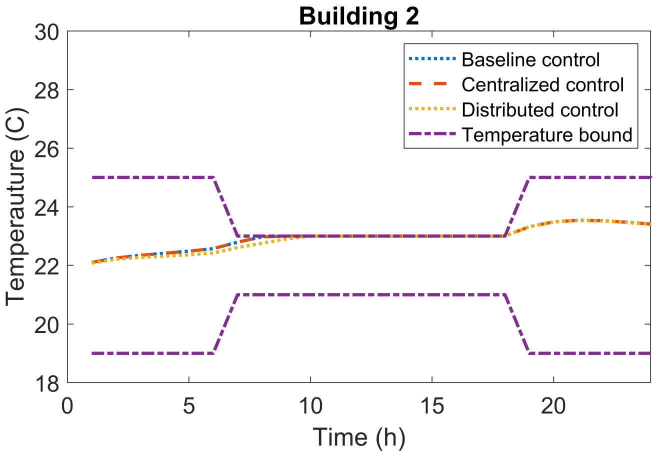

Figure 6.3: Zone temperature of building #2

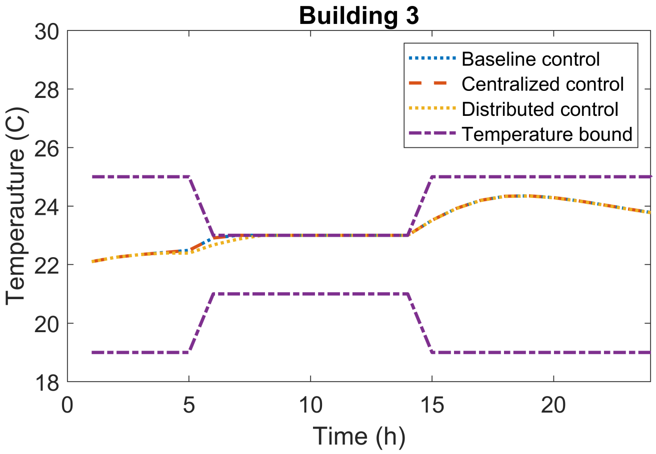

Figure 6.4: Zone temperature of building #3

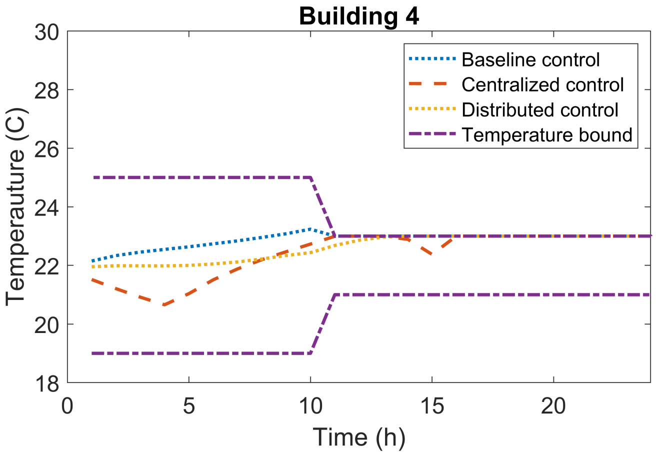

Figure 6.5: Zone temperature of building #4

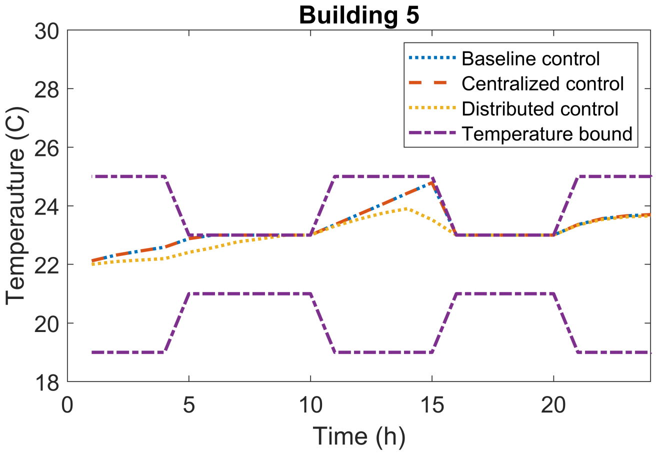

Figure 6.6: Zone temperature of building #5

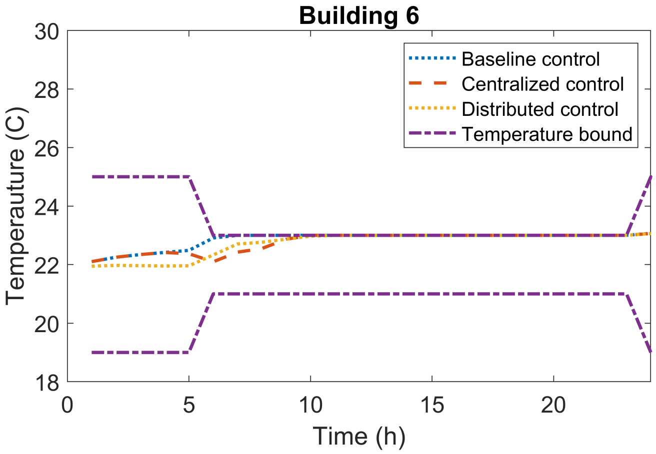

Figure 6.7: Zone temperature of building #6

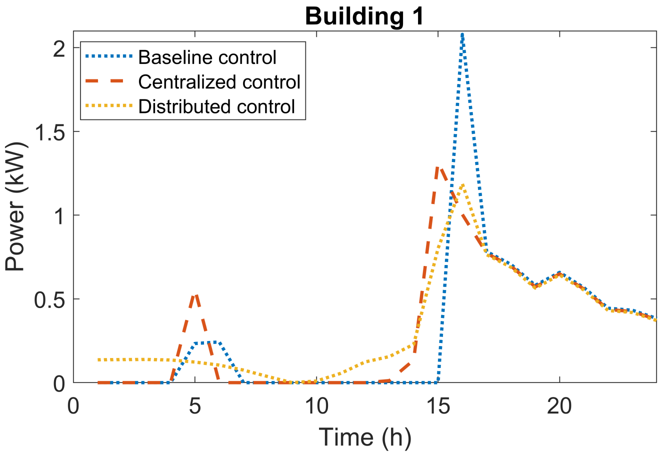

Figure 6.8: Power consumption of building #1

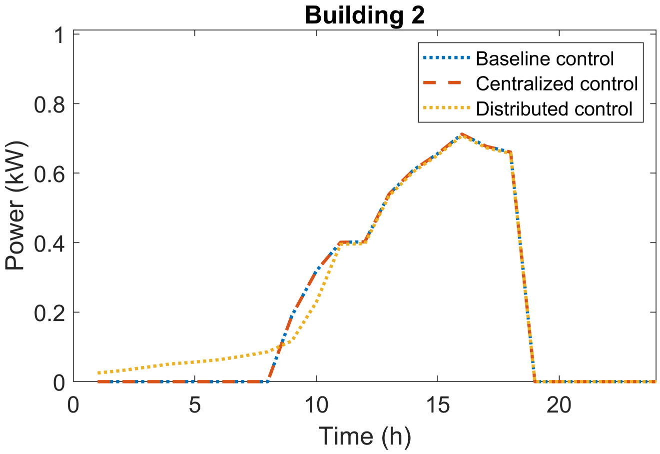

Figure 6.9: Power consumption of building #2

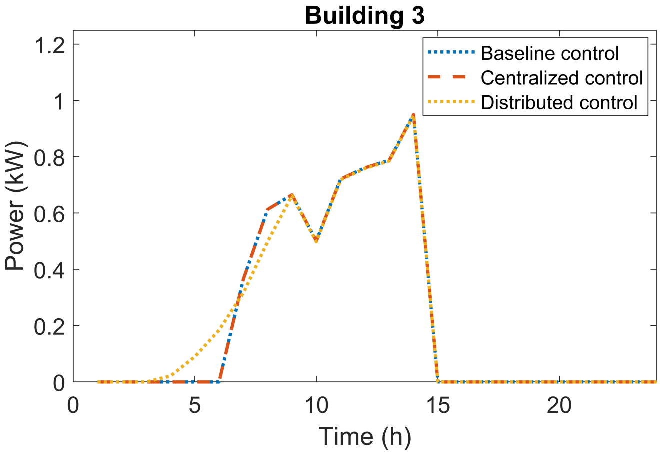

Figure 6.10: Power consumption of building #3

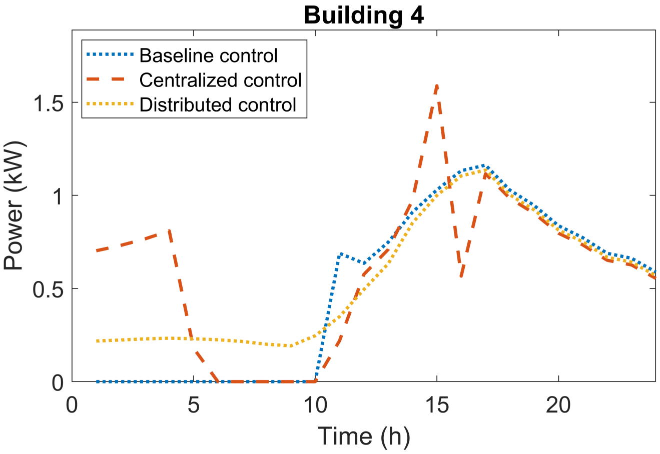

Figure 6.11: Power consumption of building #4

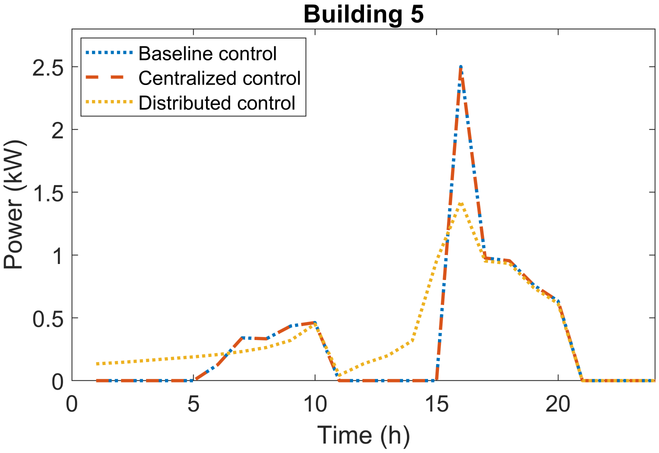

Figure 6.12: Power consumption of building #5

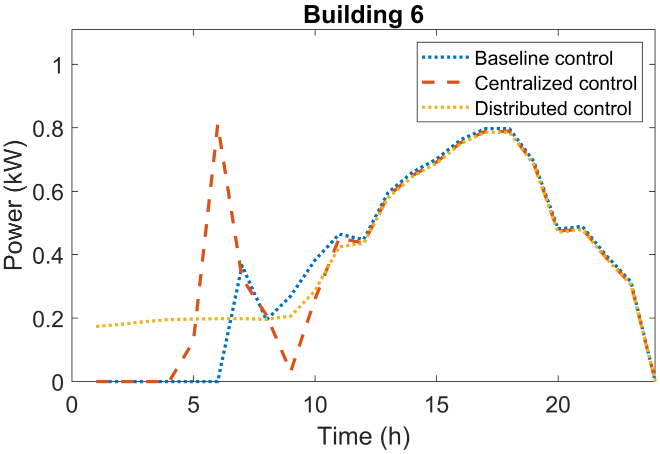

Figure 6.13: Power consumption of building #6

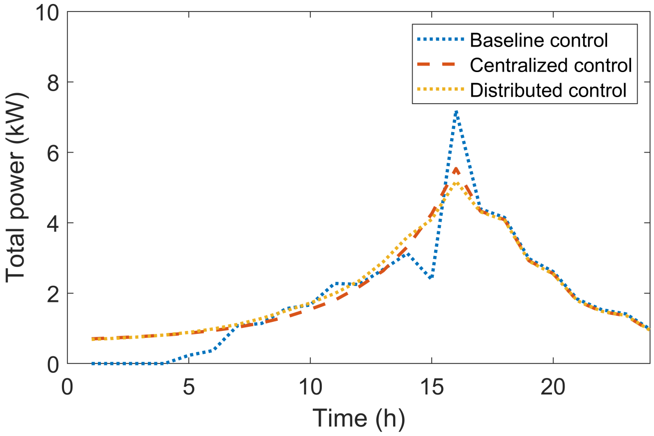

Figure 6.14: Total power consumption

	Total charge ($)		
	Baseline	Centralized	Distributed
Bld #1	1.66	1.45	1.42
Bld #2	1.10	1.09	1.10
Bld #3	0.68	0.64	0.72
Bld #4	2.21	2.17	2.18
Bld #5	1.94	1.68	1.66
Bld #6	1.60	1.57	1.58
Sum of individual	9.19	8.60	8.66

Table 6.1: The electricity costs for the various strategies in microgrid scenario

6.3 Chapter Summary

In this section, a non-cooperative game theoretic control framework for load scheduling of building clusters when the players are price makers is presented, i.e., the electricity price varies with instantaneous electrical demand. The existence and uniqueness of NE of the formulated game problem are proven and a distributed best response algorithm is presented to find the NE. The convergence of the algorithm is guaranteed by reformulating the original game as a potential game. A simulation test was carried out for six buildings and the proposed game theoretic control strategy was shown to be effective in reducing the aggregate electricity cost while ensuring lower PAR. The resultant control actions were very close to social optimum, with the Price of Anarchy of 1.007.

CHAPTER 7

SUMMARY AND FUTURE WORK

7.1 Summary

This dissertation presents two control approaches for building cluster energy management in support of grid reliability and efficiency: dictatorial load modulation control, which leverages the building flexible loads to stabilize distribution voltage against volatile solar PV generation, and market-based game theoretic control, which relies on a market mechanism to incentivize buildings' flexibility actions. To evaluate the potential for grid reliability support, voltage regulation control methods designed for two types of HVAC systems and game-theoretic control methods for two different pricing mechanisms were proposed and assessed either through simulation or experimental tests.

- *Distribution voltage support using variable-capacity HVAC systems:* a novel control method using variable-capacity HVAC systems to smooth PV power output has been proposed and tested. In this control method, the compressor speed is modulated by a variable frequency drive to drive the power to follow solar power output in order to reduce net demand/generation variations and voltage fluctuations. Laboratory tests showed that the compressor ramp rate limit had a direct impact on the power tracking performance. Better tracking performance was achieved with higher ramp rate limits. The voltage regulation controller could effectively reduce the variations of net demand/generation and nodal voltages. More than 55% reduction of voltage fluctuations was achieved for a test case with 50% PV penetration and 70% load ratio. With reduced voltage fluctuations, the SVR tap operations could be fully or partially eliminated. Relaxed SVR deadband settings would result in fewer tap operations, especially at moderate PV penetrations. Higher PV penetrations could lead to more frequent tap position changes.

- *Distribution voltage support through coordinative cycling of HVAC systems:* a voltage regulation control method that uses flexible thermal loads in cycling HVAC systems to mitigate adverse solar PV impact is discussed. Its effectiveness on distribution voltage regulation was examined using a community co-simulation platform. Simulation tests showed that the voltage regulation control of cycling HVAC systems is effective in reducing the number of SVR operations from 15 to 4, with a marginal increase in the average HVAC cycling frequency from 44 to 49 cycles per day per unit. For distribution systems without voltage regulation devices, a droop controller over thermostat setpoint could help maintain the feeder voltage within a prescribed range and reduce or even eliminate voltage excursions. However, the temperature setpoint adjustment may cause indoor discomfort.
- *Market-based game-theoretic control for peak demand reduction:* a non-cooperative game model is proposed to capture interactions of self-interested buildings with the electricity market and a control strategy has been devised through solution of the NE game problem. The existence and uniqueness of the NE for the game model have been proven under a mild condition, namely, the feasible action set does not admit a strategy with identical control schedules for all buildings. A centralized algorithm and a distributed algorithm are proposed for solving the aggregator game model and the centralized algorithm's convergence to the NE has been proved. Numerical tests with a commercial community showed that the control performance attained was close to social optimum with less than 2% performance degradation.
- *Maket-based game-theoretic control for flexible load dispatching:* a load dispatch problem is considered where the marginal electricity generation operation cost is as-

sumed to be demand-dependent. This study investigated a power model and an exponential model for the marginal cost curve, and proved the existence and uniqueness of NE for these two cost models. In order to verify the effectiveness of the proposed game-theoretic control for flexible load dispatching in building clusters, a simulation case study using a linear marginal cost model was considered. To find the NE, a distributed best response method was developed. The simulation tests showed that the game-theoretic control could reduce the overall operating cost by 5.8% and reduce peak load by 28% compared to a baseline operation strategy. The achieved performance was very close to the social optimum, with a Price of Anarchy of 1.007.

7.2 Future Work

Work presented in this dissertation can be extended in several directions:

- *Building flexible load estimation.* The discussed dictatorial load modulation control methods are heuristics-based. Optimization-based control methods can enable the building cluster to provide more effective support with limited flexible loads. However, in optimization-based control, the effectiveness of the control strategy is dependent on the quality of the building and HVAC system models. A reliable modeling methodology with adequate prediction accuracy and low computational complexity is needed for building flexible load estimation, which is a topic worth pursuing in future work.

- *Social cost splitting function.* In this study, the Shapley value is used to split the social cost among participants. The main advantage of the Shapley value approach is that it provides a fair allocation mechanism with favorable properties such as efficiency (the sum of individual contributions equals the value achieved by the alliance), symmetry (two members with the same Shapley value have the same share of cost/benefit), linearity (if the alliance S engages multiple projects, say two projects with value functions $V(S)$ and $U(S)$, then summing each member's shares across the two projects is the same as computing his/her share using the overall gain $V(S) + U(S)$), coalitional rationality (given how benefits/costs will be divided, all agents are willing to join the grand coalition and no agents prefer to form smaller coalitions). However, the disadvantage of the Shapley value approach is the high numerical complexity of the algorithm because the number of feature combinations grows exponentially. Therefore, a more numerically efficient cost allocation mechanism should be developed in future work.

- *Algorithm convergence properties.* The current study only considered a centralized algorithm and a distributed algorithm for a game with linear constraints. Nevertheless, in many building control problems, the models involved in the control strategy are nonlinear and non-convex, which may cause convergence issues with the proposed algorithms. Therefore, the NE solution algorithms should be improved to achieve convergence for a wide range of building control problems.

- *Indoor air comfort.* For indoor comfort impact assessment, the present study only considered the indoor air temperature effect. However, indoor comfort is influenced not only by temperature, but also by humidity ratio, air velocity and air quality. In future work, an improved comfort model may be incorporated in the building control problem.

Appendices

APPENDIX A

PUBLICATIONS

A.1 Conference

- Jiang, Zhimin, and Jie Cai. ”Distributed Game-Theoretic Control of Aggregate Building Thermal Loads Under Quadratic Generation Cost.” In 2022 American Control Conference (ACC), to appear
- Jie Cai, and Jiang, Zhimin. ”Primal-Dual Distributed Control of Residential Thermal Loads for Voltage Regulation of Distribution Systems with High PV Penetration.” In 2022 American Control Conference (ACC), to appear
- Jiang, Zhimin, and Jie Cai. ”Game Theoretic Control of Thermal Loads in Demand Response Aggregators.” In 2021 American Control Conference (ACC), to appear
- Jiang, Zhimin, Jie Cai, Philani Hlanze, and Hao Zhang. ”Optimized Control of Phase Change Material-Based Storage Integrated in Building Air-Distribution Systems.” In 2020 American Control Conference (ACC), to appear

A.2 Journal

- Jiang, Zhimin, Jie Cai. ”Optimal Predictive Control of Phase Change Material-Based Energy Storage in Buildings via Mixed-Integer Convex Programming.” Applied Thermal Engineering(2022): 118821.
- Jiang, Zhimin, Jie Cai, and Paul S. Moses. ”Smoothing control of solar photovoltaic

generation using building thermal loads." Applied Energy 277 (2020): 115523.

- Elhefny, Aly, Zhimin Jiang, and Jie Cai. ”Co-simulation and energy management of photovoltaic-rich residential communities for improved distribution voltage support with flexible loads." Solar Energy 231 (2022): 516-526.
- Hlanze, Philani, Aly Elhefny, Zhimin Jiang, Jie Cai, and Hamidreza Shabgard. ”Induct phase change material-based energy storage to enhance building demand flexibility." Applied Energy 310 (2022): 118520.
- Sanchez, Jerson, Zhimin Jiang, and Jie Cai.”Modeling and Mitigating Lifetime Impact of Building Demand Responsive Control of Heating, Ventilation and Air-Conditioning Systems." Journal of Building Performance Simulation, accepted
- Hlanze, Philani, Zhimin Jiang, Jie Cai, and Bo Shen. ”Model-Based Predictive Control of Multi-Stage Air-Source Heat Pumps Integrated with Phase Change Material-Embedded Ceilings." Applied Energy, under review.
- Cai, Jie, Zhimin Jiang. ”Privacy-Preserving Distributed Load Control to Mitigate Distribution Voltage Excursions Induced by Solar Photovoltaic." Solar Energy, under review.

A.3 Presentation

- "Distributed Game-Theoretic Control of Aggregate Building Thermal Loads Under Quadratic Generation Cost", American Control Conference (ACC), 2022
- ”Primal-Dual Distributed Control of Residential Thermal Loads for Voltage Regulation of Distribution Systems with High PV Penetration", American Control Conference (ACC), 2022

- ”Noncooperative Game based Demand Response for Multi-Building electricity consumption”, American Control Conference (ACC), 2021
- ”Optimal predictive control of PCM storage integrated in building air-distribution systems” American Control Conference (ACC), 2020.
- “Integration of Phase Change Material-Based Storage in Air Distribution Systems to Increase Building Power Flexibility”, The University of Tulsa, April 2019

REFERENCES

[1] U. DoE, “Quadrennial technology review 2015”, *US Department of Energy, Washington, DC*, 2015.

[2] M. Neukomm, V. Nubbe, and R. Fares, “Grid-interactive efficient buildings technical report series: Overview of research challenges and gaps”, 2019.

[3] *National conference of legislatures, state renewable portfolio and goals*, http://www.ncsl.org/research/energy/renewable-portfolio-standards.aspx, Accessed: 2019-12-15.

[4] C. E. Comission, *Energy commission adopts standards requiring solar systems for new homes, first in nation*, https://ww2.energy.ca.gov/releases/2018_releases/2018-05-09_building_standards_adopted_nr.html, Accessed: 2019-12-15.

[5] M. Karimi, H. Mokhlis, K. Naidu, S. Uddin, and A. Bakar, “Photovoltaic penetration issues and impacts in distribution network–a review”, *Renewable and Sustainable Energy Reviews*, vol. 53, pp. 594–605, 2016.

[6] P. Denholm, M. O’Connell, G. Brinkman, and J. Jorgenson, “Overgeneration from solar energy in california. a field guide to the duck chart”, National Renewable Energy Lab.(NREL), Golden, CO (United States), Tech. Rep., 2015.

[7] B. Palmintier *et al.*, “On the path to sunshot. emerging issues and challenges in integrating solar with the distribution system”, National Renewable Energy Lab.(NREL), Golden, CO (United States), Tech. Rep., 2016.

[8] S. Shivashankar, S. Mekhilef, H. Mokhlis, and M. Karimi, “Mitigating methods of power fluctuation of photovoltaic (PV) sources–a review”, *Renewable and Sustainable Energy Reviews*, vol. 59, pp. 1170–1184, 2016.

[9] N. Ina, S. Yanagawa, T. Kato, and Y. Suzuoki, “Smoothing of PV system output by tuning mppt control”, *Electrical Engineering in Japan*, vol. 152, no. 2, pp. 10–17, 2005.

[10] Y. S. Lim and J. H. Tang, “Experimental study on flicker emissions by photovoltaic systems on highly cloudy region: A case study in malaysia”, *Renewable Energy*, vol. 64, pp. 61–70, 2014.

[11] M. Datta, T. Senjyu, A. Yona, T. Funabashi, and C.-H. Kim, “A coordinated control method for leveling PV output power fluctuations of PV–diesel hybrid systems connected to isolated power utility”, *IEEE Transactions on Energy Conversion*, vol. 24, no. 1, pp. 153–162, 2009.

[12] R. van Haaren, M. Morjaria, and V. Fthenakis, “An energy storage algorithm for ramp rate control of utility scale PV (photovoltaics) plants”, *Energy*, vol. 91, pp. 894–902, 2015.

[13] A. Arabkoohsar, L. Machado, M. Farzaneh-Gord, and R. Koury, “The first and second law analysis of a grid connected photovoltaic plant equipped with a compressed air energy storage unit”, *Energy*, vol. 87, pp. 520–539, 2015.

[14] N. Kakimoto, H. Satoh, S. Takayama, and K. Nakamura, “Ramp-rate control of photovoltaic generator with electric double-layer capacitor”, *IEEE Transactions on Energy Conversion*, vol. 24, no. 2, pp. 465–473, 2009.

[15] T. Kanehira, A. Takahashi, J. Imai, and S. Funabiki, “A comparison of electric power smoothing control methods for the distributed generation system”, *IEEJ Transactions on Power and Energy*, vol. 134, no. 7, pp. 596–603, 2014.

[16] A. Ellis, D. Schoenwald, J. Hawkins, S. Willard, and B. Arellano, “PV output smoothing with energy storage”, in *2012 38th IEEE Photovoltaic Specialists Conference*, IEEE, 2012, pp. 001 523–001 528.

[17] X. Li, D. Hui, and X. Lai, “Battery energy storage station (bess)-based smoothing control of photovoltaic (PV) and wind power generation fluctuations”, *IEEE transactions on sustainable energy*, vol. 4, no. 2, pp. 464–473, 2013.

[18] J. MacDonald, S. Kiliccote, J. Boch, J. Chen, and R. Nawy, “Commercial building loads providing ancillary services in pjm”, Lawrence Berkeley National Lab.(LBNL), Berkeley, CA (United States), Tech. Rep., 2014.

[19] Y. Lin, P. Barooah, S. Meyn, and T. Middelkoop, “Experimental evaluation of frequency regulation from commercial building HVAC systems”, *IEEE Transactions on Smart Grid*, vol. 6, no. 2, pp. 776–783, 2015.

[20] L. Fabietti, T. T. Gorecki, F. A. Qureshi, A. Bitlislioğlu, I. Lymperopoulos, and C. N. Jones, “Experimental implementation of frequency regulation services using commercial buildings”, *IEEE Transactions on Smart Grid*, vol. 9, no. 3, pp. 1657–1666, 2016.

[21] H. Wang, S. Wang, and R. Tang, “Investigation on the use of pumps in HVAC systems for providing ancillary services in smart grids”, *Energy Procedia*, vol. 159, pp. 219–224, 2019.

[22] Y.-J. Kim, E. Fuentes, and L. K. Norford, “Experimental study of grid frequency regulation ancillary service of a variable speed heat pump”, *IEEE Transactions on Power Systems*, vol. 31, no. 4, pp. 3090–3099, 2015.

[23] M. Motalleb, M. Thornton, E. Reihani, and R. Ghorbani, “Providing frequency regulation reserve services using demand response scheduling”, *Energy Conversion and Management*, vol. 124, pp. 439–452, 2016.

[24] L. Su and L. K. Norford, “Demonstration of HVAC chiller control for power grid frequency regulation—part 1: Controller development and experimental results”, *Science and Technology for the Built Environment*, vol. 21, no. 8, pp. 1134–1142, 2015.

[25] J. Cai and J. E. Braun, “Laboratory-based assessment of HVAC equipment for power grid frequency regulation: Methods, regulation performance, economics, indoor comfort and energy efficiency”, *Energy and Buildings*, vol. 185, pp. 148–161, 2019.

[26] S. Rotger-Griful, S. Chatzivasileiadis, R. H. Jacobsen, E. M. Stewart, J. M. Domingo, and M. Wetter, “Hardware-in-the-loop co-simulation of distribution grid for demand response”, in *2016 Power Systems Computation Conference (PSCC)*, IEEE, 2016, pp. 1–7.

[27] S. Williams, M. Short, and T. Crosbie, “On the use of thermal inertia in building stock to leverage decentralised demand side frequency regulation services”, *Applied Thermal Engineering*, vol. 133, pp. 97–106, 2018.

[28] D. S. Callaway, “Tapping the energy storage potential in electric loads to deliver load following and regulation, with application to wind energy”, *Energy Conversion and Management*, vol. 50, no. 5, pp. 1389–1400, 2009.

[29] Q. Shi, F. Li, Q. Hu, and Z. Wang, “Dynamic demand control for system frequency regulation: Concept review, algorithm comparison, and future vision”, *Electric Power Systems Research*, vol. 154, pp. 75–87, 2018.

[30] J. Cai and J. E. Braun, “Laboratory-based assessment of HVAC equipment for power grid frequency regulation: Methods, regulation performance, economics, indoor comfort and energy efficiency”, *Energy and Buildings*, vol. 185, pp. 148–161, 2019.

[31] E. Vrettos, E. C. Kara, J. MacDonald, G. Andersson, and D. S. Callaway, “Experimental demonstration of frequency regulation by commercial buildings—part i: Modeling and hierarchical control design”, *IEEE Transactions on Smart Grid*, vol. 9, no. 4, pp. 3213–3223, 2016.

[32] E. Vrettos, E. C. Kara, J. MacDonald, G. Andersson, and D. S. Callaway, “Experimental demonstration of frequency regulation by commercial buildings—part ii: Results and performance evaluation”, *IEEE Transactions on Smart Grid*, vol. 9, no. 4, pp. 3224–3234, 2016.

[33] M. Maasoumy, C. Rosenberg, A. Sangiovanni-Vincentelli, and D. S. Callaway, “Model predictive control approach to online computation of demand-side flexibility of com-

mercial buildings HVAC systems for supply following", in *2014 American Control Conference*, IEEE, 2014, pp. 1082–1089.

[34] R. Tonkoski and L. A. Lopes, "Impact of active power curtailment on overvoltage prevention and energy production of PV inverters connected to low voltage residential feeders", *Renewable energy*, vol. 36, no. 12, pp. 3566–3574, 2011.

[35] A. M. Howlader, S. Sadoyama, L. R. Roose, and S. Sepasi, "Distributed voltage regulation using volt-var controls of a smart PV inverter in a smart grid: An experimental study", *Renewable Energy*, vol. 127, pp. 145–157, 2018.

[36] M. Hasheminamin, V. G. Agelidis, A. Ahmadi, P. Siano, and R. Teodorescu, "Single-point reactive power control method on voltage rise mitigation in residential networks with high PV penetration", *Renewable Energy*, vol. 119, pp. 504–512, 2018.

[37] M. Zeraati, M. E. H. Golshan, and J. M. Guerrero, "Distributed control of battery energy storage systems for voltage regulation in distribution networks with high PV penetration", *IEEE Transactions on Smart Grid*, vol. 9, no. 4, pp. 3582–3593, 2016.

[38] A. Zakariazadeh, O. Homaee, S. Jadid, and P. Siano, "A new approach for real time voltage control using demand response in an automated distribution system", *Applied Energy*, vol. 117, pp. 157–166, 2014.

[39] X. Liu, A. Aichhorn, L. Liu, and H. Li, "Coordinated control of distributed energy storage system with tap changer transformers for voltage rise mitigation under high photovoltaic penetration", *IEEE Transactions on Smart Grid*, vol. 3, no. 2, pp. 897–906, 2012.

[40] W. Pereira, A. Bögl, and T. Natschläger, "Sensitivity analysis and validation of an energyplus model of a house in upper austria", *Energy Procedia*, vol. 62, pp. 472–481, 2014.

[41] J. Zhao, K. P. Lam, B. E. Ydstie, and V. Loftness, "Occupant-oriented mixed-mode energyplus predictive control simulation", *Energy and Buildings*, vol. 117, pp. 362–371, 2016.

[42] T. E. Morakinyo, K. K. C. Dahanayake, E. Ng, and C. L. Chow, "Temperature and cooling demand reduction by green-roof types in different climates and urban densities: A co-simulation parametric study", *Energy and Buildings*, vol. 145, pp. 226–237, 2017.

[43] B. Pandey, R. Banerjee, and A. Sharma, "Coupled energyplus and CFD analysis of pcm for thermal management of buildings", *Energy and buildings*, vol. 231, p. 110 598, 2021.

[44] D. P. Chassin, K. Schneider, and C. Gerkensmeyer, “Gridlab-d: An open-source power systems modeling and simulation environment”, in *2008 IEEE/PES Transmission and Distribution Conference and Exposition*, IEEE, 2008, pp. 1–5.

[45] C. Li, X. Yu, W. Yu, G. Chen, and J. Wang, “Efficient computation for sparse load shifting in demand side management”, *IEEE Transactions on Smart Grid*, vol. 8, no. 1, pp. 250–261, 2016.

[46] Z. Wang, R. Yang, and L. Wang, “Multi-agent control system with intelligent optimization for smart and energy-efficient buildings”, pp. 1144–1149, 2010.

[47] L. Klein *et al.*, “Coordinating occupant behavior for building energy and comfort management using multi-agent systems”, *Automation in construction*, vol. 22, pp. 525–536, 2012.

[48] S. Bahrami and M. Parniani, “Game theoretic based charging strategy for plug-in hybrid electric vehicles”, *IEEE Transactions on Smart Grid*, vol. 5, no. 5, pp. 2368–2375, 2014.

[49] J. Li, C. Li, Y. Xu, Z. Y. Dong, K. P. Wong, and T. Huang, “Noncooperative game-based distributed charging control for plug-in electric vehicles in distribution networks”, *IEEE Transactions on Industrial Informatics*, vol. 14, no. 1, pp. 301–310, 2016.

[50] S. Li, W. Zhang, J. Lian, and K. Kalsi, “Market-based coordination of thermostatically controlled loads—part i: A mechanism design formulation”, *IEEE Transactions on Power Systems*, vol. 31, no. 2, pp. 1170–1178, 2015.

[51] I. Atzeni, L. G. Ordóñez, G. Scutari, D. P. Palomar, and J. R. Fonollosa, “Noncooperative day-ahead bidding strategies for demand-side expected cost minimization with real-time adjustments: A gnep approach”, *IEEE transactions on Signal Processing*, vol. 62, no. 9, pp. 2397–2412, 2014.

[52] A.-H. Mohsenian-Rad, V. W. Wong, J. Jatskevich, R. Schober, and A. Leon-Garcia, “Autonomous demand-side management based on game-theoretic energy consumption scheduling for the future smart grid”, *IEEE transactions on Smart Grid*, vol. 1, no. 3, pp. 320–331, 2010.

[53] S. Maharjan, Q. Zhu, Y. Zhang, S. Gjessing, and T. Basar, “Dependable demand response management in the smart grid: A stackelberg game approach”, *IEEE Transactions on Smart Grid*, vol. 4, no. 1, pp. 120–132, 2013.

[54] T. Basar and R. Srikant, “Revenue-maximizing pricing and capacity expansion in a many-users regime”, in *Proceedings. Twenty-First Annual Joint Conference of the IEEE Computer and Communications Societies*, IEEE, vol. 1, 2002, pp. 294–301.

[55] K. Alshehri, J. Liu, X. Chen, and T. Başar, “A game-theoretic framework for multiperiod-multicompany demand response management in the smart grid”, *IEEE Transactions on Control Systems Technology*, 2020.

[56] H. M. Soliman and A. Leon-Garcia, “Game-theoretic demand-side management with storage devices for the future smart grid”, *IEEE Transactions on Smart Grid*, vol. 5, no. 3, pp. 1475–1485, 2014.

[57] P. Samadi, H. Mohsenian-Rad, R. Schober, and V. W. Wong, “Advanced demand side management for the future smart grid using mechanism design”, *IEEE Transactions on Smart Grid*, vol. 3, no. 3, pp. 1170–1180, 2012.

[58] E. Fernandez, M. Hossain, and M. Nizami, “Game-theoretic approach to demand-side energy management for a smart neighbourhood in sydney incorporating renewable resources”, *Applied energy*, vol. 232, pp. 245–257, 2018.

[59] A. Barbato, A. Capone, L. Chen, F. Martignon, and S. Paris, “A distributed demand-side management framework for the smart grid”, *Computer Communications*, vol. 57, pp. 13–24, 2015.

[60] D. Monderer and L. S. Shapley, “Potential games”, *Games and economic behavior*, vol. 14, no. 1, pp. 124–143, 1996.

[61] D. M. Topkis, *Supermodularity and complementarity*. Princeton university press, 1998.

[62] G. M. Korpelevich, “The extragradient method for finding saddle points and other problems”, *Matecon*, vol. 12, pp. 747–756, 1976.

[63] M. A. Akivis and V. V. Konnov, “Some local aspects of the theory of conformal structure”, *Russian Mathematical Surveys*, vol. 48, no. 1, p. 1, 1993.

[64] C. Groetsch, “The theory of tikhonov regularization for fredholm equations”, *104p, Boston Pitman Publication*, 1984.

[65] B. Martinet, “Régularisation d’inéquations variationnelles par approximations successives. rev. française informat”, *Recherche Opérationnelle*, vol. 4, pp. 154–158, 1970.

[66] J. Eckstein, “Splitting methods for monotone operators with applications to parallel optimization”, Ph.D. dissertation, Massachusetts Institute of Technology, 1989.

[67] H. Nikaidô and K. Isoda, “Note on non-cooperative convex games”, *Pacific Journal of Mathematics*, vol. 5, no. S1, pp. 807–815, 1955.

[68] A. von Heusinger and C. Kanzow, “Optimization reformulations of the generalized nash equilibrium problem using nikaido-isoda-type functions”, *Computational Optimization and Applications*, vol. 43, no. 3, pp. 353–377, 2009.

[69] T. De Luca, F. Facchinei, and C. Kanzow, “A semismooth equation approach to the solution of nonlinear complementarity problems”, *Mathematical programming*, vol. 75, no. 3, pp. 407–439, 1996.

[70] C. Dutang, “A survey of gne computation methods: Theory and algorithms”, 2013.

[71] S. J. Treado, “An agent-based methodology for optimizing building HVAC system performance”, *ASHRAE Transactions*, vol. 116, no. 2, pp. 124–135, 2010.

[72] P. Zhao, S. Suryanarayanan, and M. G. Simoes, “An energy management system for building structures using a multi-agent decision-making control methodology”, *IEEE transactions on industry applications*, vol. 49, no. 1, pp. 322–330, 2012.

[73] B. Sun, P. B. Luh, Q.-S. Jia, Z. Jiang, F. Wang, and C. Song, “An integrated control of shading blinds, natural ventilation, and HVAC systems for energy saving and human comfort”, in *2010 IEEE International Conference on Automation Science and Engineering*, IEEE, 2010, pp. 7–14.

[74] B. He, X. Yuan, and W. Zhang, “A customized proximal point algorithm for convex minimization with linear constraints”, *Computational Optimization and Applications*, vol. 56, no. 3, pp. 559–572, 2013.

[75] A. Hoke, R. Butler, J. Hambrick, and B. Kroposki, “Maximum photovoltaic penetration levels on typical distribution feeders”, National Renewable Energy Lab.(NREL), Golden, CO (United States), Tech. Rep., 2012.

[76] G. Ari and Y. Baghzouz, “Impact of high PV penetration on voltage regulation in electrical distribution systems”, in *2011 International Conference on Clean Electrical Power (ICCEP)*, IEEE, 2011, pp. 744–748.

[77] M. Baran and F. F. Wu, “Optimal sizing of capacitors placed on a radial distribution system”, *IEEE Transactions on power Delivery*, vol. 4, no. 1, pp. 735–743, 1989.

[78] G. Shahgholian and S. Soltani, “Modeling and application of step voltage regulators in radial-meshed networks”, *International Journal of Information and Electronics Engineering*, vol. 3, no. 4, 2013.

[79] N. E. M. Association *et al.*, “American national standards institute (ANSI) c84. 1-2011, voltage ratings for electric power systems and equipment”, *Rosslyn, VA*, 2011.

[80] J. Dong *et al.*, “Operational impacts of high penetration solar power on a real-world distribution feeder”, in *2018 IEEE Power & Energy Society Innovative Smart Grid Technologies Conference (ISGT)*, IEEE, 2018, pp. 1–5.

[81] Y. Xue *et al.*, “Voltage impact analyses of solar photovoltaics on distribution load tap changer operations”, in *2017 North American Power Symposium (NAPS)*, IEEE, 2017, pp. 1–6.

[82] P. Torcelini *et al.*, “Doe commercial building benchmark models”, National Renewable Energy Lab.(NREL), Golden, CO (United States), Tech. Rep., 2008.

[83] D. B. Shirey III, H. I. Henderson Jr, and R. A. Raustad, “Understanding the dehumidification performance of air-conditioning equipment at part-load conditions”, Univ. of Central Florida, Orlando, FL (United States), Tech. Rep., 2006.

[84] R. D. Zimmerman, C. E. Murillo-Sánchez, and R. J. Thomas, “Matpower: Steady-state operations, planning, and analysis tools for power systems research and education”, *IEEE Transactions on power systems*, vol. 26, no. 1, pp. 12–19, 2010.

[85] M. E. Baran and F. F. Wu, “Network reconfiguration in distribution systems for loss reduction and load balancing”, *IEEE Power Engineering Review*, vol. 9, no. 4, pp. 101–102, 1989.

[86] H. I. Henderson and K. Rengarajan, “A model to predict the latent capacity of air conditioners and heat pumps at part-load conditions with constant fan operation”, American Society of Heating, Refrigerating and Air-Conditioning Engineers …, Tech. Rep., 1996.

[87] A. L. Hjortland and J. E. Braun, “Load-based testing methodology for fixed-speed and variable-speed unitary air conditioning equipment”, *Science and Technology for the Built Environment*, vol. 25, no. 2, pp. 233–244, 2019.

[88] U. B. Code. “International code council”. (2006-2018).

[89] E. McKenna, M. Krawczynski, and M. Thomson, “Four-state domestic building occupancy model for energy demand simulations”, *Energy and Buildings*, vol. 96, pp. 30–39, 2015.

[90] S. Wilcox and A. Andreas, “Solar resource & meteorological assessment project (SOLRMAP): Observed atmospheric and solar information system (OASIS); tucson, arizona (Data)”, National Renewable Energy Lab.(NREL), Golden, CO (United States), Tech. Rep., 2010.

[91] M. Olama, J. Dong, I. Sharma, Y. Xue, and T. Kuruganti, "Frequency analysis of solar PV power to enable optimal building load control", *Energies*, vol. 13, no. 18, p. 4593, 2020.

[92] D. Evans, "Simplified method for predicting photovoltaic array output", *Solar energy*, vol. 27, no. 6, pp. 555–560, 1981.

[93] G. Notton, C. Cristofari, M. Mattei, and P. Poggi, "Modelling of a double-glass photovoltaic module using finite differences", *Applied thermal engineering*, vol. 25, no. 17-18, pp. 2854–2877, 2005.

[94] Q. Kou, S. Klein, and W. Beckman, "A method for estimating the long-term performance of direct-coupled PV pumping systems", *Solar Energy*, vol. 64, no. 1-3, pp. 33–40, 1998.

[95] J. Stultz and L. Wen, "Thermal performance testing and analysis of photovoltaic modules in natural sunlight", *LSA Task Report*, vol. 5101, p. 31, 1977.

[96] A. Standard, *C84. 1-2011, electric power systems and equipment-voltage ratings (60 hertz).*

[97] S. Boyd, S. P. Boyd, and L. Vandenberghe, *Convex optimization*. Cambridge university press, 2004.

[98] F. Facchinei and J.-S. Pang, *Finite-dimensional variational inequalities and complementarity problems*. Springer Science & Business Media, 2007.

[99] J. F. Nash *et al.*, "Equilibrium points in n-person games", *Proceedings of the national academy of sciences*, vol. 36, no. 1, pp. 48–49, 1950.

[100] M. Phillips and J. R. Marden, "Design tradeoffs in concave cost-sharing games", *IEEE Transactions on Automatic Control*, vol. 63, no. 7, pp. 2242–2247, 2017.

[101] J. Cai and J. Braun, "An inverse hygrothermal model for multi-zone buildings", *Journal of Building Performance Simulation*, vol. 9, no. 5, pp. 510–528, 2016.

[102] Z. Jiang and J. Cai, "Game theoretic control of thermal loads in demand response aggregators", in *2021 American Control Conference (ACC)*, IEEE, 2021, pp. 4141–4147.

[103] J. Cai, H. Zhang, D. Kim, J. E. Braun, and J. Hu, "Convex optimization-based control of sustainable communities with on-site photovoltaic (PV) and batteries", in *2017 IEEE Conference on Control Technology and Applications (CCTA)*, IEEE, 2017, pp. 1007–1012.

[104] K. R. Apt, “Strategic games”, *Course Notes*, pp. 21–22, 2011.